Wide band modelling of an air-core power transformer winding

B.J van Jaarsveld

Thesis presented in partial fulfilment of the requirements for the degree Master of Science in Engineering in the Faculty of Engineering at Stellenbosch University

Supervisor: Prof H.J Vermeulen
Department of Electrical & Electronic Engineering

December 2013

DECLARATION

By submitting this thesis electronically, I declare that the entirety of the work contained therein is my own, original work, that I am the sole author thereof (save to the extent explicitly otherwise stated), that reproduction and publication thereof by Stellenbosch University will not infringe any third party rights and that I have not previously in its entirety or in part submitted it for obtaining any qualification.

B. J. van Jaarsveld December 2013

ABSTRACT

The objective of this project is to develop an electromagnetic model that can be used to accurately calculate the voltage distribution in a transformer winding structure when excited with standard impulse excitation waves. This voltage distribution is required during the design stage of a power transformer to ensure that the insulation is capable of withstanding the occurring electric field stresses during these tests. This study focuses on the modelling of a single disk-type power transformer winding without the presence of an iron-core. Methods of calculating self- and mutual-inductances of transformer windings are presented and validated by means of finite element method software simulations. The same is done for the calculation methods used for calculating the capacitances in and around the winding structure. The calculated and FEM-simulated results are compared to measured values as a final stage of validation. The methods used to calculate the various model parameters seem to produce results that agrees well with measured values. The non-linear frequency dependant dissipative nature of transformer windings is also investigated and a methodology to take this into account is proposed and implemented. The complete modelling methodology proposed in this thesis, which includes the calculation of the model parameters, model synthesis and solver algorithm, are applied to an actual case study. The case study is performed on an air-core reactor manufactured using a disk-type power transformer winding. The reactor is excited with standard lightning impulse waves and the voltages along the winding are measured. The calculated and measured voltage wave forms are compared in both the frequency and time-domain. From the comparison it is found that the model accurately represents the actual transient voltage response of the test-unit for the frequency range of interest during standard factory acceptance tests.

OPSOMMING

Die doel van hierdie projek is om 'n elektromagnetiese model te ontwikkel wat gebruik kan word om die spanningsverspreiding in 'n transformatorwindingstruktuur te bereken as standaard weerligimpulstoetse toegedien word. Hierdie spanningsverspreiding word vereis tydens die ontwerpstadium van ‘n kragtransformator om te verseker dat die isolasie in staat is om die elektriese veldsterkte tydens hierdie toetse te weerstaan. Hierdie studie fokus op die modelering van 'n enkele skyftipe-kragtransformatorwinding sonder die teenwoordigheid van 'n ysterkern. Metodes van berekening van self- n wedersydse-induktansie van transformatorwindings word aangebied en getoets deur middel van Eindige-Element-Metode (EEM) simulasies. Dieselfde word gedoen vir die metodes wat gebruik word vir die berekening van die kapasitansies in en rondom die windingstruktuur. Die berekende en EEM-gesimuleerde resultate word vergelyk met die gemeete waardes as 'n finale vlak van bekragtiging. Die metodes wat gebruik word om die verskillende modelparameters te bereken vergelyk goed met gemete waardes. Die nie-lineêre frekwensie-afhanklike verliese van transformatorwindings word ook ondersoek en 'n metode om hierdie in ag te neem is voorgestel en geïmplementeer. Die volledige voorgestelde modeleringsmetodiek in hierdie tesis, wat die berekening van die modelparameters, modelsintese en oplosingsalgoritme insluit word toegepas op 'n werklike gevallestudie. Die gevallestudie is uitgevoer op 'n lugkern-reaktor wat 'n skyftipe-kragtransformatorwinding. Die reaktor word onderwerp aan die standaard weerligimpuls golwe en die spanning al langs die winding word gemeet. Die berekende en gemete spanning golf vorms word met mekaar vergelyk in beide die frekwensie- en tyd-vlak. Uit die vergelyking blyk dit dat die model die werklike oorgangspanningsweergawe van die toetseenheid akkuraat verteenwoordig vir die frekwensie reeks van belang tydens standaard fabriekaanvaardingstoetse.

ACKNOWLEGEMENTS

During research I have done in this project, I have had the privilege in being guided and mentored by renowned experts in this field of study. Without their help and the grace of my God this work would not have been possible. My sincerest gratitude goes to Robert Degeneff - president of Utility Systems Technologies (UST) - for sharing his knowledge gained by years of experience and his constant words of encouragement. I will treasure our casual discussions at the dinners in Albany. You have been a great mentor and friend – may God bless you and your family. I thank my supervisor at Powertech Transformers Pty. (Ltd) Nico Günter and the rest of the Technology team for creating a resourceful, productive and friendly environment at the office where I could focus on my research. Many thanks to Angélica Rocha and the other members of the Cigré joint workgroup A2/C4.39 for creating a platform for sharing knowledge and experience. I have learned a considerable amount from my interaction with this group of experts and hope that my contribution to the Cigré organisation and similiar entities will grow in value over time. A special thanks to my supervisor at the University of Stellenbosch, Johan Vermeulen. Your passion for the science of engineering and your philosopical discussions ensured that my time spent with you was insightful and enjoyable. I want to extend my gratitude to Baudilio Valecillos from TrafoExperts for his assistance and guidance in my research. Thank you for your positive attitude during the long hours we spent in the laboratory. To my wive Elsje, you have been a great friend and spouse to me. I love you dearly. Thank you for your patience and support with my research. To my mother Renette, thank you for your help in proofreading my work. Your support means a lot to me and I treasure your love with all my heart. Without the grace of my God and Saviour all my work in life would be of no value. I thank you Lord for your love and guidance through your Spirit, and your constant encouragement.

In him was life;
and the life was the light of men.
And the light shineth in darkness;
and the darkness comprehended it not.

- *John1:5*
King James Bible,
Cambridge Edition

TABLE OF CONTENTS

LIST OF TABLES

LIST OF FIGURES

SYMBOLS AND ABREVIATIONS

ADC	Analogue to digital conversion
A	Cross-sectional area
$\bar{A}$	Magnetic vector potential
a	Enclosed surface area
α	Gradient factor of initial voltage distribution in winding
α_e	Frequency dependant damping factor
α_k, β_k, k_k	Double-exponential equation constants
α_{pu}, β_{pu}	Per unit length of materials in a per unit volume of composite insulation
BIL	Basic insulation level
$\bar{B}$	Magnetic field density vector
C	Capacitance
$[\boldsymbol{C}]$	Branch capacitance matrix
$[\boldsymbol{C}_n]$	Nodal capacitance matrix
C_c	Capacitance of probe lead to ground
C_g, C_{w-g}	Capacitance of winding to ground
C_p	Capacitance between windings
C_s	Series capacitance of winding
C_{tg}	Capacitance of electrical turn to ground
C_{tt}	Capacitance between two turns
DEM	Difference equation method
∇	Vector partial-differentiation operator
d	Distance between electrode surfaces
σ	Conductivity of material
δ	Loss angle
ε_0	Permittivity of vacuum
ε_{equ}	Equivalent permittivity of composite insulation structure
ε_r	Relative permittivity of material
FEM	Finite Element Method
F_{lost}	Fraction of electrical turns lost due to staggered cross-overs
f	Frequency in Hertz

f_n	Nyquist frequency
f_s	Sampling frequency
GMD	Geometrical mean distance
G	Conductance
$[\boldsymbol{G}]$	Branch conductance matrix
$[\boldsymbol{G}_n]$	Nodal conductance matrix
H_e	Conductor height
$\bar{H}$	Magnetic field vector
h	Overlapping height of facing surfaces of adjacent conductors
I	Current magnitude scalar value
$\bar{I}$	Current vector
I_r	Resistive current through dielectric material
I_s	Displacement current through dielectric material
$\boldsymbol{I}(t)$	Injected nodal current column-vector
$\boldsymbol{I}_R$	Current column-vector of MTLM at receiving node
$\boldsymbol{I}_S$	Current column-vector of MTLM at sending node
$[\mathfrak{T}]$	The identity matrix
$i(t)$	Instantaneous current
$\boldsymbol{i}(t)$	Instantaneous current column-vector
$\bar{\imath}$	Current vector
K,E	Complete elliptic integral of first and second kind
KVL	Kirchhoff's voltage law
KCL	Kirchhoff's current law
k	Modules of the Elliptic integral of first and second kind
k_k	constant
k_{lost}	Fraction of electrical turn lost due to cross-over staggering
LI	Lightning impulse wave
LIC	Lightning impulse wave with a chopped tail
LPM	Lumped parameter model
L	Inductance
L_g	Ground loop inductance
L_{Total}	Total winding inductance
$[\boldsymbol{L}]$	Branch inductance matrix

$[\boldsymbol{L}_n]$	Nodal inductance matrix
$[\boldsymbol{\Gamma}_n]$	Inverse nodal inductance matrix
l	Length
λ	Wave length
MTLM	Multi transmission line model
MSE	Mean square error of digitised signal
μ_0	Permeability of free space
μ_r	Relative permeability of material
N	Number of electrical turns
N_{lost}	Number of electrical turns lost due to cross-over staggering
N_{mech}	Number of mechanical turns in winding
N_{pitch}	Number of pitches required to complete a crossover
N_{sp}	Number of spacers around the circumference of the winding
ODE	Ordinary differential equation
$[\boldsymbol{0}]$	The zero matrix
ω	Radial frequency
ω_o	Fundamental frequency
ρ	Resistivity of material
RLC	Collective of resistance, inductance and capacitance
R	Resistance
R_m	Radius to centre of current filament
R_{mw}	Mean radius of winding
R_p	Shunt resistance of measuring probe
R_t	Source output resistance
$[\boldsymbol{R}_n]$	Nodal resistance matrix
r_{av}	Average radius between facing surfaces of two adjacent conductors
s	Relative displacement
ς	Skin depth
T	Sample interval of discrete signal
$[\boldsymbol{T}]$	Adjacency matrix
t	Time instant
Δt	Time step size
t_{30}	Time duration for LI wave to reach 30% of peak value

t_{50}	Time duration for LI wave to drop to 50% of peak value
t_{90}	Time duration for LI wave to reach 90% of peak value
t_c	Time duration until chopping of LI wave tail
t_f	Rise-time of wave front of LI
t_{pap}	Paper thickness
V_{peak}	Peak voltage amplitude
V	Voltage magnitude scalar value
$\boldsymbol{V}_R$	Voltage column-vector at receiving end of MTLM
$\boldsymbol{V}_S$	Voltage column-vector at sending end of MTLM
v	Velocity of wave propagation
$v(t)$	Instantaneous voltage
$\boldsymbol{v}(t)$	Instantaneous voltage column-vector
$v(nT)$	Discrete time-domain voltage
$v(t,x)$	Instantaneous voltage as a function of position
φ	Noise variance
W	Energy
W_e	Conductor width
W_{sp}	Spacer width
$w(nT,\omega)$	Discrete-time windowing frequency dependant function
x	Position
$[\boldsymbol{Y_n}]$	Nodal admittance matrix
z	Axial distance between current filament centres

Chapter 1 Project description and motivation

1.1 Introduction

In our current society the use of electricity has become an integral component of the socioeconomic infrastructure [1]. Industries involved in manufacturing, mining and agriculture play a major role in the economy of a country. These industries are highly dependent on a stable electrical infrastructure. Health services, public transportation infrastructures and other basic service deliveries also require a reliable supply of energy.

The power grids in developing countries such as South-Africa, operate under extremely challenging conditions. Insufficient power generation, limited transmission line capacity, a lack of maintenance and a shortage of local content cripple the socioeconomic growth of these countries. The prospective development and upkeep of these electrical infrastructures are faced with various challenges relating to the available financial resources [2] [3].

The reliable supply of energy is not only a challenge faced by developing countries. Power utilities of countries with strong economies such as China are required to meet the ever increasing demand of electricity [4].

The reliability of the system components used in a power grid plays a crucial role in light of the scenarios portrayed above. One of these components is the large power transformer. Large power transformers are required throughout a power grid and are one of many system components required for the effective transmission of energy over large geographical areas. Failure of these transformers causes loss of revenue for both the power utility and its client. The client suffers downtime in production while the utility has considerable capital expenditure to repair or replace these components [5].

The reliability and longevity of these power transformers plays a critical part in the performance of the power grid. Therefore transformer manufacturers should ensure that the design and manufacture of these power transformers conform to international standards [6] [7]. Equally as important is the responsibility of the power utility to protect and maintain these transformers while in operation in its power grid.

A major concern in power grids regarding the safe operation of system components is the occurrence of voltage transients and overvoltages. These conditions are usually caused by current interruptions due to circuit breaker operations, energizing of unloaded transmission lines, load rejection and lightning surges on or near transmission lines [5] [8]. Transient

voltages are capable of disrupting power grids and may cause severe damage to electrical equipment [9] [10].

For many years the modelling of power grid components, when subjected to transient voltages, has been a matter of great interest [11]. Numerous studies have been done on the modelling of transmission lines, surge arrestors, electrical motors and power transformers in order to predict the behaviour of the system [12] [13] [14] [15]. These have enabled engineers and designers to take preventative measures to protect these components.

Power grids are subjected to continual changes. These transformations may be due to the replacement of old equipment, power grid expansion or the change in the behaviour of the demand-side electricity usage [2]. Although these transformations are essential, they pose new challenges in that they change the electromagnetic behaviour of the existing power grid.

If these behavioural changes are not understood, the failure of system components and disruption in power supply due to voltage abnormalities are unavoidable. To circumvent these dangers engineers and designers rely heavily on the accurate modelling of these systems to reduce the impact of transient- and overvoltage occurrences. Hence the availability of accurate electromagnetic models of power grid components such as power transformers is a key factor in ensuring a reliable supply of electricity.

1.2 Project motivation

The insulation structure of a large power transformer should be able to withstand the strain caused by transient voltages. To ensure that the insulation structure is adequate, the transformer is subjected to a variety of standardised factory tests after manufacturing. During these tests the transformer windings are excited with various specified periodic- and aperiodic wave shapes [6] [7].

When these excitation waves contain high frequency components, the capacitive nature of the transformer winding structure becomes noticeable [16] [17] [18]. The presence of these capacitances along with the inductive properties of the transformer winding forms an electromagnetic system of high order. This system is capable of resonating at various excitation frequencies causing voltage amplification in different parts in the transformer winding structure [12] [19] [20] [21]. If these amplified voltages exceed the insulation strength of the insulating materials, dielectric failure may occur.

In reality the standardised wave shapes are not representative of all the transient voltages that power transformers are exposed to. Each occurrence of a lightning- or switching event

is unique in wave shape and amplitude. If the actual occurring transient voltage excitation wave contains a frequency close to one of the major resonance frequencies of the transformer winding structure, dielectric failure is possible even if the transformer passed the specified acceptance tests [9] [22]. Preventative measures such as the implementation of surge arrestors are commonly used to protect power transformers, but are only sensitive to voltage amplitudes. Thus, although an incoming transient voltage wave has an amplitude well below the protection level of the surge arrestor, it is still capable of stimulating resonance behaviour in the winding structure which may cause dielectric failure [10] [22].

Both the power utility and the transformer manufacturer are faced with the challenge of predicting the behaviour of the transformer winding structure when subjected to transient voltage excitations. The transformer manufacturer must design the transformer to withstand the specified factory tests and the power utility must coordinate their system response to avoid unnecessary transient behaviour as far as practically possible.

During the design stage of the transformer unit, the design engineer requires the maximum voltages occurring in and around the winding structure when undergoing factory testing. This information enables the engineer to specify the required electrical clearances, insulation thickness and arrangement of insulation barriers to avoid insulation failure [23] [24] [25] [26]. In addition to this the designer can implement a variety of methods to improve the transient response of the winding structure, such as the use of interleaved- and shielded disk windings and the choice of winding arrangements [27] [25] [28].

The utility on the other hand can mitigate various transient occurrences caused by network switching operations. The impact of switching transient voltages can be lessened by implementing synchronise switching, damping resistors and snubber circuits [9] [29] [30].

In either application there exists the need for an electromagnetic model that can be used to calculate the transient voltage behaviour of the system. The model required is not necessarily the same for both. A reduced two port network model may be sufficient when analysing the power grid behaviour surrounding the transformer [31]. However, a detailed model is required during the transformer design stage. In order for the design engineer to specify the insulation structure, the voltage distribution throughout the transformer winding structure is required [23] [24] [26].

1.3 Project description

1.3.1 Project objective

The objective of this project is to develop an electromagnetic model that can be used to accurately calculate the voltage distribution in a transformer winding structure when excited with standard impulse excitation waves. These voltages are required during the design stage of the power transformer to ensure that the insulation is capable of withstanding the occurring electric field stresses during these tests.

It will be evident from Chapter 2 that the subject matter regarding the variety of transformer geometries, excitation wave types and boundary conditions is substantial. To ensure that the project is manageable, this study will focus on the modelling of a single disk-type power transformer winding. These winding types are common in core-type power transformers and are more complex than the more familiar spiral-type windings. It can be concluded from the literature survey presented in Chapter 2 that the principles applied in the modelling approach followed in this project are also valid for a complete transformer with other winding types. In this regard, the thesis presents a foundation that can be used for modelling the transient voltage behaviour of power transformers to determine the voltage distribution in its winding structures.

1.3.2 Research objectives

It is important to define the various research objectives required for the successful completion of the project. The following research objectives have been identified regarding this matter:

- Development of a proper modelling methodology that can be applied to determine the voltage distribution in a power transformer's winding structure when subjected to transient voltage excitations such as those found during standard factory acceptance tests

- Development of methods to accurately calculate the model parameters. This includes calculations of the self- and mutual-inductances of transformer windings having various geometrical sizes and number of turns. The calculation of other parameters such as the capacitances in and around the winding and the dissipative elements are also required.

- Development of a suitable methodology for modelling non-linear frequency-dependent damping parameters due to stray losses such as iron losses and dielectric losses.

- Identification, implementation and validation of suitable solution methods to simulate the response of the model.

These research objectives form the key elements of this project. Each of these objectives requires the execution of various project tasks to meet the requirements of the project. These tasks include the following:

- Perform a literature study to identify the various modelling approaches used in transient simulations of power transformers. The different model topologies and their characteristics should be reviewed. The survey should include methods used to calculate the self- and mutual-inductances of transformer windings and their capacitive elements. Special considerations such as the flux behaviour in the core during impulse testing and frequency dependant losses should be reviewed and their effect on the model parameters should be investigated in the survey. The conclusions drawn from the literature study will determine the choice of model topology, parameter calculation methods and solution method.

- The calculation algorithms of the model parameters should be implemented in a software environment. A suitable environment must be identified to develop the code required for this project. Program code must be developed to calculate the inductive, capacitive and dissipative elements of a transformer winding from known electrical and geometrical information. The development of program code that creates the mathematical representation of the equivalent electrical circuit model of the transformer winding is required. A solver must be implemented in the program environment to calculate the voltage distribution throughout the winding structure.

- An actual test-unit must be used as a case study. Standard lightning impulse excitation waves should be applied while the voltage distribution throughout the winding is measured. Special considerations regarding good practices when taking measurements should be identified and applied. The interaction between the measuring equipment and the test-unit should be investigated. This includes the input- and output impedance matching of the respective systems. Matters regarding data acquisition and its accuracy such as quantization errors and sampling frequency considerations must be investigated. For the purposes of this investigation, tests will be conducted on an air-core reactor rather than a complex multi winding transformer. This is due to the exploratory nature of the subject matter and the time constraints of the project.

- The methodologies used to calculate the model parameters must be validated. This should be done by comparing results from multiple calculation methods. Finite Element Method (FEM) software should be used in this respect as a benchmark. The geometry of the test-unit must be drawn in the FEM software and appropriate boundary and material properties must be applied. Matters regarding the accuracy of FEM simulation results and their interpretation should be addressed. These include the sensitivity of the problem to the size of the mesh elements as well as the effect of the boundary conditions.

- A method of generating the excitation waves mathematically should be investigated and implemented. The function parameters required should be calculated depending on the required wave properties.

- The accuracy of the solver algorithm must be evaluated by comparing the solver output to another solution method. Both the time- and frequency-domain should be compared to determine the reliability of the solver. The matters contributing to the solver accuracy should be identified and applied to achieve reliable results.

- The voltage distribution measured along the winding of test-unit should be compared with the calculated voltages. This requires careful evaluation of the results in both the time- and frequency-domain. To ensure the correct interpretation of the processed signals, digital signal processing (DSP) methods, including application of the Fast Fourier Transform (FFT), must be reviewed. The DSP operations should take due cognisance of the properties of the input signal, e.g. frequency bandwidth and dynamic range.

- Upon completion of the project, areas of improvement must be identified to reduce or mitigate the discrepancies found when comparing measured and calculated results. Possible research opportunities should be clearly identified that will complement the outcomes of this project.

1.4 Thesis outline

Chapter 2 presents a critical literature survey on the modelling methods used for transient analysis. This requires a review of the power transformer architecture and the nature of transient voltages in power systems. Methods for determining the model parameters are also reviewed. The mathematical model representation and solution methods used in transient voltage studies are discussed. Important considerations regarding practical

measurements are discussed as well as some fundamental digital signal processing principles.

Using the principles discussed in Chapter 2, the development of the electromagnetic model is presented in Chapter 3. Initial discussions revolve around the choice of model type and the level of discretisation. Capacitance and inductance calculations are implemented and validated by means of finite element modelling. Chapter 3 also includes the method in which the damping of oscillating voltages in windings is modelled.

Chapter 4 presents the solvers used to evaluate the mathematical model of the electromagnetic system. The solver algorithms are implemented in a MATLAB environment. The results obtained using two different solving methods are compared in both the time- and frequency-domain.

The complete modelling approach is applied to a case study to validate the accuracy of the model and assess the performance of the different solvers. The experimental setup used to measure the voltage distribution at multiple positions along the test-unit is presented in Chapter 5. The measured and calculated results are compared in both the time- and frequency- domain.

Chapter 6 concludes the thesis by comparing the initial research objectives with the actual outcome of the project. The deviations between calculated and measured results are carefully evaluated and attributed to possible causes. Recommendations are made with regards to future research.

Chapter 2 Literature review

2.1 Overview

This chapter presents the supporting literature that pertains to the modelling of transient voltage behaviour of power transformer windings. A detailed description of the different components of a power transformer is presented, followed by a discussion on the causes and characteristics of transient voltages occurring in power grids. A historical overview is presented regarding the evolution of transformer modelling for transient voltage analysis. The methodologies of determining the model parameters and their effect on the transient voltage behaviour of the modelled transformer are presented. These matters will lay the foundation required to construct a suitable model to achieve the goal of this study. The chapter concludes with a discussion regarding considerations when taking practical measurements. Some considerations regarding digital signal processing and analysis are also reviewed.

2.2 Power transformer anatomy

2.2.1 Introduction

Generally two types of transformers are referred to in the power engineering industry namely distribution transformers and power transformers. Currently no clear definition exists in international standards that distinguish distribution transformers from power transformers [32]. For the purpose of this thesis, the term power transformer will refer to transformers with a power rating of greater than 5 MVA.

The major transformer components discussed in the following sections will be collectively referred to as the active part. The active part consists mainly of the magnetic core, and the winding-block. In accordance with the scope of this project, other external components such as the bushings and harness will be omitted.

2.2.2 Transformer core assembly

The core provides a low reluctance path for magnetic coupling between the primary and secondary windings. Power transformers have mainly two types of core constructions namely shell- and core-type [25] [24]. This dissertation will exclude shell type transformers since the physical construction between shell- and core-type transformers are completely different.

The most common assembly used in three phase core-type power transformers is the three-limb core as shown in Figure 2-1. Each phase is associated with its respective main limb. The main limbs of the three phases are magnetically connected via the horizontal top and bottom yokes [24] [28]. The operating flux density of these transformer cores are in the region of 1.7 Tesla. Both the core and its clamping structure are held at ground potential [33].

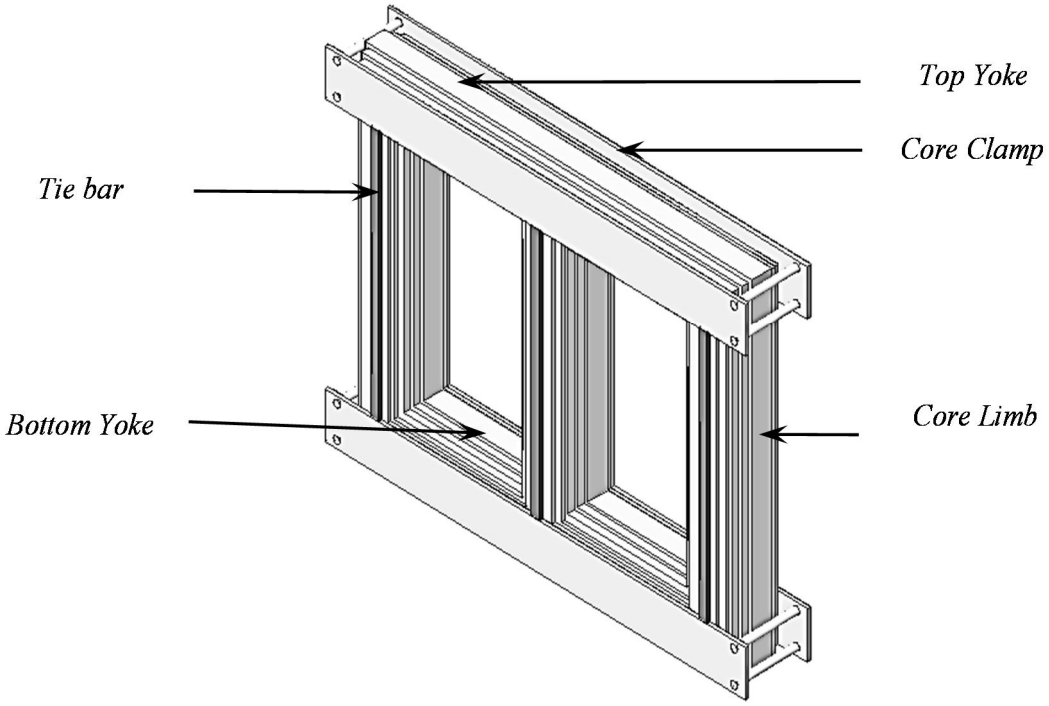

Figure 2-1: Three-limb laminated transformer core

The core is manufactured using silicon steel with low carbon content. The presence of the silicone crystalline structures reduces hysteresis losses and increases the permeability of the steel. Eddy current losses are reduced by constructing the core with laminated steel sheets that are coated with a thin layer of insulating material. The thickness of these laminated sheets varies between 0.3 and 0.25 mm and they have a silicon content of approximately 3 $\%$. The core laminates are held together by a steel clamping structure and tie bars [24] [23] [34].

The stacked laminated core forms a stepped cross section approximating a circular form. The stepped profile and insulation coating on the laminates cause a loss in effective cross sectional core area with reference to the gross cross section. This ratio of effective- to gross

area is known as the space factor. For economic reasons it is crucial to maintain a high space factor to ensure effective use of the available core area [24] [34].

2.2.3 Insulation material used in power transformers

The insulation used throughout the active part of the transformer is mostly made from cellulose material. The cellulose material is obtained from processed timber [25]. The fibres in the cellulose material are made up of long polymer chains that enable the material to have a measure of elasticity [35].

The winding conductors and exit leads are covered in kraft paper. *Kraft* paper provides the required electrical insulation around a conductor. Fixtures providing mechanical support in and around the winding structure can be made of pressboard which is manufactured from compacted processed cellulose fibres to form a hard ridged material [28] [35].

The complete active part is submerged in transformer oil. The oil serves as a coolant and as an insulation medium since its breakdown strength is considerably higher than that of air [36]. The oil penetrates the cellulose structure of the pressboard and paper to form a composite insulation structure [35]. The oil also retards the ageing of the cellulose material.

It is very important for the cellulose material and the transformer oil to have a low content of moisture. Moisture reduces the electric strength of the insulation material and accelerates the rate of aging of the cellulose material. Ageing causes the breakdown of the polymer chains in the cellulose structure which jeopardises the mechanical strength of the material. The preferable moisture content of cellulose insulation material should be no more than 5 % [35] [25].

The choice of insulation material is very important when considering a composite insulation structure, especially with reference to the different dielectric constants of the materials. The dielectric constants of the materials should be as close as possible to each other in order to avoid electric field density enhancement due to dielectric displacement [37]. In general, mineral oil with a relative permittivity (ε_r) of 2.2 is used along with paper and pressboard which has a ε_r of 3.5 and 4.4 respectively [35].

2.2.4 Winding-block assembly of power transformers

2.2.4.1 Description of the transformer winding-block

The winding-block refers to all the windings such as the high voltage (HV), low voltage (LV) and regulating windings pertaining to a specific phase. The windings are wound on circumferentially spaced ribs supported by a pressboard cylinder known as the *former-*

cylinder [32]. These windings are slid over each other, forming a concentric configuration that encloses the core limb as shown in Figure 2-2 and Figure 2-3 [38] [23]. The windings are separated with vertical ducts required for electrical clearance and to allow oil to flow along the height of the winding for cooling [24]. The oil ducts have multiple pressboard barriers residing in them, forming a composite insulation structure as presented in Figure 2-3 [23].

The winding-block is held securely in place by a clamping structure as shown in Figure 2-4, consisting of clamping rings made from pressboard [25]. These plates are inserted during assembly while applying an axial force on the windings. When the applied force is removed, the plates maintain a constant pressure on the windings. This is done to ensure that the winding structure remains rigid when subjected to electromagnetic forces during short-circuit events [24] [25].

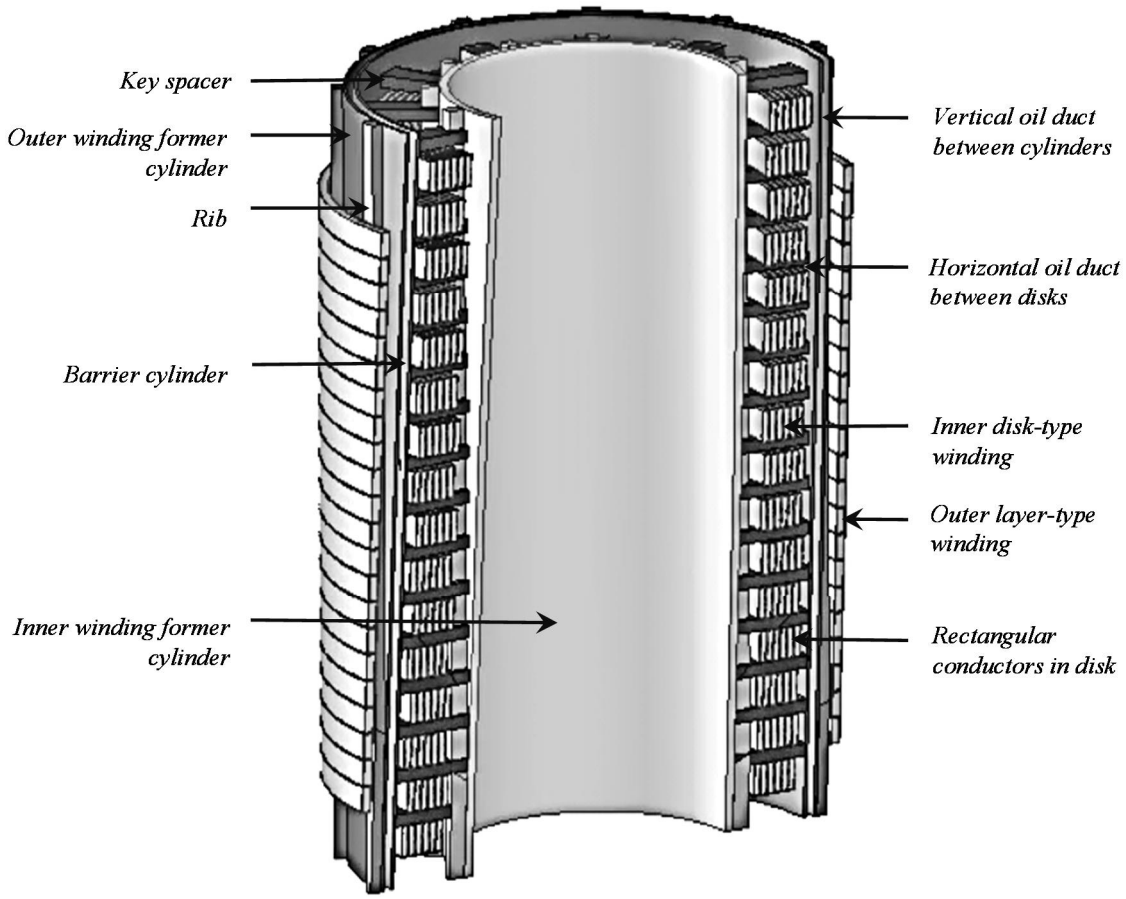

Figure 2-2: Complete power transformer winding-block assembly

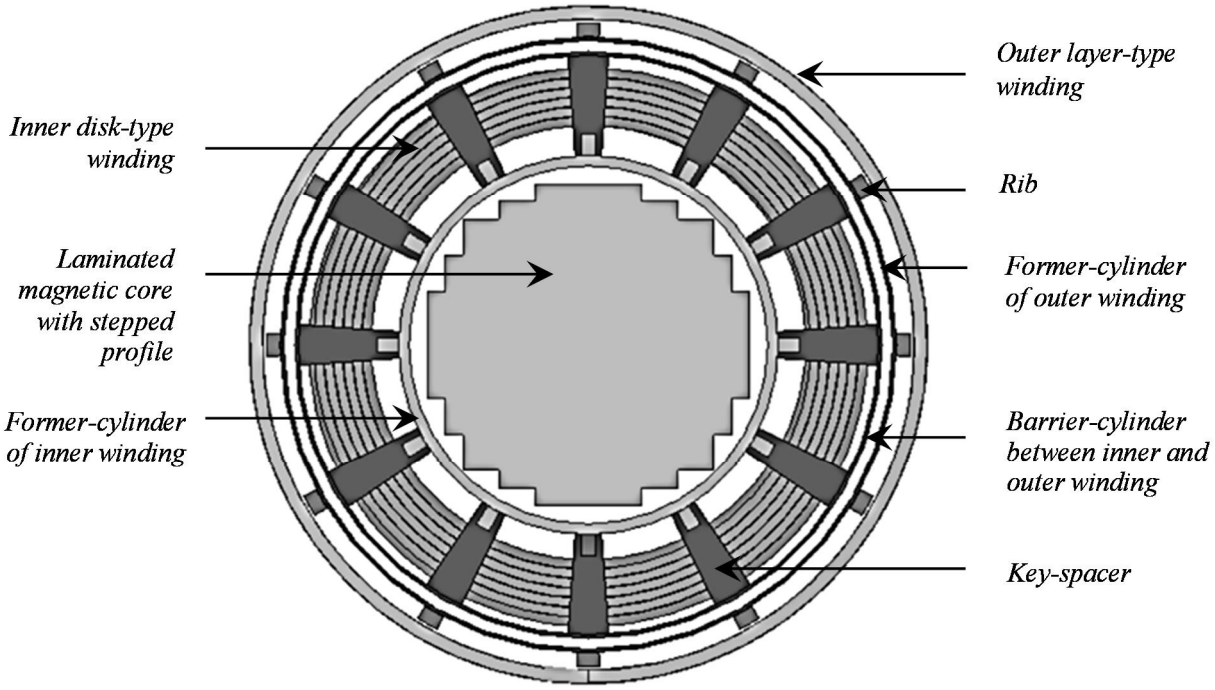

Figure 2-3: Concentric arrangement of winding-block

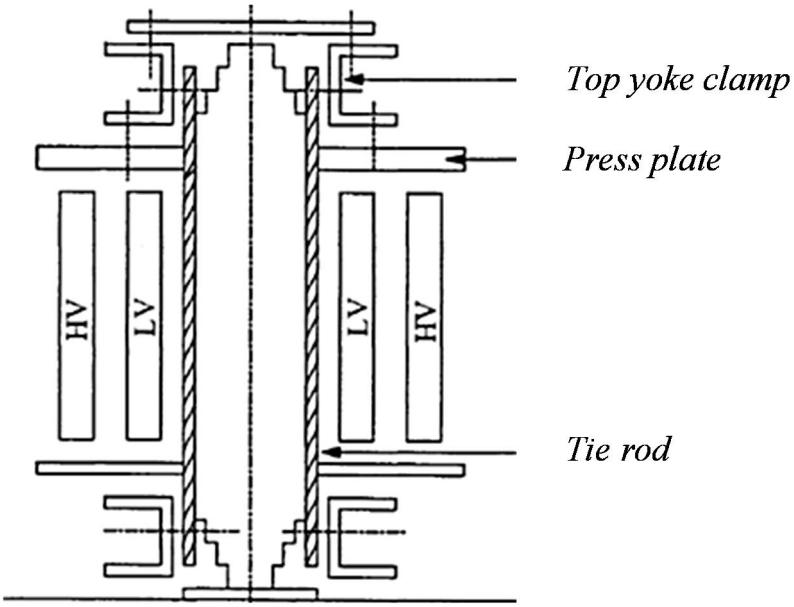

Figure 2-4: Winding clamping structure [25]

2.2.4.2 *Winding types commonly used in power transformers*

In essence there are two common winding construction methods when referring to core-type power transformers namely spiral- and disk-wound windings [28] [34].

Spiral-type windings are wound continuously from the bottom to the top. The turns may be wound directly adjacent to each other to form what is commonly referred to as a *layer-winding* as presented in Figure 2-5 [23] [24]. Alternatively, *key-spacers* may be placed around the circumference between turns to increase the cooling surface. These windings are mostly referred to as helical-windings [32]. Spiral windings are mostly used in LV windings and are capable of carrying large currents due to the large cooling surface of each conductor [34].

Disk windings consist of pancake-like coils known as disks as presented in Figure 2-5. During the manufacturing of these windings a certain amount of turns are wound radially before crossing over to the next disk as shown in Figure 2-6 [24] [25]. The disks are separated by key-spacers creating radial ducts which allow oil flow for cooling purposes. Disk windings are typically used in HV winding applications since it is possible to have a multitude of electrical turns in a relatively small axial direction [34].

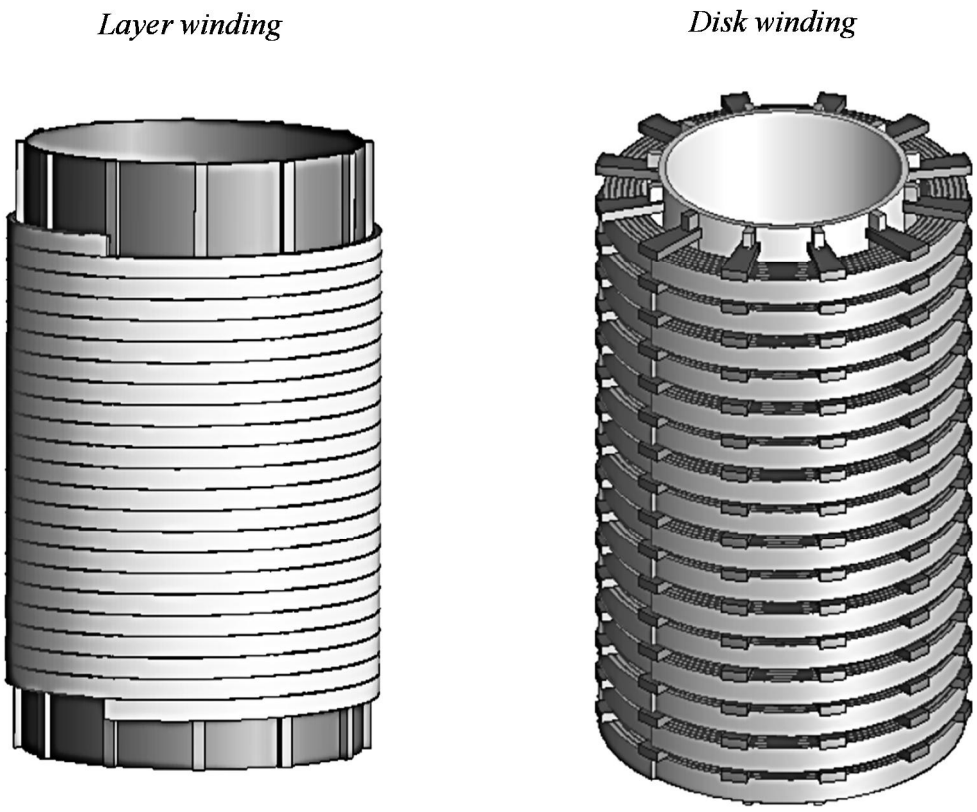

Figure 2-5: Layer- and disk-type winding representation

A matter to consider when specifying a disk winding is that the cross-overs as shown in Figure 2-6 causes a part of the electrical turn in the disk to be lost. Cross-overs are staggered to distribute them around the winding to ensure mechanical stability. The staggering is done by starting the cross-over one or multiple pitches prior to the previous cross-over. A pitch refers to the distance between the middle of two adjacent spacers or ribs. Thus the transition from disk A to disk B requires the conductor to cross over before revolving a full 360º.

The number of turns lost due to staggering can be calculated if the total number of spacers around the circumference of the winding (N_{sp}) is known as well as the number of pitches used for staggering (N_{pitch}). If a winding has n disks, $(n-1)$ cross-overs are required. A full turn will cover all the pitches around the circumference. The fraction of the turn that is lost k_{lost} due to the staggering is then:

$$k_{lost} = \frac{N_{pitch}}{N_{sp}}. \tag{2.1}$$

This fraction is lost at every cross-over and so the total number of turns lost is:

$$N_{lost} = (n-1) \cdot \frac{N_{pitch}}{N_{sp}}. \tag{2.2}$$

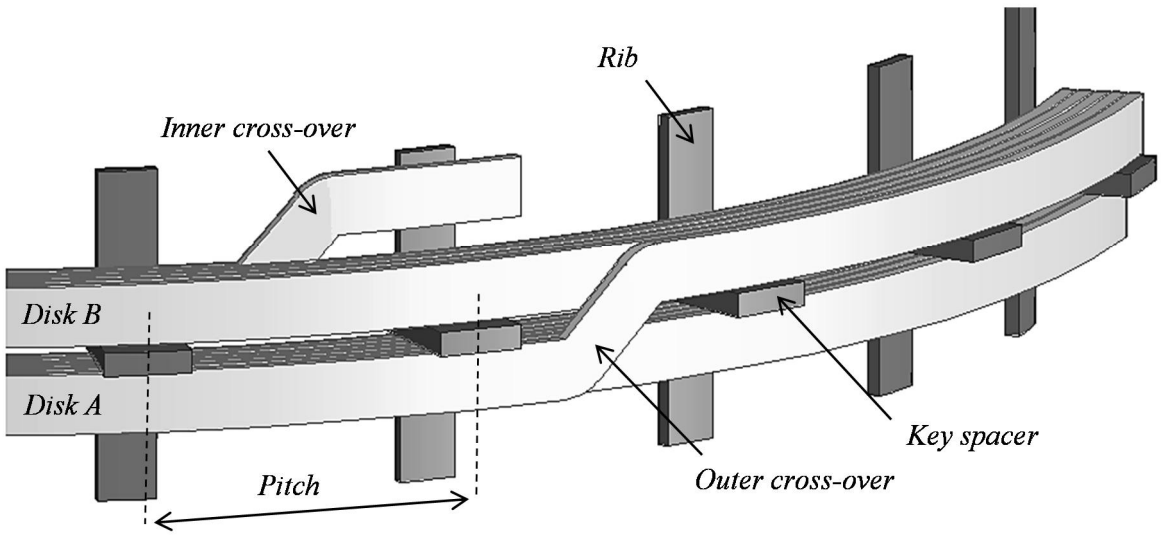

Figure 2-6: Cross-overs in disk-type windings [24]

A great advantage of disk windings in high voltage applications is the ability to interleave electrical turns. Interleaving entails the non-sequential ordering of electrical turns as

presented in Figure 2-7 [27] [39]. Interleaved windings may reduce the non-linear transient voltage behaviour of the winding as will be seen in subsequent discussions. Floating conductors can also be wound in disk windings - known as wound-in-shields - to improve the transient voltage distribution along the winding [28].

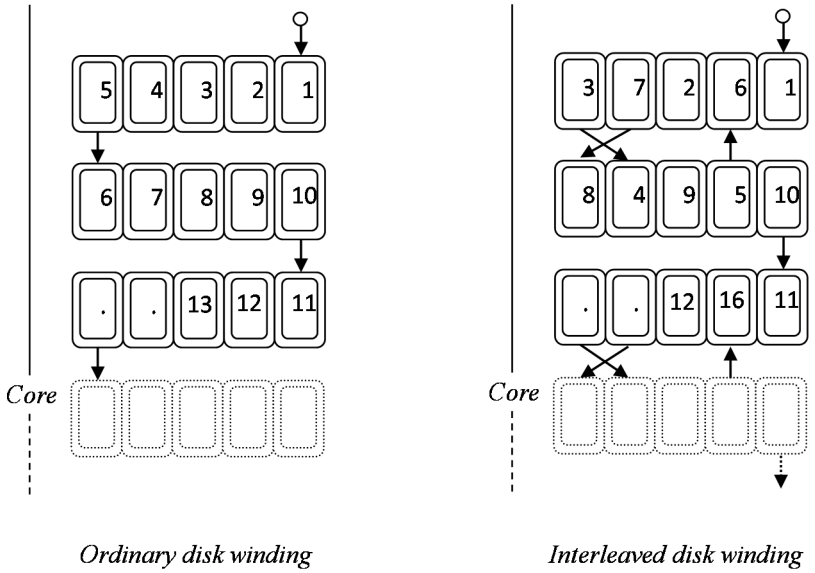

Figure 2-7: Turn configuration of ordinary- and interleaved disk windings [27]

2.2.4.3 Conductors commonly used in transformer windings

The conductors used in the windings are typically rectangular in cross-section and insulated with cellulose paper. Copper is the preferred conductor material due to its mechanical strength concerning short-circuit forces, but in some cases aluminium could also be used [32] [34].

High winding currents result in heat generation due to the winding resistance. These losses can be reduced by increasing the cross sectional area of the conductor. However since the windings are situated in an oscillating magnetic field, eddy currents are formed on the conductor surface. If the cross sectional area of the conductor is increased the outer surface becomes larger increasing the losses caused by eddy currents [23].

To address this challenge, multiple conductors can be used in parallel rather than increasing the cross sectional area of one conductor. Other means of reducing eddy losses in windings while maintaining a large cross sectional area is by using Continuously Transposed Conductors (CTC). This is a special type of conductor that contains multiple enamel coated rectangular strands that are periodically transposed as presented in Figure 2-8 [32].

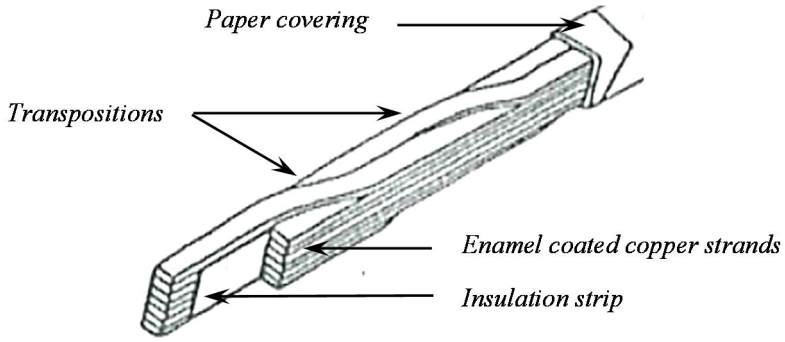

Figure 2-8: Continuous Transposed Conductor (CTC) [32]

Transpositions of parallel conductors or strands are necessary to ensure that the same amount of flux is enclosed by the parallel conduction paths. If this is not done a potential difference will occur between the parallel paths resulting in circulating currents. This would cause additional losses in the windings [32] [24]. When multiple conductors are used in a disk winding, the conductors are transposed at the cross-over to avoid circulating currents.

2.3 Transient voltages in power systems

2.3.1 Origin and characteristics of transient voltages

A power transformer is exposed to various abnormal transient voltages during its operation in a power grid. Transient voltages are caused by various events in the network such as lightning surges, current interruptions by circuit breakers, energization of various network components and faulty conditions in the network [5] [15]. These transient voltages may either have aperiodic- or periodic wave shapes and can have amplitudes much higher than the transformer's rated operating voltage.

The classification of transient voltages is not a trivial matter since almost every transient voltage event is unique with reference to its wave profile and amplitude. Therefore the most practical method of distinction is with reference to the frequency content of the transient wave. Transient voltages can be classified into four groups namely low-frequency oscillations, slow-front surges, fast-front surges and very fast-front surges [40].

Low-frequency oscillations range from 0.1 Hz to 3 kHz. These oscillations are typically caused by inrush currents when transformers are energized [41]. The transformer core may have had a remnant flux after its former disconnection [24]. When energised this may cause the core to saturate causing harmonic disturbances on the excitation voltage [25].

Slow-front surges contain frequencies between 50 Hz and 20 kHz. Switching of capacitor banks is a typical cause of these surge types [30]. The circuit in which the capacitor bank

resides contains inductive properties forming a resonance circuit. The instantaneous application of the excitation voltage may stimulate the natural frequency of the circuit resulting in oscillatory overvoltage [5].

The frequencies of fast-front surges range from 10 kHz to 3 MHz and are usually caused by re-ignitions during circuitbreaker operations. These are caused by the residual voltage stored in the capacitance of supplied network after the contacts of a circuit breaker separated. These arcs may strike repetitively causing oscillatory voltage waves [5]. Fast-front surges may also be caused by lightning impulses on or near power grid components [10].

Very fast-front surges are mostly found in Gas Insulated Substations (GIS) during the switching events of disconnectors. The frequency content or these wave forms ranges between 100 kHz and 500 MHz [8].

2.3.2 Standardised waves shapes

The standard lightning impulse (LI) wave profile as shown in Figure 2-9 [7] can be approximated with a double exponential function. The instantaneous voltage $v(t)$ is expressed as [42] [43]:

$$v(t) = k_k\left(e^{-\alpha_k t} - e^{-\beta_k t}\right), \qquad (2.3)$$

where the parameters α_k, β_k and k_k are dependent on the rise time t_f and the time taken t_{50} to drop to half the crest value. The rise time is defined by the duration that it takes the signal to rise from 30% to 90% of its peak value V_{peak} where both values are evaluated respectively at t_{30} and t_{90}. The parameters in equation (2.3) can be solved by means of the Newton-Rapson method as shown in Appendix A. The standard LI is used in routine factory tests and has a t_f of 1.2 μs and a t_{50} of 50 μs [6] [7].

Another common transient voltage wave used for testing, is the standard lightning impulse wave with a chopped tail (LIC) as presented in Figure 2-10. This wave profile is generated by collapsing the full wave voltage at an instance t_c. The LIC is not currently a mandatory test according to international standards, but some customers may request it as a special test. To generate a LIC the LI wave profile is chopped at t_c ranging between 3 to 6 μs [7].

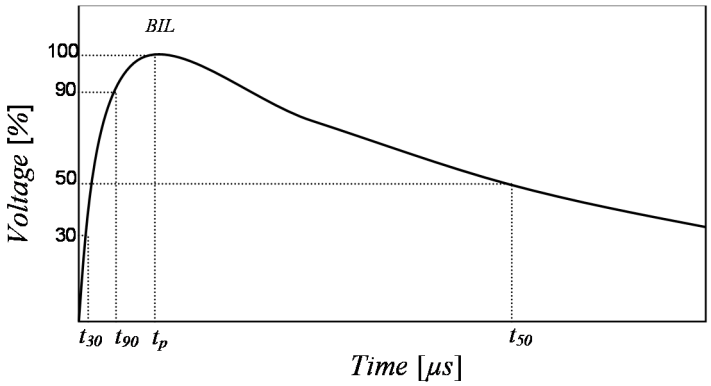

Figure 2-9: Standard full wave lightning impulse [7]

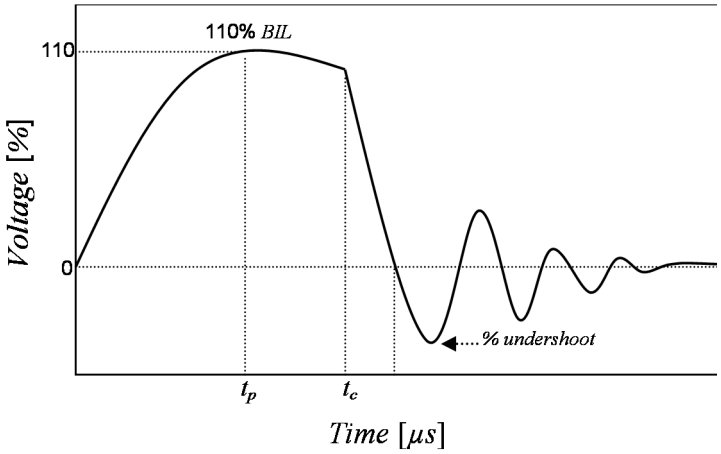

Figure 2-10: Lightning impulse wave with chopped tail [7]

2.4 Electromagnetic behaviour of transformer windings

2.4.1 Classification of winding response

During normal power frequency excitation the voltage distribution along the winding is nearly linear. The voltage distribution is governed by the turn ratio and resistive losses along the length of winding [25]. This is the typical inductive behaviour of a winding during low frequency excitation.

When a transformer winding is excited with a voltage wave form with a steep front the voltage distribution throughout the winding is non-linear as presented in Figure 2-11 [44]. The transient voltage behaviour is categorised into three distinctive periods namely the initial-, transient- and pseudo-final response [17] [18] [45]. Each of these periods are governed respectively by the winding's capacitive, inductive and dissipative nature [46].

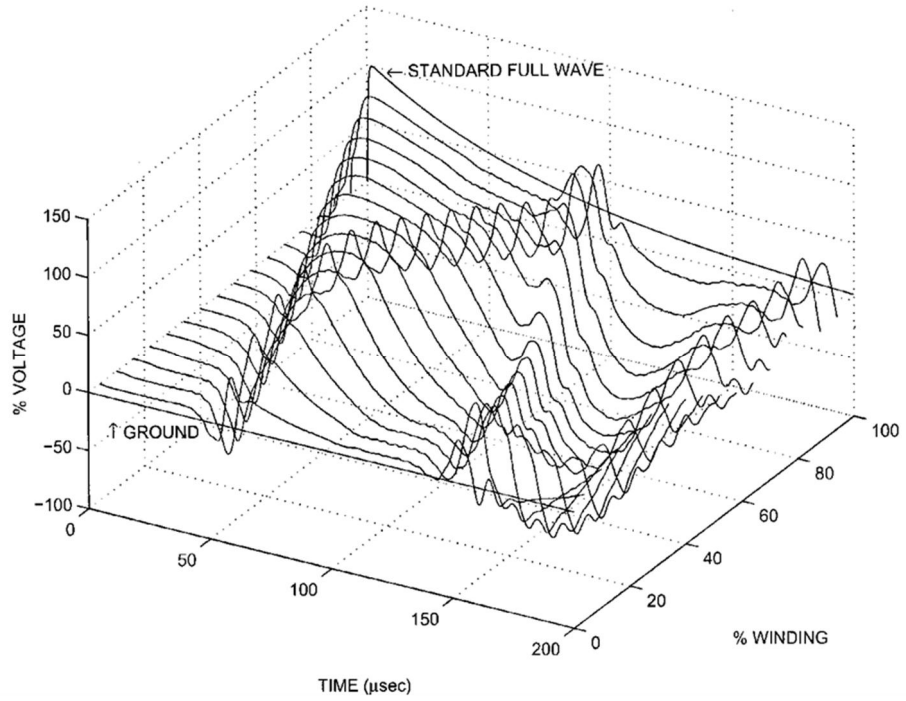

Figure 2-11: Transient voltage response for 100 disk winding [44]

2.4.2 Inductive behaviour of transformer windings

2.4.2.1 Background theory on inductance

During normal power frequency operation, the prominent behaviour of a transformer is inductive [16] [17]. The inductance of a winding is governed by the distribution of magnetic flux in the region enclosed by the winding. A current flowing along a closed contour produces a magnetic flux $\bar{B}_1$ in the enclosed surface a as presented in Figure 2-12 [47]. The self-inductance L_{11} of the contour having N_1 turns is defined by the relation [48]:

$$L_{11} = \frac{N_1}{I_1} \int da \cdot \bar{B}_1 . \qquad (2.4)$$

If two current contours are in close proximity of each other enclosing a surface a they will couple magnetically with each other. The mutual-inductance L_{12} due to the flux $\bar{B}_2$ set up by the current I_2 in nearby loop, can be expressed by the equation:

$$L_{12} = \frac{N_1}{I_2} \int da \cdot \bar{B}_2 . \qquad (2.5)$$

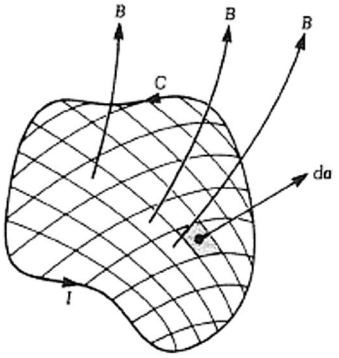

Figure 2-12: Current contour enclosing [47]

The magnetic field can also be influenced by nearby ferromagnetic material. If a ferromagnetic material is placed in the magnetic field enclosed by the current contours, the magnetic domains of the material will line up with the magnetic field [47] [49]. This causes the magnetic material to act as an induced magnetic source further enhancing the magnetic field. Hence the presence of the magnetic material will cause the inductance of the circuit to increase since the total magnetic flux in the enclosed region increases. It is therefore critical to evaluate the magnetic flux behaviour in and around the winding-block of a power transformer when determining the inductance parameters.

The magnetic flux distribution in the core and winding-block depends on the loading conditions of the transformer [32] [24]. If the transformer is unloaded most of the magnetic flux resides in the core. However, under operating conditions with a lagging load current, the magnetic flux in the core leaks into the winding structure as shown in Figure 2-13 [32] [50]. This leakage flux is a portion of the flux created by both windings that does not link with each other.

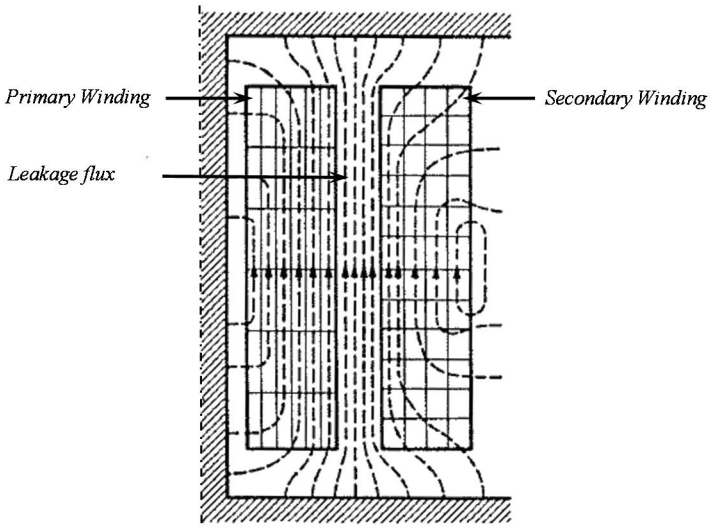

Figure 2-13: Leakage flux distribution in winding structure [24]

2.4.2.2 *Classical analytic inductance calculations*

The effect of the iron-core is neglected in various inductance models used for voltage transient studies. When the winding structure is excited with an impulse, the inability of current to change instantaneously through an inductor implies that a negligible amount of flux will be set up in the core during the initial-response period [51]. Another matter to consider is that the effective permeability of the core steel decreases at higher frequencies [16] [52] [53]. Considering these matters, many inductance models assume an air-core.

Maxwell introduced an analytical formula for calculating the self-inductance of an air-core coil with a rectangular cross section [54]. Lyle improved the accuracy of this analytical formula by approximating the conductor with multiple current-carrying filaments [54]. The self- and mutual-inductances of these filaments were calculated by means of the elliptic integral formula from which the total self-inductance of the conductor was derived. In some applications a single current-filament representation of each turn of the conductor in a coil was sufficient [23]. The method proposed by Lyle could also be used to calculate the mutual-inductance between two rectangular conductors based on work done by Rosa [55].

The evaluation of these analytical formulas was a cumbersome exercise in early studies due to the absence of digital computers. For this reason Grover wrote a publication on inductance calculations by means of tabular data [56] [57] [58]. However, tabular data are valid only for a limited variety of conductor configurations and some inaccuracies become noticeable when working with peripheral tabular data [59].

2.4.2.3 *Analytical iron-core inductance calculations*

The presence of the iron-core can only be ignored under certain circumstances. When the secondary winding is short circuited – as done during standard LI testing [7] – the currents produce a magnetic flux in the core opposing the main flux. Thus, no flux resides in the magnetic core and it can be assumed to be air [60]. However, if the terminal conditions of the winding allow flux to form in the iron-core, the inductive behaviour of the winding structure changes significantly [60]. The reduced effective permeability of the iron-core at high frequencies also does not disqualify the iron-core's effect. Even at excitation frequencies of 1 MHz the effective permeability of the core is still a contributor to the magnetic flux behaviour [61].

The importance of considering the presence of the iron-core became evident in studies done by Abbeti [20]. His publications show that the iron-core has a significant effect on the

mutual-inductances. With the use of air-core models, the mutual-inductance was often omitted or considered only for adjacent turns [18] [52].

Abbeti measured the natural frequencies of windings with and without a magnetic core and compared them to his calculated results. He first considered no mutual coupling between any conductors followed by considering coupling to only the immediate adjacent turns. His final comparison was done by evaluating the mutual inductive coupling between a conductor and the two consecutive turns on either side. His study showed that the measured natural frequencies of a winding with an iron-core correlate better with the calculated frequencies when mutual-inductive coupling is considered between non-adjacent turns due to the presence of the iron-core [20].

Abbeti attempted to use an iron-core inductance model in an electromagnetic model of a transformer winding [62]. His work was based on empirical data showing that a winding having an iron-core can be approximated with an equivalent air-core having a larger diameter [63].

Analytical methods for calculating winding inductance with an iron-core remain a challenging exercise due to the non-linear behaviour of the core. Rabins developed an analytical method for calculating the magnetic flux distribution in the presence of an iron-core. By calculating the vector potential $\bar{A}$ in a region with a relative permeability of μ_r and a current vector $\bar{\imath}$ where:

$$\nabla^2 \cdot \bar{A} = -\mu_o \mu_r \bar{I}\,, \qquad (2.6)$$

he derived the inductance from the flux distribution in the evaluated region. As boundary conditions he assumed that the flux was radially unbounded in the top- and bottom yokes that the core had an infinite permeability [64]. Hence no radial flux component exiting the core was considered.

Other analytical methods used in transient studies used a different approach. These methods mainly revolved around adding a term to the calculated air-core flux. The correction term represents the induced flux generated by the magnetic core and the change in the magnetic field outside the winding [59] [65].

2.4.2.4 Numerical inductance calculations

Alternative methods of calculating inductance are by means of Finite Element Modelling (FEM) using two or three dimensional geometries [25] [66]. These simulations should be performed with careful consideration regarding the meshing criteria and specifications of the

boundary conditions. The sensitivity of the required results to the mesh size and boundary conditions, is determined by recursively evaluating the results after successive changes in the mesh size or boundary condition [25].

The inductances between the various current carrying conductors are calculated by recursively applying a per unit ampere excitation to each conductor while the other conductors contain no current [66]. The return path of the current is assumed to be outside the problem region. For each recurrence the stored energy W_{ij} between two sections i and j, due to the current I_i, are calculated from which the mutual-inductance L_{ij} is derived using the relation [25] [28]:

$$W_{ij} = \frac{1}{2} L_{ij} {I_i}^2 . \qquad (2.7)$$

2.4.2.5 Inductance calculation considerations

During high frequency excitation the current does not distribute uniformly in the cross section of the conductor [47] [50]. This displacement of current affects the magnetic flux distribution in and around the conductor which results in a change of inductance [65] [67]. In light of this, when the above mentioned methods are used it should be acknowledged that the calculated inductance is only valid for a limited frequency range.

2.4.3 Capacitive behaviour of transformer windings

2.4.3.1 Origin and classification of winding capacitances

When a winding is excited at very high frequencies such as those found in steep fronted voltage waves, it behaves like a capacitor [16] [11] [18] [51]. It is established that the capacitive behaviour of the transformer winding governs approximately the first 0.1 μs [39] [27] [45]. Traditionally the capacitances in a winding structure have been divided into three distinct types [38]. In this thesis these capacitances will be respectively referred to as series-, shunt-, and ground-capacitance.

Adjacent turns have surfaces facing each other separated by a composite insulation of mineral oil and paper. This configuration provides a space in which an electrical charge can be stored. An electrical charge can also be stored between consecutive disks. These capacitive structures collectively form what is known as the series-capacitances C_s of a winding [27] [39].

The concentric configuration of the windings as shown in Figure 2-3, forms a similar structure as found in a cylindrical capacitor. Capacitive coupling occurs between adjacent windings which are commonly referred to as shunt-capacitances C_p [14] [46].

Another capacitive component that plays an important role in the transient behaviour is the capacitive coupling of the complete winding structure to ground C_g [17]. This capacitive coupling mainly occurs between the inner-most winding to the core limb and the outer winding to the tank wall.

The contribution of the capacitances in and around the winding structure became evident in studies done by Blume and Boyajian when observing the voltage distribution throughout the winding during the initial response time [17]. The initial transient voltage response of the winding is largely dependent on the ratio of the ground-capacitances to the series-capacitance in the winding. For a unity voltage step wave the initial voltage distribution as presented in equation (2.8) is governed by the gradient factor α presented in equation (2.9) [17] [18].

For a winding with a grounded neutral, the voltage along the winding length l at the position s is shown in Figure 2-14 using the relation:

$$v(x) = \frac{sinh(\alpha x)}{sinh(\alpha)} \tag{2.8}$$

where:

$$\alpha = \sqrt{\frac{C_g}{C_s}} \tag{2.9}$$

and

$$x = \frac{s}{l}. \tag{2.10}$$

The initial voltage distribution for different α values for a winding with a grounded neutral is represented in Figure 2-14. Evidently the voltage distribution is linear if there is no capacitance to ground similar to that of suspension insulators [16]. With a decrease in series-capacitance with respect to C_g, the initial voltage distribution concentrates near the terminal subjected to the surge, resulting in a highly non-linear voltage distribution [68]. The series-capacitance can be increased by reducing the specified distance between disks and adjacent turns, but is constrained by the required electrical clearance.

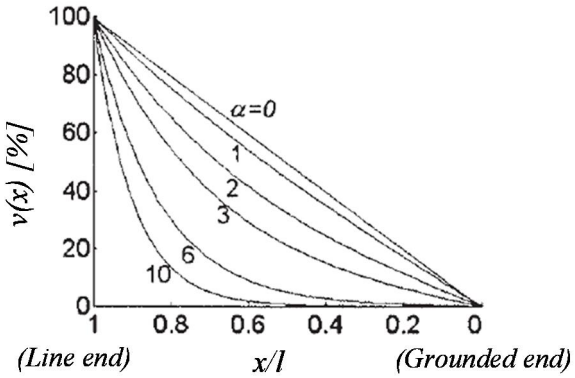

Figure 2-14: Initial voltage distribution of winding with grounded neutral [25]

Alternative methods to increase C_s is to apply the interleaving and wound-in-shields as previously mentioned in 2.2.4.2 [39] [28]. These methods do not directly increase the series capacitance per se, since their effect relies on a turn-to-turn voltage difference which requires inductive current to flow in the winding [27]. However, the initial period is confined to the first 0.1 μs which allows enough time for current flow to create a turn-to-turn voltage difference. Due to the larger turn difference between adjacent turns in interleaved windings, more energy is stored in the initial period of the transient event – thus effectively increasing the series-capacitance. Hence the restructuring of the capacitive coupling between the winding conductors by interleaving or wound-in-shields, does improve the transient behaviour [39] [68].

2.4.3.2 Analytical capacitance calculations

A common practice throughout various studies was to calculate the capacitance between the various elements in and around the winding structure utilizing closed form expressions such as the parallel- or cylindrical plate capacitor formulas [27] [24] [28] [68]. In general, the parallel plate capacitor formula for two plates at a distance d from each other with an overlapping surface area of A is expressed as:

$$C = \varepsilon_0 \varepsilon_r \frac{A}{d}, \qquad (2.11)$$

where ε_0 and ε_r is the vacuum and relative material permittivity respectively. This relation works well where the distance d between the elements is much smaller in comparison to the area A. However, as d increases, fringing occurring at the edge of the surfaces becomes more noticeable [69]. This causes inaccuracies in equation (2.11) if A decreases relative to d. However, more elaborate formulas can be used to account for the fringing at the edges which may yield better results [70].

2.4.3.3 Numerical capacitance calculation methods

As with inductance calculations, FEM also provides an alternative for calculating capacitance. The advantage of this method is that effect of fringing is included in the results. However, this method is much more computationally intensive.

The capacitances between sections such as a conductor and a part of the core is calculated by recursively applying a per unit voltage V_i excitation to each section while the other sections are held at ground potential [66]. The stored energy W_{ij} between two sections i and j is calculated from which the capacitive coupling C_{ij} between them is derived using the relation [25] [28]:

$$W_{ij} = \frac{1}{2} C_{ij} {V_i}^2 . \qquad (2.12)$$

2.4.3.4 Capacitance calculation considerations

The equivalent relative permittivity used in calculating capacitances in and around the winding structure is generally done using fixed dielectric constants for the sake of simplicity. However, this is not the case in practice. The dielectric constants of the insulation materials are a function of the excitation frequency of the electric field in which it resides as well as temperature [71]. Figure 2-15 and Figure 2-16 show the change due to temperature in the relative dielectric constant of mineral oil at various frequencies indicated in Hz above each curve [72].

In composite insulation materials such as oil impregnated paper, additional parameters contribute to the actual relative permittivity of the insulation. These parameters include the densities of the respective materials [72]. For composite insulation structures where each material's dielectric constant is known, the effective relative permittivity can be calculated as presented in section 3.4.2 [24] [37]. This is merely an approximation of the physical system since the dielectric structure is in fact a 3D problem to consider if a higher order of accuracy is required [66].

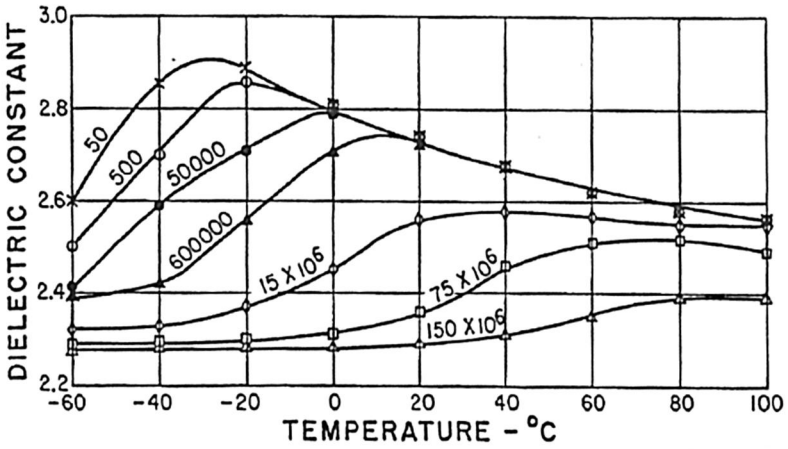

Figure 2-15: Temperature and frequency dependency of transformer oil [72]

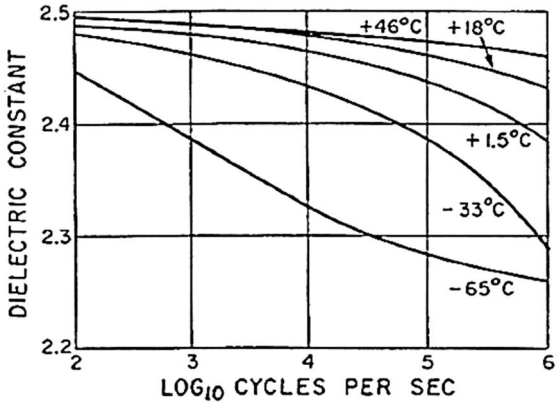

Figure 2-16: Effect of excitation frequency on dielectric constant (oil impregnated paper) [72]

2.4.4 Damping of oscillations due to losses

The currents arising from the transient voltage excitation causes energy dissipation due to the resistive losses of the medium they reside in and can mainly be classified as copper-, core- and dielectric losses. The effect of these losses has already been observed in studies done by early authors Blume and Boyajian [17].

When currents are set up in a conductor the effective copper area decreases with increasing excitation frequency due to the skin-effect. The currents concentrate on the surface of the conductor resulting in higher losses. In addition to this the current in a conductor generates eddy-currents on the surfaces of their neighbouring conductors resulting in the proximity-effect [73] [65]. These two mechanisms primarily cause the losses in the copper conductors. The losses in the core are caused by the eddy-currents set up on the surface of the laminated core by the radial flux component that penetrates the core sheets perpendicularly [53].

Various experimental studies concluded that the high frequency oscillations are highly damped when compared to lower frequency oscillations [41]. Based on this type of experimental data some transient studies implemented frequency dependant damping in an empirical way [14]. The relationship between the damping and excitation frequency is presented in Figure 2-17 [14]. By means of linear curve fitting in Excel, the trend in Figure 2-17 can be approximated by using with the following relation:

$$\alpha_e = 5 \cdot 10^{-8}\omega + 0.0266\,, \qquad (2.13)$$

where α_e represents the damping factor at the frequency ω_k. The assumption in this approach is that the damping can then be represented by a time-frequency dependant windowing function. Assume a discrete time-domain signal $v(nT)$ which are defined for each n point and sampled at intervals of T. The windowing function can then be expressed as shown in the following relation:

$$w(nT, \omega) = e^{-\alpha_e(nT)}. \qquad (2.14)$$

As an example, assume a 50 kHz sinusoidal signal. The damped signal could then be expressed as:

$$v(nT) = 1.0 \cdot sin(50\,000 \cdot 2\pi \cdot nT) \cdot e^{-\alpha_e(nT)}\,, \qquad (2.15)$$

where

$$\alpha_e = 5 \cdot 10^{-8} \cdot (50\,000 \cdot 2\pi) + 0.0266\,. \qquad (2.16)$$

The resulting signal is shown in Figure 2-18. It can be seen that, after approximately 5 μs the signal has been damped by 7.5 $\%$.

Some authors include the losses in their models by means of lumped resistive elements [74]. The calculation of the various damping elements is not a trivial exercise. Valiant efforts were made in many studies to develop or improve loss models for the purpose of transient studies [65] [75].

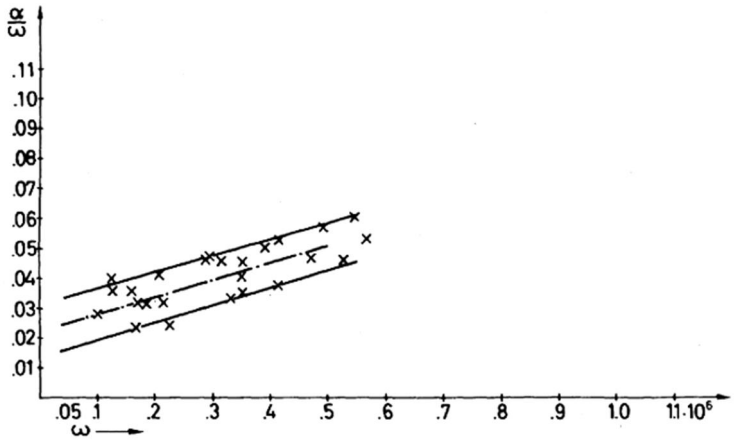

Figure 2-17: Measured relationship between damping and frequency [14]

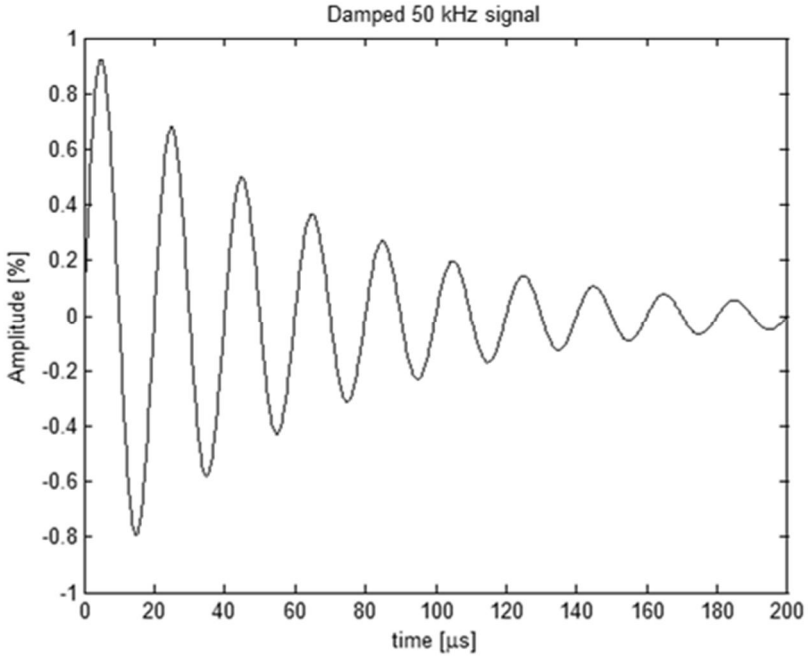

Figure 2-18: Empirically damped signal

The damping phenomenon during transient overvoltages in transformer windings cannot be neglected in a design and manufacturing industry. Damping is inherently the first tier of defence against high voltage oscillations in the winding structure, and therefore plays a significant role when considering the design of the insulation in and around the winding-block.

Due to fact that damping has a negligible effect on the frequency response of the transformer winding, most models omitted the damping behaviour of the physical system completely or approximate its behaviour empirically [20] [14] [76]. The consequence of this was that calculated voltages would be more conservative than those measured in practice.

2.5 Evolution of modelling methodologies

2.5.1 Introduction

The modelling of electromagnetic systems has been approached in various ways. The methodologies are very closely related and present a challenge to separate them into distinctive categories. For the purpose of this study the subject matter regarding modelling methods can be distilled into the classifications presented in Figure 2-19.

The most common modelling methodologies applied to the modelling of transformer windings stems forth from one of two approaches. One approach is based on the assumption that the complete system behaviour can be approximated using an electrical circuit equivalent [14] [41] [24]. The other approach model the system behaviour using electromagnetic field theory [15] [77] [78]. The derivation of these models fundamentally relies on Maxwell's field equations [47].

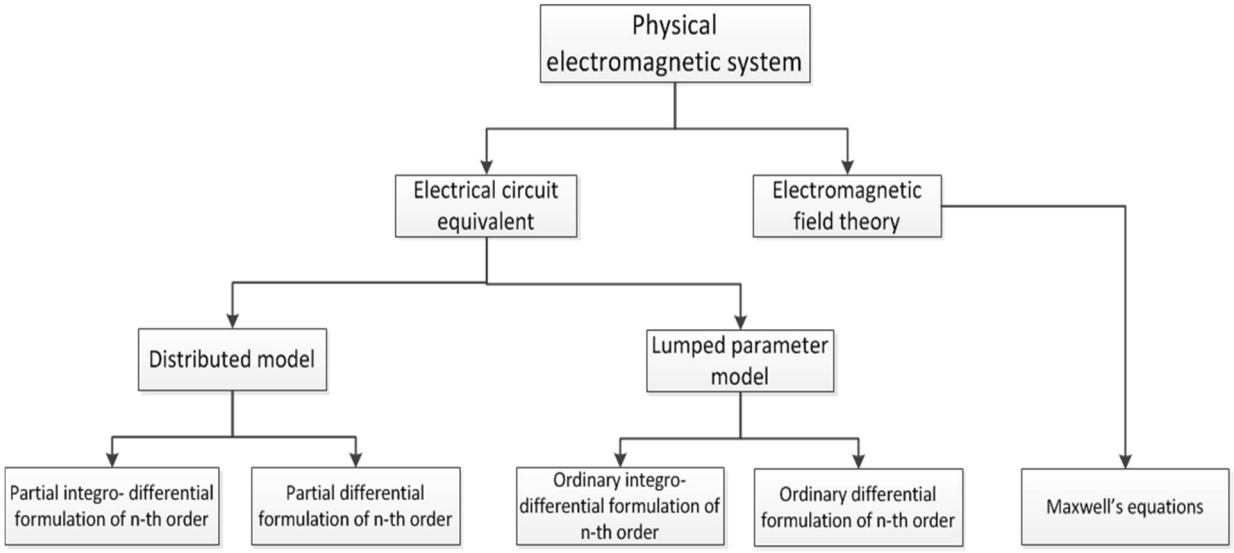

Figure 2-19: Modelling methods of electromagnetic systems

2.5.2 Electrical circuit equivalent models

2.5.2.1 Lumped- and distributed parameter models

Early documented attempts at rising to the challenge started by first modelling the responses of a single winding using an electrical circuit equivalent. The winding was represented by a ladder network of distributed or lumped resistive, inductive and capacitive parameters as shown in Figure 2-20 and Figure 2-21 respectively [16] [17] [52]. Subsequent studies included adjacent windings in the model [12].

Using a distributed parameter model (DPM), the inductance L, series capacitance C_s and capacitance to ground C_g were calculated per unit length dx along the winding. The electromagnetic system behaviour was described by applying Krichhoff's voltage law (KVL) and Krichhoff's current law (KCL). Distributed network models were expressed as partial differential equations (PDEs) or as partial integro-differential equations. The partial differential equation describing the electromagnetic behaviour of a homogeneous system can be written in a higher order relation as [17] [12] [18]:

$$\frac{\partial^4}{\partial x^4} v(t,x) - LC_s \frac{\partial^4}{\partial x^2 \partial t^2} v(t,x) + LC_g \frac{\partial^2}{\partial t^2} v(t,x) = 0\,, \qquad (2.17)$$

where $v(t,x)$ is the voltage at position x along the winding at time t. Partial integro-differential equations were mostly expressed in the frequency-domain and evaluated over a specific frequency range [19].

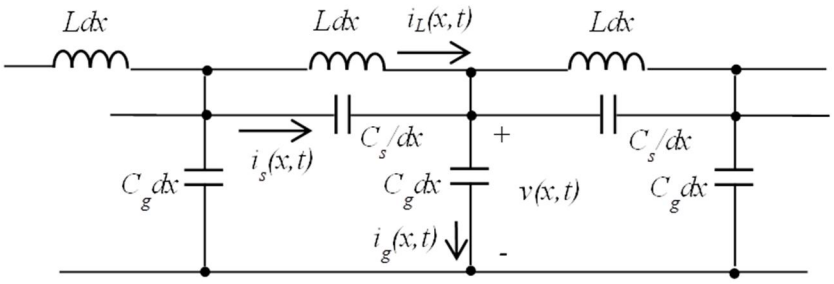

Figure 2-20: Distributed parameter model of a winding (mutual-inductance not shown) [18]

Subsequent models were simplified by grouping parts of the winding into N number of sections resulting in a lumped parameter model (LPM). For a uniform winding the total ground- and series-capacitances, as well as the self-inductance of the winding was divided uniformly along the winding as presented in Figure 2-21. Since the model parameters is no longer a function of position, the model can be represented by a set of ordinary differential equations.

The application of the KCL on a lumped parameter network presented in Figure 2-21 yields a set of ordinary integro-differential equations (IDE). The nodal currents according to KCL are expressed as [18] [74]:

$$[\boldsymbol{C}_n] \frac{d}{dt} \boldsymbol{v}(t) + \frac{1}{[\boldsymbol{L}_n]} \int_{t_1}^{t_1} \boldsymbol{v}(t) \cdot dt = \boldsymbol{I}(t) \qquad (2.18)$$

The $[\boldsymbol{C}_n]$ matrix represented the absolute lumped capacitances between the discrete sections. The entries in the matrix $[\boldsymbol{L}_n]$ represented the lumped self- and mutual-inductances of the discrete sections. The column vector $\boldsymbol{v}(t)$ represents the voltage at each node in the system, while the nodal vector $\boldsymbol{I}(t)$ represents injected nodal currents in the system.

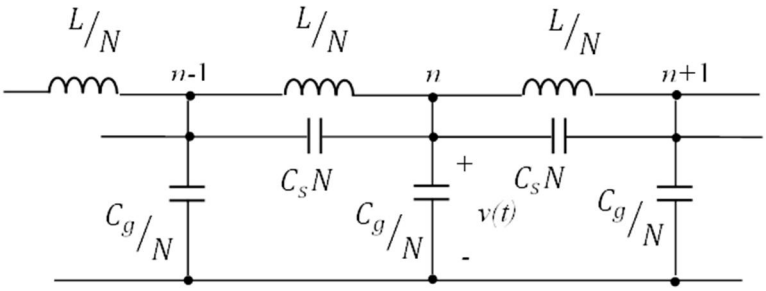

Figure 2-21: Lumped parameter model of winding segment

Modern modelling methods still apply the same principles in that they represent the physical system as a network of either distributed or lumped RLC parameters [59] [79] [26] [80]. Distributed parameter models are limited to windings where the RLC parameters are uniformly distributed throughout the winding. If a winding is not uniform, a cascade of confined distributed parameters can be used. This is done by representing a group of n disks or turns in a uniform part of the winding with a multi transmission line model (MTLM) as shown in Figure 2-22. Groups of these MLTMs are cascaded, forming a hybrid model as shown in Figure 2-23 [26] [80] [79] [81]. In some studies the model order has been reduced by representing the sections that are not of interest with a single transmission line model (STLM) [82] [53]. The sending and receiving voltages and currents ($\boldsymbol{V}_s$, $\boldsymbol{I}_s$, $\boldsymbol{V}_R$ and $\boldsymbol{I}_R$ respectively) are then calculated.

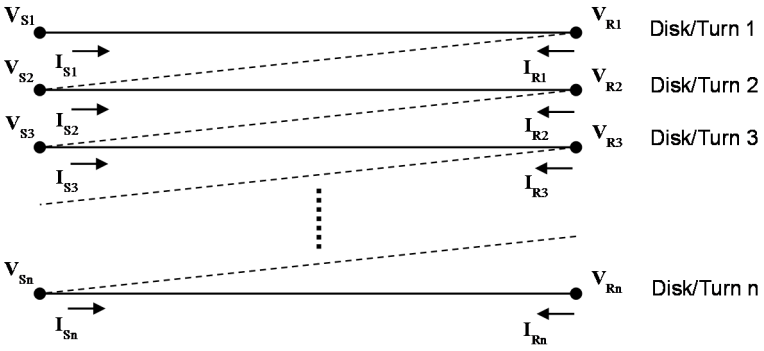

Figure 2-22: MTLM representing a uniform winding segment [81]

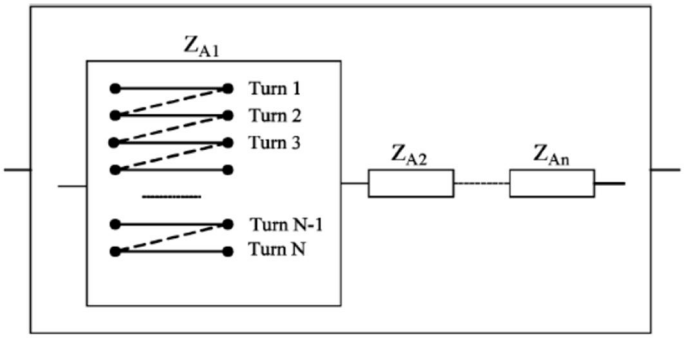

Figure 2-23: Hybrid model of a winding [26]

2.5.2.2 Discretization of transformer windings

2.5.2.2.1 Frequency range dependency

In the application of either the LPM or the DPM it is required to divide the actual winding into fictitious discrete sections where each section is represented as a MTLM or a lumped element. This process is referred to as discretization. The discretization is largely driven by the application of the model and the available computational resources.

Careful consideration must be made in the discretization of the physical system. The desired frequency range plays a significant role in the required length per section [83]. If the physical length l of a section exceeds the wave length λ of the highest required frequency, multiple reflections can occur which would not be noticed at the terminals of the section [84].

The physical length of the conductor represented by a lumped circuit should be much shorter than the shortest required wave length. Good results have been documented where [85]:

$$l = 0.12\lambda\,. \qquad (2.19)$$

The lowest discretization resolution of a physical transformer is obtained when representing the primary and secondary winding with a single inductive branch L_1 and L_2 respectively with their resistances $R_1$and R_2 as presented in Figure 2-24. These types of models are usually used in system studies [86].

Since these model types do not contain nodes along the winding structure, they lend themselfs of little use for transformer insulation design purposes. They do however give a summary of the parameters that need to be taken into consideration at high frequency excitation. C_{12} represents the capacitive coupling between the primary and secondary winding. C_1 and C_2 represents the series capacitance of the primary and secondary winding respectively. The capacitance of each winding to ground C_{w-g} is also an important parameter to consider.

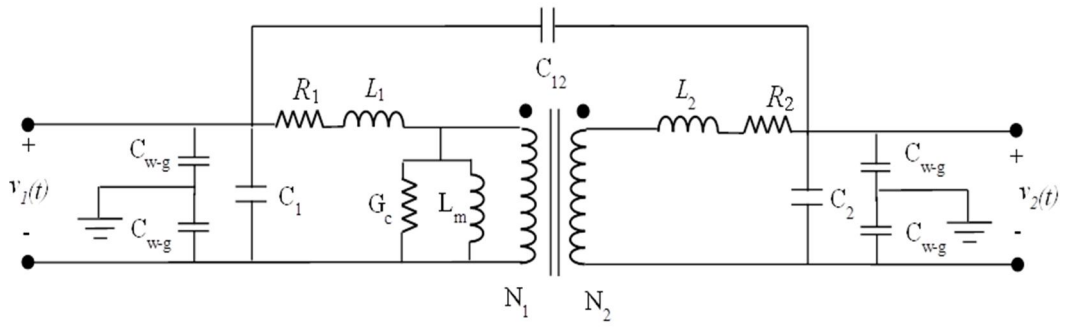

Figure 2-24: Low order high frequency model of a power transformer

2.5.2.2.2 Effect of discretization on model parameters

The way in which the winding is discretised affects the methodology in which the model parameters are evaluated. For a DPM or LPM having a fine resolution as shown in Figure 2-25, the calculated turn-to-turn capacitance C_{tt} and turn-to-ground capacitance C_{tg} can readily be implemented if each turn represents a section. However, if a group of turns or disks constitutes a single section as presented in Figure 2-25 the equivalent series-capacitance C_s and equivalent capacitance to ground C_g must be derived in some way from the initial detailed parameters.

Models used for transformer design traditionally have a resolution where a section represents at least a disk pair [24]. Thus a disk pair is represented with a single inductive branch, a series-capacitance and a capacitance to ground. An equivalent series-capacitance can be calculated by assuming a unity linear voltage drop V across the section. The stored energy W_{ij} between each conductor, i and j, in the section is calculated and converted to an equivalent series-capacitance C_s that would store the same energy using the relation [24] [27]:

$$C_s = \frac{2\sum W_{ij}}{V^2}, \qquad (2.20)$$

In practice the voltage distribution inside a section behaves similarly to the voltage distribution along the whole of the winding in that it is non-linear [39]. In some transient studies the non-linear voltage distribution inside the disks are accounted for, resulting in a more accurate representation of the equivalent capacitance [14]. The same approach can be used in reducing the number of inductive parameters. An equivalent inductive branch can be derived by preserving the flux of all the inductive elements of the original detailed sections [67].

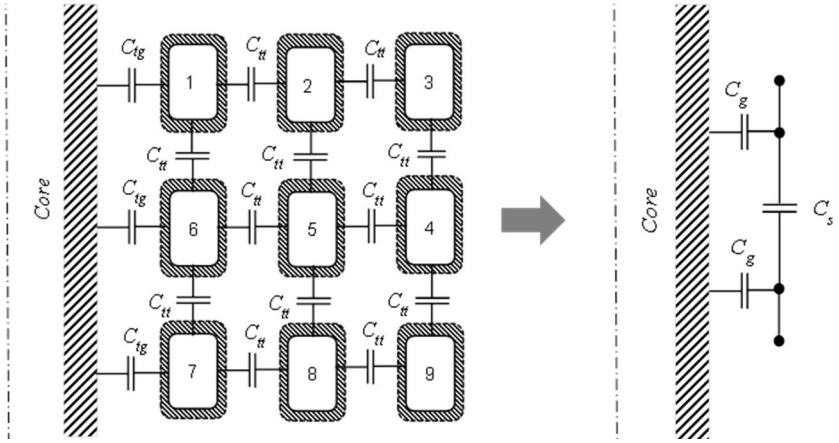

Figure 2-25: Reduction of capacitive model to a single π-network

If a single conductor is used, the method is quite simple and presented in Figure 2-26. If multiple conductors are used in parallel, the stored energy in each conductor must be calculated with respect to the current distribution in the two paths. From this energy the equivalent inductance value can be calculated. This is only valid if the conductors are properly transposed which implies that all three conductors in the section under consideration have the same inductance.

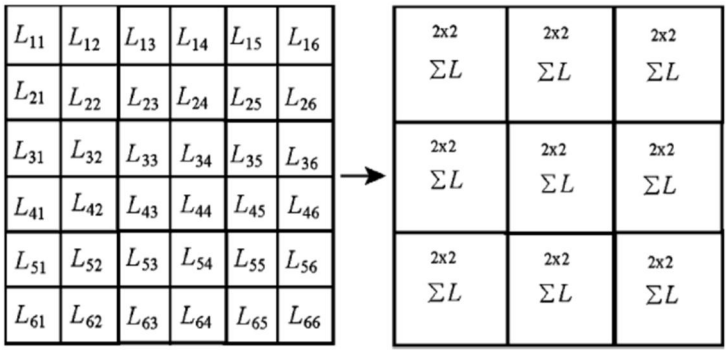

Figure 2-26: Reduction method of inductance matrix [67]

2.6 Solving electromagnetic models

2.6.1 Introduction

Due to the complexity and size of the mathematical models, initial studies evaluated the mathematical models only for a unit voltage step [17] [18] [11]. While the industrial application of mathematical models lingered due to the absence of digital computers, physical scaled models were used during the design stage of a transformer in order to determine the expected voltage oscillations, thereby insuring adequate insulation in and around the winding structure [62]. However, this meant that for each transformer design a

new scale model had to be constructed resulting in an expensive and time consuming exercise.

The feasibility of detailed mathematical models became evident with the developments in digital computing. Computational speed and memory capacity grew to an extent where mathematical modelling became an attractive alternative to scale models. The digital computer was first used for transient studies by Abetti [11]. The model consisted of an equivalent circuit representing discrete subdivisions of the transformer winding, where each division had its individual self-inductance, mutual-inductance to all other sections and capacitive coupling to adjacent sections and earth. The voltage throughout the winding was determined by solving the set of ODEs representing the LPM [13].

As mentioned in section 2.5.2.1, both the DPM and LPM can be expressed in either differential form or in integro-differential form. These mathematical representations can be expressed in various ways each lending it more or less appropriate to different solution methods. This literature survey will be limited to the two common formulations used in transient simulation studies namely the *state-space* formulation and the *nodal* formulation.

2.6.2 Common model formulations

2.6.2.1 State-space form

For both equations (2.17) and (2.18) the unknown voltages can be calculated using the state-space formulation as presented below [87]:

$$\dot{\boldsymbol{X}} = [\boldsymbol{A}]\boldsymbol{X} + \boldsymbol{B}\boldsymbol{v} \qquad (2.21)$$

and

$$\boldsymbol{y} = [\boldsymbol{F}]\boldsymbol{X} + \boldsymbol{D}\boldsymbol{v}\,, \qquad (2.22)$$

where $\dot{\boldsymbol{X}}$ denotes the column vector of the derivative of the state variables. $[\boldsymbol{A}]$ and $[\boldsymbol{F}]$ are matrices of constant coefficients and $\boldsymbol{y}$ is the column vector of the output voltages. Both the $\boldsymbol{B}$ and $\boldsymbol{D}$ column vectors contain constant coefficients. The two state variables commonly used, are the currents through the inductors and the voltages across the capacitors [25] [59] [14].

The state variables of a DPM as presented in Figure 2-20 are both time and space dependant. Neglecting the losses, the state of the system can be expressed by means of a set of PDEs [38] [18] [79] as expressed in the following relations:

$$\frac{\partial \boldsymbol{v}(x,t)}{\partial x} = [\boldsymbol{L}]\frac{\partial \boldsymbol{i}(x,t)}{\partial t} \tag{2.23}$$

and

$$\frac{\partial \boldsymbol{i}(x,t)}{\partial x} = -[\boldsymbol{C}]\frac{\partial \boldsymbol{v}(x,t)}{\partial t}. \tag{2.24}$$

This formulation is also referred to as the *Telegrapher's equations*. The voltage $\boldsymbol{v}(x,t)$ and current $\boldsymbol{i}(x,t)$ are both a function of time and position along the winding. In this format the matrix $[\boldsymbol{L}]$ represents the distributed self-inductance of each disk or turn and the mutual-inductances between them. These values are expressed in per-unit length. The matrix $[\boldsymbol{C}]$ contains the per unit length values of the capacitances between the disks or turns [24].

For LPMs, the state variables are only time dependant and can therefore be written as a set of ODEs. Unlike the $[\boldsymbol{L}]$ and $[\boldsymbol{C}]$ matrices of the DPM, the matrices of the LPM contains the lumped capacitive and inductive values of each discrete section.

2.6.2.2 Nodal form

Instead of expressing the system in state-space form, the application of substitution results in the nodal form. This formulation may take on various forms such as that used in modified nodal analysis (MNA). Generally the nodal form of a LPM, where the parameters, voltages and currents are only dependant on time, is expressed as an integro-differential equation as shown in the following relation:

$$[\boldsymbol{Y}_n]\boldsymbol{v}(t) = \boldsymbol{i}(t) \tag{2.25}$$

where

$$[\boldsymbol{Y}_n] = \left[\frac{d}{dt}[\boldsymbol{C}_n] + \int [\boldsymbol{L}_n]\, dt\right]. \tag{2.26}$$

The matrix $[\boldsymbol{Y}_n]$ is known as the nodal admittance matrix. The $[\boldsymbol{C}_n]$ and $[\boldsymbol{L}_n]$ matrices in equation (2.26) are represents the capacitances and inductance connected to each node in the model.

2.6.3 Time- and frequency-domain solution methods

The mathematical formulations can be solved in both the time- and frequency-domain. The reduced complexity of circuit analysis in the frequency-domain portrays this method as the

preferred route and has been used in various studies when main interest is the resonance behaviour of the winding [21] [88] [79] [81]. The time-domain response can be obtained by using the inverse Fourier transform. However, time dependant model parameters such as switches cannot readily be address in the frequency-domain. Another challenge is the presence of non-linear model parameters such as those representing surge arrestors.

Time-domain solvers can easily accommodate non-linear model parameters as well as switches. However the handling of frequency dependant parameters such as dielectric losses and the skin-effect mentioned in section 2.4.4 become more complicated. Estimated RC or RL branches can be used to represent these frequency dependant losses when solving the model in the time-domain [65]. Frequency-domain solvers, on the other hand, can facilitate these matters more easily [89] [82].

2.7 Signal measurement

In order to validate the response of the model it should be compared to the measured response of the physical system under consideration. The connection of the measurement equipment inherently applies an additional load to the system subjected to testing. Care should be taken to minimise the effect of the measuring equipment on the actual system response.

2.7.1 Effect of probe connections

Various types of probes are available, but due to the simplicity and economic benefits of passive RC probes this thesis will only discuss these probe types. The probe head and connecting lead has specified input impedances as presented in Figure 2-27 [90]. The capacitance to ground C_c and the shunt resistance R_p of the probe along with the inductance in the ground lead L_g of the probe should be considered during the experimental setup.

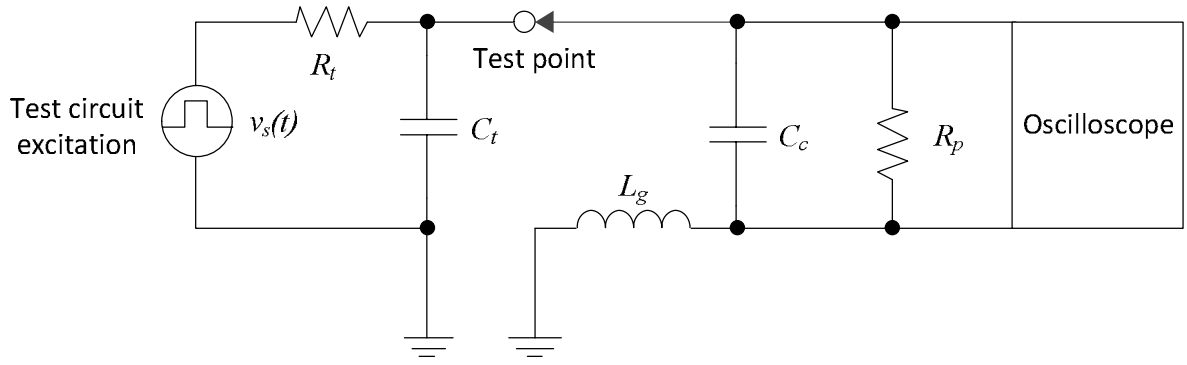

Figure 2-27: High frequency circuit of probe and test subject [90]

For accurate measurements the effect of C_c, R_p and L_g on the source having an output resistance R_t and capacitance C_t should be kept as small as possible. Selecting a probe with a very small C_c and a large R_p will accomplish this. To keep L_g as small as possible, the ground lead should be made as short as possible [90].

2.7.2 Quantization- and ambient noise

A measured signal is subjected to noise arising from ambient interference and quantization noise. Ambient noise is mostly regarded as arbitrary interferences in a signal. Noise may be caused by sources external or internal to the measurement equipment. External noise may arise from equipment producing electromagnetic discharges. Other sources of external noise are atmospheric noise caused by lightning and radiation from space caused by solar activities [91]. Internal noise on the other hand is mostly caused by temperature variations in devise components.

Unlike ambient noise, quantization noise is an inherent characteristic of every analogue to digital conversion device (ADC). It originates from the digital binary representation of an analogue signal. The number of bits used by the ADC determines the resolution of the signal amplitude [92] [93]. Signal values that do not coincide with the resolution are either truncated or rounded. This causes a step-like profile on the wave as presented Figure 2-28. These noise components need to be taken into account during measurements.

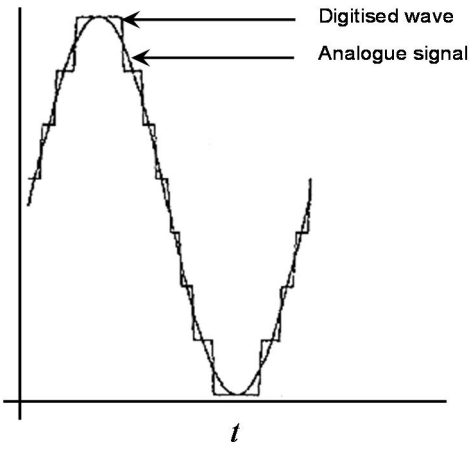

Figure 2-28: Digital quantisation of analogue signal [93]

Using an ADC with a high resolution reduces the effect of the quantisation [93]. Averaging can also be used to reduce noise on a measured signal. The total mean square error (MSE) of a sampled signal can be reduced using the average of N measurements of such that the total MSE can be expressed as [94]:

$$MSE = (\Delta t^2/12 + \varphi^2)/N \qquad (2.27)$$

where Δt is the sample interval and φ is the noise variation. Thus by taking multiple measurements of the signal of interest the error caused by quantization- and ambient noise can be reduced.

2.8 Digital signal processing considerations

2.8.1 Introduction

The response of electromagnetic model of the power transformer is evaluated in both the time and frequency-domain. Aside from proper measurement considerations such as those presented in 2.7, some fundamental signal processing matters also need to be addressed. The two topics discussed in this section are due to their importance in the context of this project.

2.8.2 Sampling frequency

The fidelity of the measured signal is strongly dependant on the sampling frequency f_s. If the sampling frequency is too low, aliasing can occur as shown in Figure 2-29 [92]. The Shannon theorem states that the sample frequency must be at least twice that of the highest frequency component of the signal [95]. This frequency is known as the *Nyquist frequency* f_n. The sampling frequency also plays an important role in the frequency-domain analysis of a sampled signal. This matter is discussed in the following section.

2.8.3 Frequency-domain signal analysis

The transformation of time-domain signals to the frequency-domain can be done either by the Fourier transform or the Laplace transform [95] [92]. The choice of transformation method depends mainly on the application. When analysing discretised time signals $\boldsymbol{x}$(n) the favourable method is the Discrete Time Fourier Transform (DTFT) [95] [92] defined as:

$$\boldsymbol{X}(\omega) = \sum_{-\infty}^{\infty} \boldsymbol{x}(n)\, e^{-j\omega n} \qquad (2.28)$$

where $\boldsymbol{X}(\omega)$ is a series of complex exponentials. The Fast Fourier Transform (FFT) is a DTFT algorithm used in various frequency estimation applications in discrete time signal processing. Application of the FFT to a discrete time signal, results in a finite series of

rotating vectors expressed as complex conjugate pairs. These conjugate pairs represent multitudes of 0,1,2, … , $n/2$ of the fundamental frequency ω_o of the signal expressed as [53]:

$$\omega_o = f_s/n \qquad (2.29)$$

It is therefore imperative that f_s is high enough to ensure that the frequency step ω_o is not too large. If ω_o is too large, frequencies of interest may be lost between consecutive multitudes of the fundamental frequency. In addition to this, n must be large enough to represent the lowest frequency of interest.

Another matter to consider is the discontinuities caused at the beginning and end of the analysed signal. The input signal is assumed to be periodical and given for a period of 2π. Non-zero values at the beginning- and end of the signal causes discontinuities as presented in Figure 2-30. These discontinuities can cause high frequency components to reflect in the frequency plot the analysed signal. This can be remedied by applying windowing functions to the signal of interest. However, if possible, non-zero values at the beginning and end of the signal should be avoided.

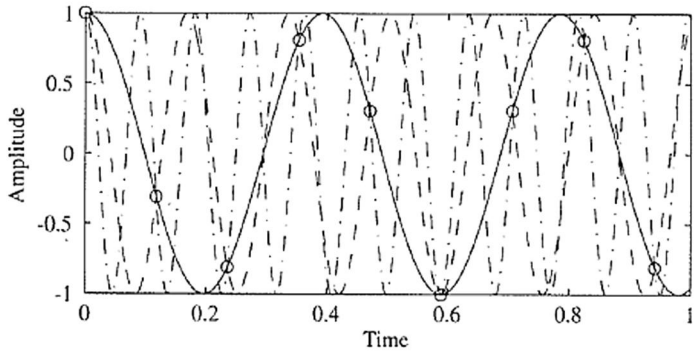

Figure 2-29: Aliasing effect of under-sampled time-domain signal [92]

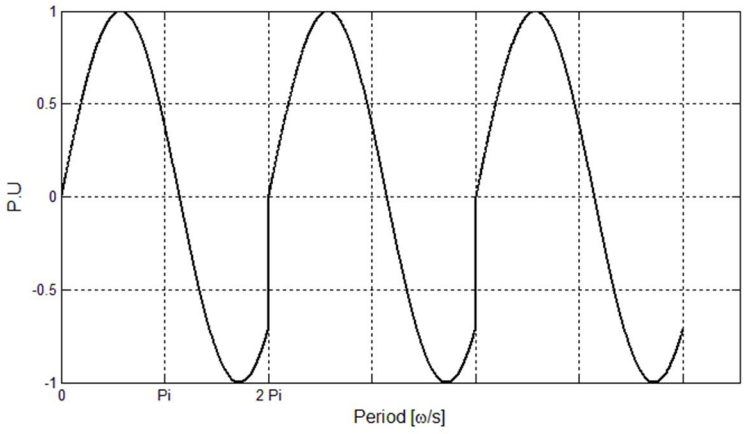

Figure 2-30: Non-zero discontinuities interpretation of FFT algorithm

Chapter 3 Modelling approach

3.1 Selection of model type

The ability to represent the LPM as a system of ODEs makes it an attractive approach due to its reduced complexity and intuitive nature. It is also easy to implement in a digital computer algorithm and can accommodate a non-uniform winding structure with ease.

As discussed in section 2.5.2.1, many transient studies have been done using the LPM and it is thus a tried-and-trusted method. Though the LPM has a smaller bandwidth than a MTL, the frequency range of interest is still relatively low enough to implement a LPM with a fair accuracy [80].

3.2 Discretisation methodology of transformer winding structure

The highest frequency that this study is concerned with is 500 kHz. The matter to consider during discretization of the actual geometry is the physical length of a discrete section as discussed in section 2.5.2.2. The wave length λ of the highest frequency f is given by the expression [47]:

$$\lambda = \frac{v}{f} \tag{3.1}$$

where v is the velocity of the traveling wave. Assuming a vacuum medium where v is 300e6 m/s the wave length would be 600 m. Refering to equation (2.19), this means that the physical length of a discrete winding element should ideally not be longer than 72 m. Power transformers have windings where the mean turn length of a winding can be up to 70 m. Thus a suitable resolution would be to divide the winding into sections where each section represents a single turn of a conductor in the winding as shown in Figure 3-1.

The core is also divided into sections as shown in Figure 3-2. For the purpose of this study the core is divided into the same number of sections as the number of sections of the inner-most winding facing the core. For simplicity sake, the yoke area above the winding is assumed to cover the entire circumference of the winding.

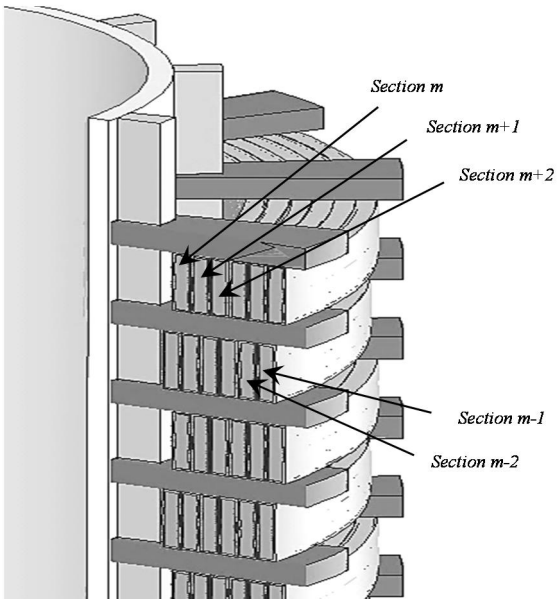

Figure 3-1: Discretisation of disk winding

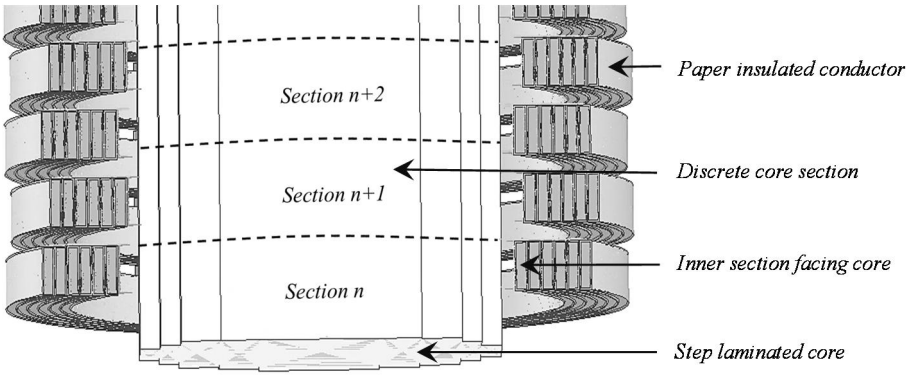

Figure 3-2: Main core limb discretisation

Each section in the transformer winding is represented with an inductive element that has its self-inductance and mutual inductive coupling with all other sections. Capacitive coupling exists between sections but is only considered when in close proximity of each other.

3.3 Inductance model development

3.3.1 Requirements and considerations

The primary requirement of the model is that it must be able to portray the inductive behaviour of the transformer winding structure during factory tests. These tests are specified in [7]. Therefore three important aspects need to be considered, namely the initial conditions of the system, the boundary conditions during these tests and the frequency range that the inductance model should be valid for.

As mentioned in Chapter 2 fast-front surges range from 10 kHz to 3 MHz. However, the frequency range concerning lightning-impulse studies is ideally 10 – 500 kHz [10].

Another matter that must be considered is that the tests specified in [7] require all non-impulsed winding terminals to be grounded. High currents are set up in the winding structure due to the short circuit state of the unexcited windings. The main flux in the core is cancelled out by the unexcited short circuited windings [60]. The penetration of the magnetic flux into the core is further hampered by eddy-currents forming on the surface due to the varying magnetic flux perpendicular to the core surface [52]. The contribution of the induced magnetic field due to the core is expected to be negligible.

With the specified application of the inductance model, the effect of the iron-core on the inductive behaviour of the transformer will be ignored. Various documented electromagnetic models of transformers for similar applications have been implemented neglecting the effect of the core for frequencies above 10 kHz with acceptable results [60] [96]. It is vital to emphasise that the power transformer is in reality not a linear device. The linear inductance model is only appropriate for the application defined in the scope of this thesis.

The self- and mutual-inductances of current-carrying conductors are calculated by approximating the conductor with a current-filament at its centre as presented in Figure 3-3. As mentioned in section 2.4.2.2, a single current-filament approximation does seem to give a reasonable result in some applications.

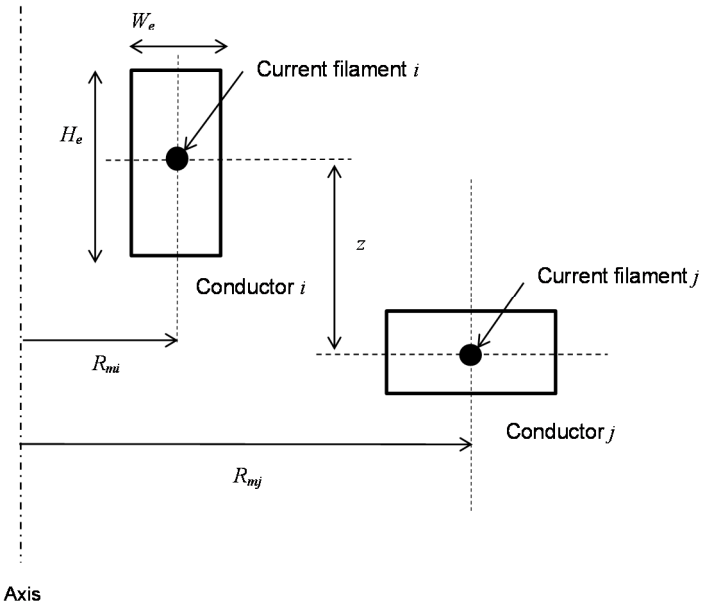

Figure 3-3: Current-filament approximation of conductors

3.3.2 Self-inductance calculations

The conductors used in power transformers are rectangular. The self-inductance L of a single turn in air where the current is uniformly distributed inside the conductor of a rectangular geometry is given by the relation [54] [56]:

$$L = 4\pi R_m \left(log\left(\frac{8R_m}{GMD}\right) - 2 \right), \tag{3.2}$$

where R_m is the mean radius of the conductor and GMD is the *geometrical-mean-distance* of the cross-section of the conductor. The GMD of a rectangular conductor can be expressed by the relation [55]

$$GMD = 0.2235(H_e + W_e), \tag{3.3}$$

where H_e and W_e are the height and the width of the conductor respectively. Equation (3.2) and (3.3) are used to calculate the self-inductance of each section excluding the sections that reside in the core, shielding-cylinder or tank.

3.3.3 Mutual-inductance calculations

The mutual-inductance M between two sections i and j is calculated by assuming that each section can be approximated by a single current-filament [56]. For two sections i and j having a mean radius R_{mi} and R_{mj} respectively, the mutual-inductance between the two current-filaments is given by the relation [97]:

$$M = 4\pi\sqrt{R_{mi}R_{mj}}\left[\left(\frac{2}{k} - k\right)K - \frac{2}{k}E\right], \tag{3.4}$$

where

$$k^2 = \frac{4\left(R_{mi}R_{mj}\right)}{\left(\left(R_{mi+}R_{mj}\right)^2 + z^2\right)} \tag{3.5}$$

and z is the vertical distance between the current-filaments. K and E are the complete elliptic integrals of the first and second kind of the modules k.

3.3.4 Compensation for cross-overs in disk windings

The equations in the preceding sections assume each section to revolve a full 360^o at a constant radius. In practice, the winding conductors do not follow this exact behaviour which

will cause deviations in calculated and measured results. A particular consideration regarding this very matter is the reduction of effective electrical turns due to staggered cross-overs as discussed in 2.2.4.2.

To account for the lost portion of the electrical turn due to the staggered cross-overs, equation (3.2) and (3.4) are corrected with the factor F_{lost} resulting in the actual per unit electrical turn. F_{lost} represents the fraction of an electrical turn pertaining to a mechanical turn. Thus for a winding having N_{mech} mechanical turns and N_{lost} number of turns are lost, F_{lost} is calculated with the following relation:

$$F_{lost} = 1 - \frac{N_{lost}}{N_{mech}}. \tag{3.6}$$

The self- and mutual-inductance are then calculated using relation (3.7) and (3.8) respectively.

$$L = 4\pi R_m \left(log\left(\frac{8R_m}{GMD}\right) - 2 \right) \cdot (F_{lost}) \tag{3.7}$$

$$M = 4\pi \sqrt{R_{mi} R_{mj}} \left[\left(\frac{2}{k} - k\right) K - \frac{2}{k} E \right] \cdot (F_{lost}) \tag{3.8}$$

3.3.5 Structure of the inductance matrix

3.3.5.1 Branch-inductance matrix

The calculated self- and mutual-inductances are captured in a $(m \times m)$ branch-inductance matrix $[\boldsymbol{L}_b]$ where m represents the total number of sections in the winding structures. These are the sections in the discretised transformer geometry that will carry currents. Thus sections belonging to the tank and core are not considered. The off-diagonal elements, $L_{b_{ij}}$, represent all the mutual-inductances and the diagonal elements, $L_{b_{ii}}$,represent the self-inductance of the respective section.

A branch representation is useful when calculating currents, but a nodal representation of the inductances is desired since the nodal voltages are calculated at different nodes. Therefore the branch-inductance matrix must be transformed into a nodal-inductance matrix. This is done via a transformation formula of impedance [98]:

$$[\boldsymbol{L}_n] = [\boldsymbol{T}'][\boldsymbol{L}_b][\boldsymbol{T}], \tag{3.9}$$

where $[\boldsymbol{T}]$ is the adjacency matrix described in the next section and $[\boldsymbol{T}]'$ is the transpose of $[\boldsymbol{T}]$.

3.3.5.2 *Adjacency matrix definition*

The adjacency matrix $[\boldsymbol{T}]$ reflects the relationship of the inductive branches (sections) with the system's nodes. $[\boldsymbol{T}]$ is expressed as an $(n \times m)$ matrix where m represents all the inductive branches and n represents the total number of system nodes. The matrix values are either '0', '1' or '-1' and are dependent on the direction of the current flow in the branch. The convention used in this thesis regards the current flow out of a node as *positive*. The construction of the adjacency matrix will be explained with reference to the network presented in Figure 3-4. The network consists of 5 inductive branches and 8 nodes.

The current flow is indicated by the arrows and the polarity of each inductor is shown by dot notation. The adjacency matrix of the system is built by evaluating each branch. A branch resides between two nodes and the current enters one node and exits the other. Depending on the polarity of the branch, the current may either flow in a positive or negative direction.

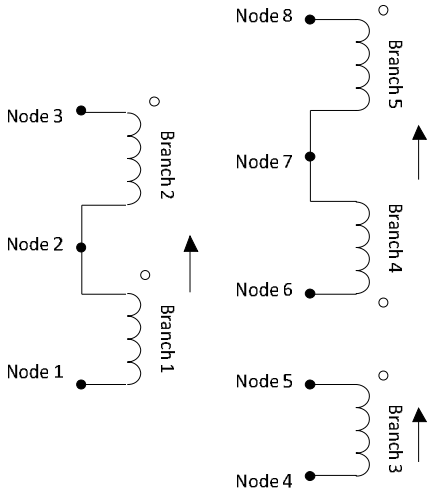

Figure 3-4: Network with node and branch allocations

With reference to Figure 3-4 branch 1 is located between node 1 and 2. Current exits node 1 and enters node 2. This is indicated on the adjacency matrix where row 1 represents branch 1, column 1 represents node 1 and column 2 represents node 2. Current exits node 1 and is therefore designated a '1'. Current enters node 2 and is therefore designated a '-1'. This convention is followed throughout the complete system until the adjacency matrix is completely populated. Relation (3.10) presents the transposed adjacency matrix.

$$[\boldsymbol{T}]' = \begin{bmatrix} 1 & -1 & 0 & 0 & 0 & 0 & 0 & 0 \\ 0 & 1 & -1 & 0 & 0 & 0 & 0 & 0 \\ 0 & 0 & 0 & 1 & -1 & 0 & 0 & 0 \\ 0 & 0 & 0 & 0 & 0 & 1 & -1 & 0 \\ 0 & 0 & 0 & 0 & 0 & 0 & 1 & -1 \end{bmatrix} \qquad (3.10)$$

3.3.6 Calculation of winding inductance with parallel conductors

The total self-inductance L_{Total} of a winding wound with one conductor having m branches, can be calculated as illustrated in Figure 2-26 using the following relation [56] [99] [67]:

$$L_{Total} = \sum_{i=1}^{m} \sum_{j=1}^{m} L_{ii} + L_{ij}, \qquad (3.11)$$

where $\boldsymbol{L}_{ij}$ is the inductance between section i and j.

However, the test-unit under consideration has two conductors in parallel. The inductances values calculated using (3.7) and (3.8) are based only on the geometrical properties of the sections. In order to calculate the total inductance of a winding having two conductors in parallel, the law of energy conservation can be implemented.

Assuming that the conductors are perfectly transposed as mentioned in 2.5.2.2.2, the total winding current I divides equally in two branch currents namely i_1 and i_2 as presented in the following expression:

$$I = (i_1 + i_2) \qquad (3.12)$$

where i_1 and i_2 are the currents flowing in conductor 1 and conductor 2 respectively. Both i_1 and i_2 are equal in magnitude and flows in the same direction. The total energy W_{Total} stored in the winding can be expressed as the sum of the energy stored in and between the inductive branches as expressed in the following relation:

$$W_{Total} = \frac{1}{2} L_1 {i_1}^2 + \frac{1}{2} L_2 {i_2}^2 + \frac{1}{2} L_{12} {i_1}^2 + \frac{1}{2} L_{21} {i_2}^2 . \qquad (3.13)$$

L_1 and L_2 are the respective total self-inductance of each conductor throughout the whole winding according to relation (3.11), while L_{12} and L_{21} are the mutual-inductances between them. Having unity current and assuming equal current distribution, the total winding inductance L_{total} can be calculated using the following equation:

$$L_{total} = \frac{1}{4}(L_1 + L_2 + 2L_{12}) \qquad (3.14)$$

3.3.7 Validation of inductance calculations using FEM

3.3.7.1 Description of geometry used in FEM modelling for validation

To validate the analytical equations the geometry of the test-unit presented in section 5.1 was drawn in Ansoft Maxwell® Version 15.0.0 as an axisymmetric 2D geometry shown in

Figure 3-5. Each section residing in the core is presented with a rectangle of vacuum material type. Each turn of every conductor in the winding is represented with a rectangle of copper material. The model was simplified by omitting the edge radii of the conductors. The paper and enamel covering of the conductors were also omitted since these do not have an effect on the magnetic field distribution. The μ_r of the conductors and the surrounding medium was set to 1 since no magnetic core is present. A unity current excitation is applied to all sections in the winding. Two additional dummy regions were created around the winding geometry for refined mesh operations.

3.3.7.2 FEM simulation considerations

Due to the pitfall briefly mentioned in 2.4.2.4 regarding FEM simulations, a boundary and mesh sensitivity analysis was done to ensure the reliability of the problem definition. The change in the self-inductance of the bottom disk and mutual-inductances of the top and bottom disk was evaluated to determine the severity of the changes in boundary and mesh definitions. For both analyses the current was assumed to be unity in all conductors.

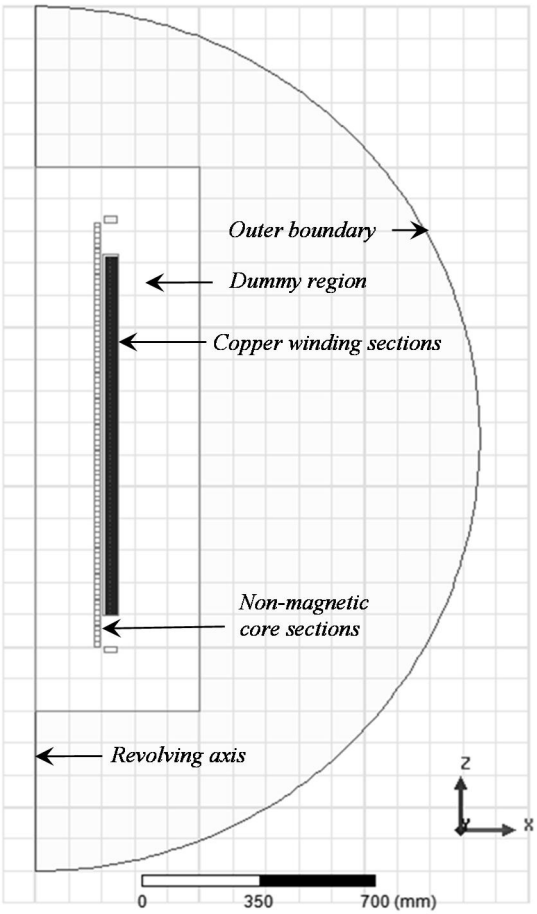

Figure 3-5: 2D FEM Geometry of test-unit

3.3.7.2.1 Effect of boundary definition and sensitivity

For magnetostatic FEM simulations the boundary conditions are usually defined by the behaviour of the vector potential $\overline{A}$ at the boundaries. The magnetic flux is either specified as tangential or perpendicular to the boundaries of the problem. With some experience this type of boundary condition can be used with a fair amount of accuracy.

Some FEM solution methods facilitate a boundary condition that does not force the vector potential to be tangential or perpendicular. Instead it allows a certain degree of freedom by assuming an extrapolation of the magnetic flux curvature before intercepting with the boundary. In Ansoft Maxwell® this method is referred to as a *balloon-type* boundary.

For the boundary sensitivity analysis the magnetic field strength $\overline{H}$ at the revolving axis was assumed to only have a z component by setting the boundary type to *symmetric*. The balloon- and vector potential type boundaries were compared for three cases. The boundary was moved closer to the winding geometry by reducing the radius of the outer boundary. The radius of the outer boundary for case 1, 2 and 3 was set to 3000 mm, 1850 mm and 1350 mm respectively. The change in the self-inductance of the bottom disk was evaluated as shown in Figure 3-6. The mutual-inductance between the top and bottom disk was also evaluated and is presented in Figure 3-7.

From these two graphs it is evident that the model having a balloon-type boundary is the least sensitive to the distance of the boundary from the area of interest. Both the self- and mutual-inductance remains fairly constant in value regardless of the distance to the boundary. The model having a vector potential type boundary on the other hand is clearly influenced by the distance of the boundary. However, the change in values in this example is not more than 1%. Thus with good judgement, both boundary types can be used depending on the desired accuracy.

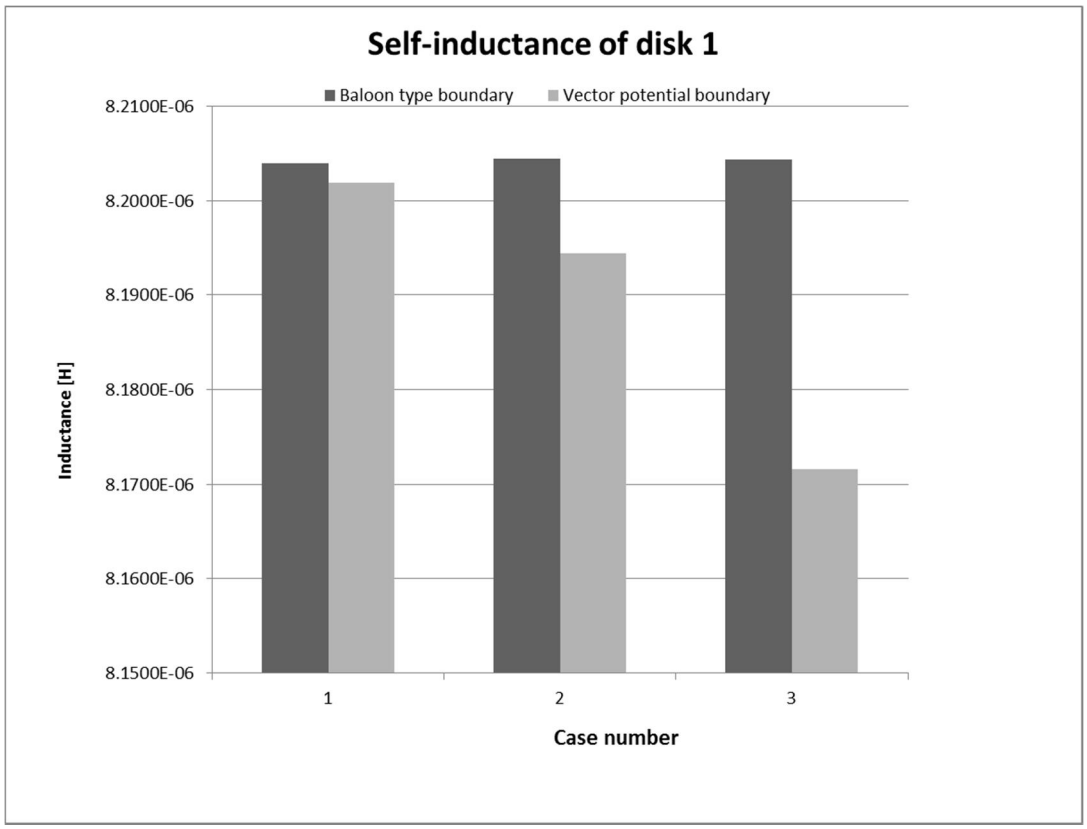

Figure 3-6: Boundary sensitivity of self-inductances

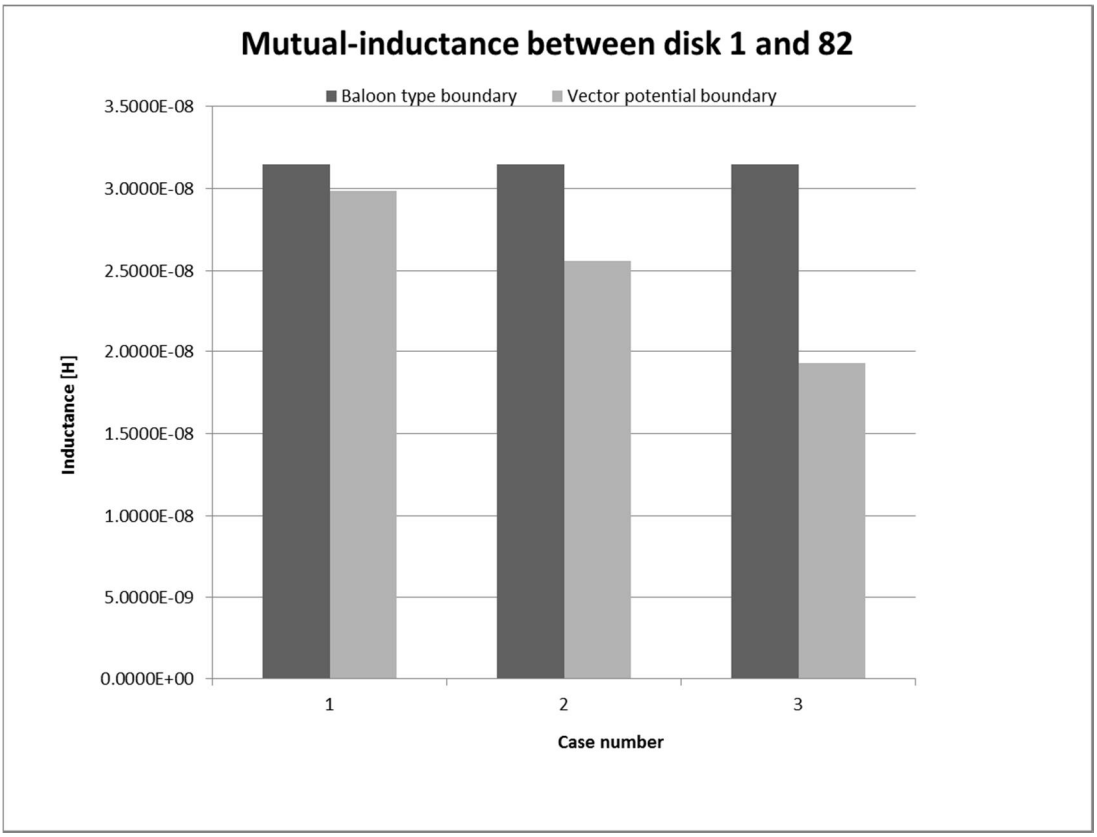

Figure 3-7: Boundary sensitivity of mutual-inductances

3.3.7.2.2 Effect of mesh resolution and sensitivity

The mesh sensitivity analysis was done by refining the mesh of the inner and outer dummy region as presented in Figure 3-8 using a balloon type boundary. Using the same validation criteria as used in the boundary sensitivity analysis, the self- and mutual-inductances of the top and bottom disk were compared and presented in Figure 3-9 and Figure 3-10. The distribution of the number of elements in the 2D geometry is shown in Figure 3-11.

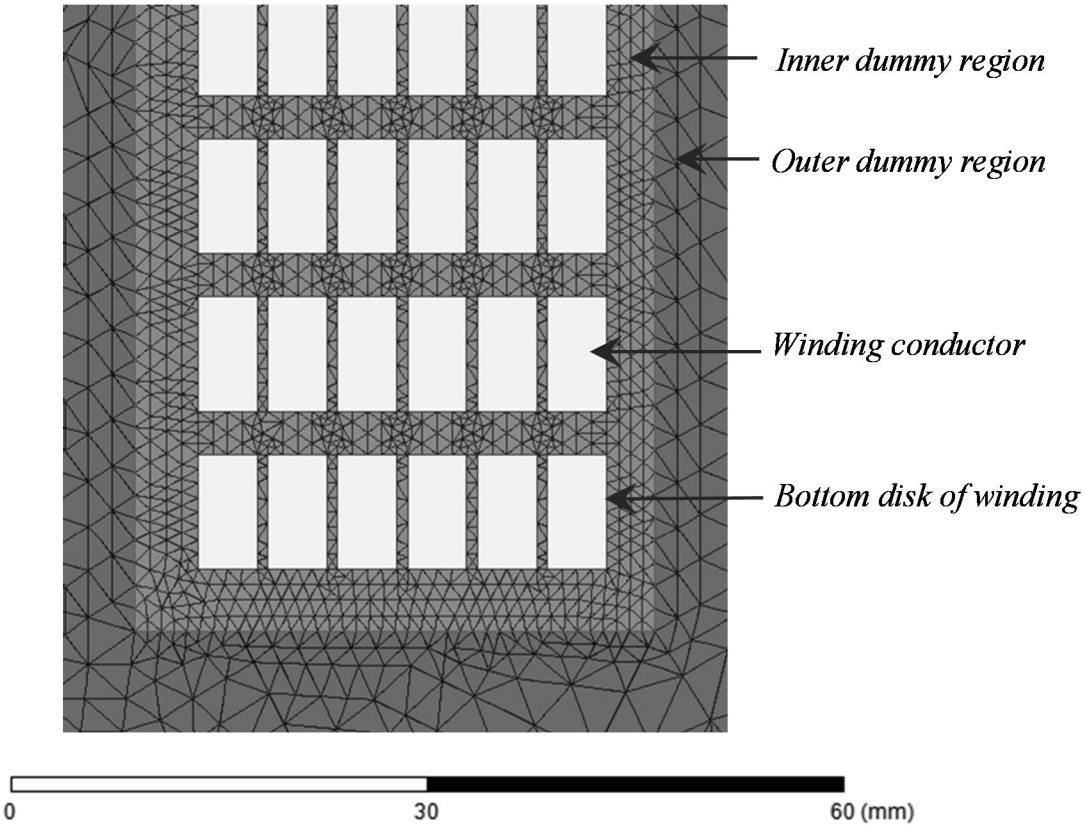

Figure 3-8: Mesh detail used in sensitivity study

It is clear that the changes in inductance values for different number of elements ranging from 9053 to 280702 are nearly negligible. Thus to avoid unnecessary computational overhead, the simulation can be done with 9053 elements with a fair accuracy.

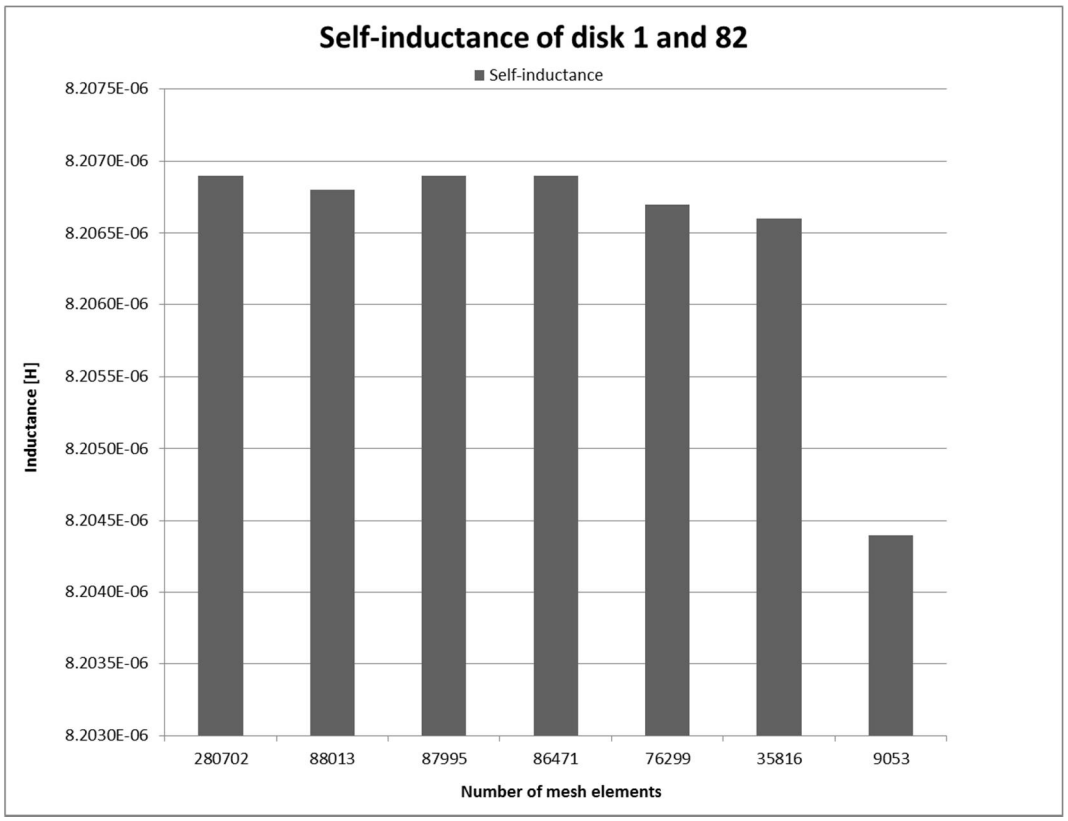

Figure 3-9: Change in self-inductance due to total number of mesh elements

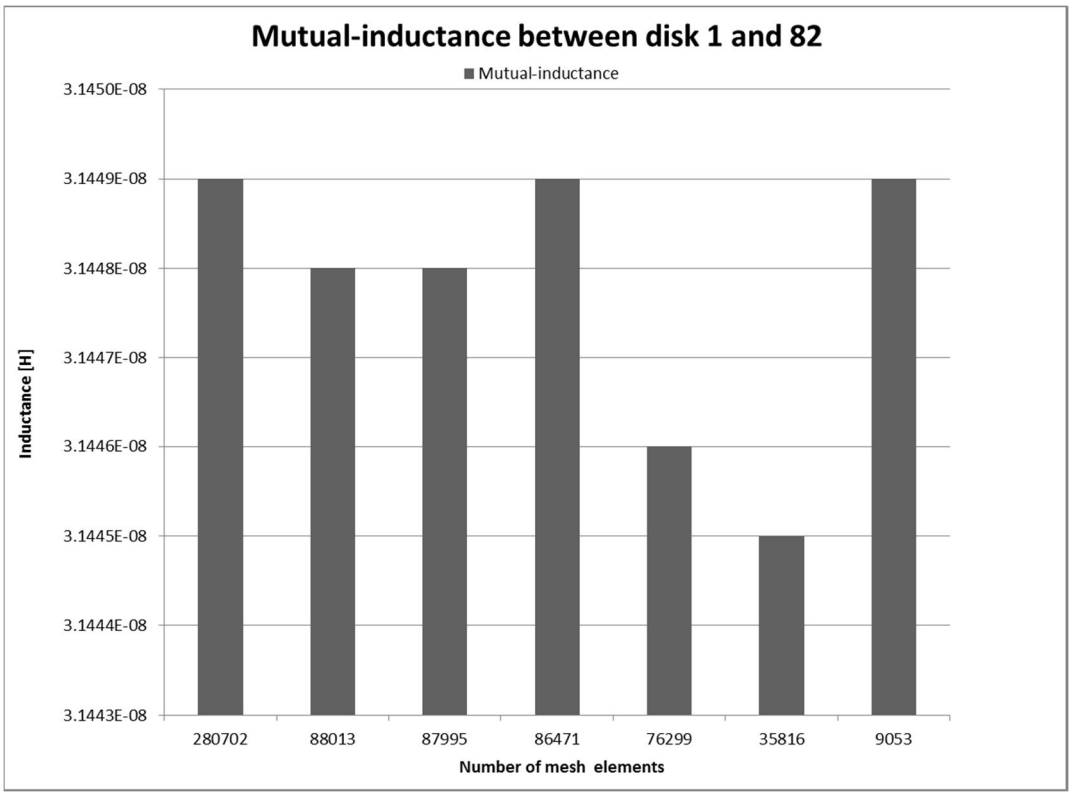

Figure 3-10: Change in mutual-inductance due to total number of mesh elements

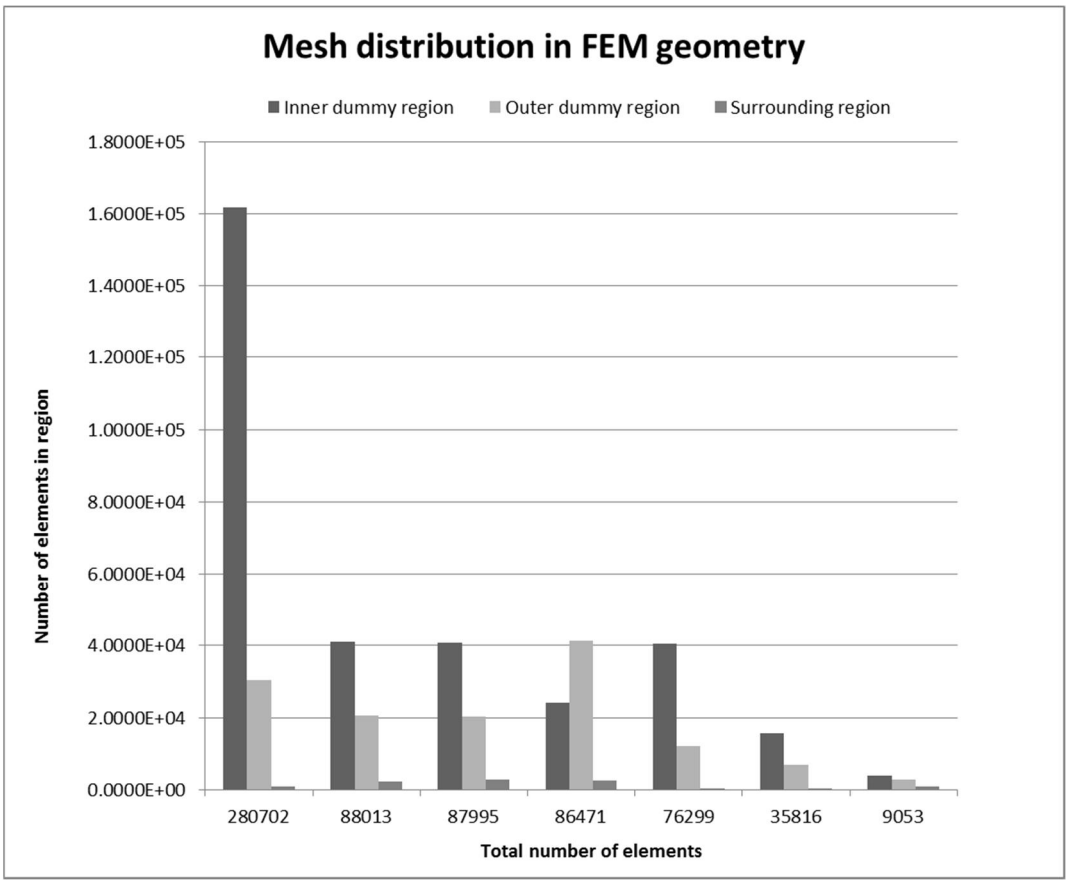

Figure 3-11: Number of elements in dummy regions used in mesh sensitivity analysis

3.3.7.2.3 Pre- and post-processing in Ansoft Maxwell®

In the initial setup as described in section 3.3.7.1, the effect of the cross-overs is not taken into account since the geometry is defined as axisymmetric. All turns are assumed to be complete. Another matter that is not reflected in the input is the fact that the winding sections belong to either one of two parallel conductors. Unity current is used during the calculation and generation of the inductance matrix as mentioned in 2.4.2.4. It is therefore not readably possible to compare a detailed inductance matrix calculated by means of equation (3.7) and (3.8) to that obtained using Ansoft Maxwell®.

The post-processing capability of Ansoft Maxwell® allows the grouping of sections where the number of electrical turns per section can be specified as well as the number of parallel paths in the grouped sections. The total winding inductance can be calculated by grouping all sections representing the winding conductors into one group with two parallel paths. The number of electrical turns of each section can now be assigned the calculated value F_{lost} as calculated according to (3.6).

In conclusion, the detailed pre-processed inductance matrix generated in Ansoft Maxwell® can be used to validate equation (3.2) and (3.4). Using the post-processing functionality of Ansoft Maxwell®, the suitability of equations (3.7) and (3.8) can be indirectly validated in terms of the complete winding inductance.

3.3.7.3 Detailed inductance matrix validation

The calculated and simulated self- and mutual-inductance values of the sections in the bottom disk of the test-unit are presented in

Table 3-1 and Table 3-2. All turns are assumed to be complete with unity current excitation. The percentage deviation is shown in Table 3-3. The maximum deviation of 3.6% in calculated and simulated results is the mutual-inductance between section 84 and 85.

Table 3-1: Inductance matrix of disk 1 (Ansoft Maxwell®)

Section	84	85	86	87	88	89
84	1.13E-06	9.58E-07	8.09E-07	7.17E-07	6.52E-07	6.02E-07
85	9.58E-07	1.17E-06	9.92E-07	8.39E-07	7.44E-07	6.77E-07
86	8.09E-07	9.92E-07	1.21E-06	1.03E-06	8.70E-07	7.72E-07
87	7.17E-07	8.39E-07	1.03E-06	1.25E-06	1.06E-06	9.00E-07
88	6.52E-07	7.44E-07	8.70E-07	1.06E-06	1.29E-06	1.10E-06
89	6.02E-07	6.77E-07	7.72E-07	9.00E-07	1.10E-06	1.33E-06

Table 3-2: Calculated inductance matrix of disk 1 - Eq. (3.2) and (3.4)

Section	84	85	86	87	88	89
84	1.13E-06	9.93E-07	8.20E-07	7.22E-07	6.55E-07	6.04E-07
85	9.93E-07	1.17E-06	1.03E-06	8.50E-07	7.49E-07	6.80E-07
86	8.20E-07	1.03E-06	1.21E-06	1.06E-06	8.81E-07	7.77E-07
87	7.22E-07	8.50E-07	1.06E-06	1.25E-06	1.10E-06	9.11E-07
88	6.55E-07	7.49E-07	8.81E-07	1.10E-06	1.29E-06	1.14E-06
89	6.04E-07	6.80E-07	7.77E-07	9.11E-07	1.14E-06	1.33E-06

Table 3-3: Deviation of calculated and simulated inductance values for disk 1 - Eq. (3.2) and (3.4)

Section	84	85	86	87	88	89
84	0.00%	3.59%	1.35%	0.69%	0.46%	0.33%
85	3.59%	0.00%	3.76%	1.30%	0.67%	0.44%
86	1.35%	3.76%	0.00%	2.87%	1.26%	0.65%
87	0.69%	1.30%	2.87%	0.00%	3.70%	1.21%
88	0.46%	0.67%	1.26%	3.70%	0.00%	3.57%
89	0.33%	0.44%	0.65%	1.21%	3.57%	0.00%

The mutual-inductance values of the sections in the bottom disk to those in the top disk are presented in Table 3-4 and Table 3-5. A unity current was assumed in each section and turns were assumed to be complete. The percentage deviation is shown in Table 3-6. The maximum deviation of 0.35% in calculated- and simulated results, is the mutual-inductance between section 84 and 570.

Table 3-4: Mutual-inductance matrix of disk 1 and 82 (Ansoft Maxwell®)

Section	570	571	572	573	574	575
84	2.69E-09	2.83E-09	2.98E-09	3.14E-09	3.29E-09	3.45E-09
85	2.83E-09	2.99E-09	3.15E-09	3.31E-09	3.47E-09	3.64E-09
86	2.98E-09	3.15E-09	3.31E-09	3.48E-09	3.66E-09	3.83E-09
87	3.14E-09	3.31E-09	3.48E-09	3.66E-09	3.84E-09	4.03E-09
88	3.29E-09	3.47E-09	3.66E-09	3.84E-09	4.03E-09	4.23E-09
89	3.45E-09	3.64E-09	3.83E-09	4.03E-09	4.23E-09	4.43E-09

Table 3-5: Calculated mutual-inductance matrix of disk 1 and 82 - Eq. (3.2) and (3.4)

Section	570	571	572	573	574	575
84	2.69E-09	2.84E-09	2.98E-09	3.14E-09	3.29E-09	3.45E-09
85	2.84E-09	2.99E-09	3.15E-09	3.31E-09	3.47E-09	3.64E-09
86	2.98E-09	3.15E-09	3.31E-09	3.48E-09	3.66E-09	3.83E-09
87	3.14E-09	3.31E-09	3.48E-09	3.66E-09	3.84E-09	4.03E-09
88	3.29E-09	3.47E-09	3.66E-09	3.84E-09	4.04E-09	4.23E-09
89	3.45E-09	3.64E-09	3.83E-09	4.03E-09	4.23E-09	4.44E-09

Table 3-6: Deviation between calculated and simulated mutual-inductances - Eq. (3.2) and (3.4)

Section	570	571	572	573	574	575
84	0.00%	0.35%	0.00%	0.00%	0.00%	0.00%
85	0.35%	0.00%	0.00%	0.00%	0.00%	0.00%
86	0.00%	0.00%	0.00%	0.00%	0.00%	0.00%
87	0.00%	0.00%	0.00%	0.00%	0.00%	0.00%
88	0.00%	0.00%	0.00%	0.00%	0.25%	0.00%
89	0.00%	0.00%	0.00%	0.00%	0.00%	0.23%

The results shown above have neglected the effect of the cross-overs. From the calculated and simulated results it is clear that the closed-form equation (3.2) and (3.4) gives reasonably accurate results when compared the results obtained by Ansoft Maxwell®.

3.3.7.4 Total winding inductance validation

Using the equation (2.2) and the data presented in Table 5-1, the total number of turns lost in the winding due to cross-overs are 13.5 turns. The winding has three mechanical turns per disk and 82 disks. Thus, there are 246 mechanical turns in the winding. Using equation (3.6) each mechanical turn represents 0.945 $p.u$ electrical turns. If equation (3.7) and (3.8) are used to calculate each section's self- and mutual-inductance respectively, the total winding inductance according to relation (3.14) is 7,9 mH. The winding inductance was measured with an RLC bridge at 1 kHz. Table 3-7 shows the calculated and measured inductance values.

Table 3-7: Total winding inductance of test-unit

Method	***Inductance value (mH)***
Calculated using equation (3.6), (3.7), (3.8) and (3.14)	7,95
Ansoft Maxwell® as described in section 3.3.7.2.3	7.89
Measured	7.9

3.4 Capacitance model development

3.4.1 Calculating capacitances inside and outside of windings

The accurate calculation of the capacitive coupling between the various sections in the winding structure is a complex exercise. In practice there exists capacitive coupling between all sections in the geometry. Calculating the capacitance between non-adjacent sections becomes a less trivial exercise since the arrangement and permittivities of the separating materials should be considered.

This study will simplify the capacitance model by only considering the charge stored between the overlapping surfaces between two sections. The fringing-effect is ignored as done by M. Loose [59]. The capacitance between radially adjacent sections i and j as presented Figure 3-12 is calculated using the parallel plate capacitor. By using the parallel plate equation, the capacitance between the two conductors separated by a distance d and having an overlapping height h, can be calculated using the following expression [25]:

$$C = \varepsilon_0 \varepsilon_r 2\pi r_{av} \left(\frac{h}{d}\right) \tag{3.15}$$

where r_{av} is the mean radius between the adjacent conductors as presented in Figure 3-12. ε_0 is the permittivity of free space ($8.854 \cdot 10^{-12}$) and ε_r is the relative permittivity of the material occupying the region between the two conductors. The same approach is used for sections that are axially adjacent. Only the overlapping width in the radial direction is considered.

3.4.2 Equivalent permittivities of composite insulation structures

The relative permittivity of the insulation material ε_r between the two sections separated by a composite insulation material, can be approximated by representing the insulation structure as a per unit volume with a per unit voltage drop across it [86]. Figure 3-13 depicts the per unit volume representation of the insulation structure typically found between disks as shown Figure 2-6.

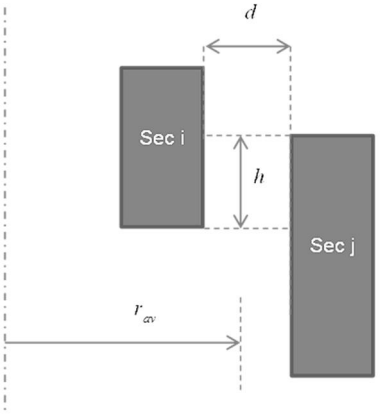

Figure 3-12: Coaxial radially adjacent sections

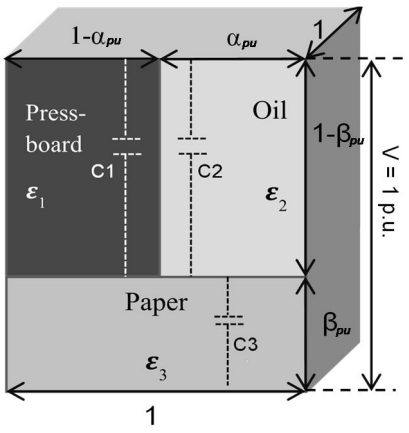

Figure 3-13: Insulation configuration for adjacent sections

The percentage of oil occupying the circumferential region between two disks is represented by α shown in the following relation:

$$\alpha_{pu} = \frac{1 - W_{sp}N_{sp}}{\pi(R_{mw})^2}, \tag{3.16}$$

where W_{sp} is the width of each spacer, N_{sp} is the number of spacers around the circumference and R_{mw} is the mean radius of the winding. β_{pu} represents the percentage of paper residing in the space between the two disks and is calculated as follows:

$$\beta_{pu} = \frac{t_{pap}}{d} \tag{3.17}$$

where t_{pap} represents the total paper thickness in region between the two disks. The distance between copper surfaces of the conductors in the disks is denoted by d.

The equivalent relative permittivity of the insulation structure between disks in a winding, is derived by calculating the total equivalent capacitance from the fictitious lumped capacitances C_1, C_2, and C_3 as presented in Figure 3-13 using the equations (3.18), (3.19) and (3.20) respectively [86].

$$C_1 = \frac{\varepsilon_1(1 - \alpha_{pu})}{(1 - \beta_{pu})} \tag{3.18}$$

$$C_2 = \frac{\varepsilon_2(\alpha_{pu})}{(1 - \beta_{pu})} \tag{3.19}$$

$$C_3 = \frac{\varepsilon_3}{(\beta_{pu})} \tag{3.20}$$

The total per unit capacitance C_{total} in the insulation structure (assuming that there is a unity voltage drop across the insulation structure) is then expressed by the following relation:

$$C_{total} = \left[\frac{1}{C_{1+}C_2} + \frac{1}{C_3}\right]. \tag{3.21}$$

Substituting equation and (3.18), (3.19) and (3.20) into equation (3.21) yields the relation:

$$C_{total} = \varepsilon_{equ} = \left[\frac{(1-\beta_{pu})}{\varepsilon_2(\alpha_{pu}) + \varepsilon_1(1-\alpha_{pu})} + \frac{\beta_{pu}}{\varepsilon_3}\right]^{-1} \quad (3.22)$$

The fixed dielectric constants used for the insulation material are those determined at a 50 Hz field excitation at 90 ^oC. However, the deviation in relative permittivity ranging from 50 - 600 Hz the as presented in Figure 2-15 is practically negligible. The relative permittivities used in this study are shown in Table 3-8 [72].

Table 3-8: Dielectric constants (50 Hz)

Material	***Relative permittivity (*** *90^oC* ***)***
Transformer oil	2.2
Craft paper (dry, 0.7 g/cm^3)	1.8
Press board (dry, 1.15 g/cm^3)	2.6
Craft paper (oil impregnated, 0.7 g/cm^3)	3.5
Press board (oil impregnated, 1.15 g/cm^3)	4.5

3.4.3 Capacitance matrix

After each section-to-section capacitance has been calculated, the calculated value is halved and assigned to the top and bottom node of the respective sections [59]. In this manner, the nodal capacitance matrix $[\boldsymbol{C}_n]$ is constructed. For example assume the top and bottom node of section 103 is node 105 and 106 respectively and section 107 has node 111 and 108 at the top and bottom respectively as presented in Figure 3-14. The calculated capacitance between section 103 and 107 is then distributed as presented in Figure 3-15. If there are multiple capacitance assignments between node 106 and 111, the equivalent capacitance between node 106 and node 111 is the sum total as presented in and Figure 3-16.

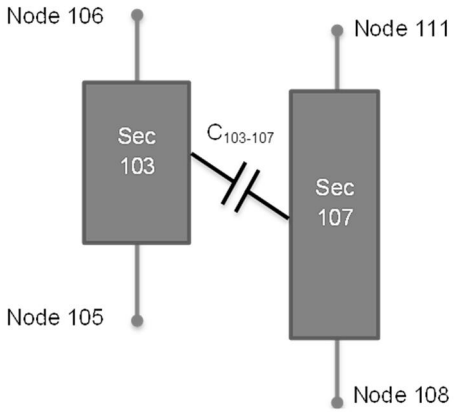

Figure 3-14: Capacitance between sections

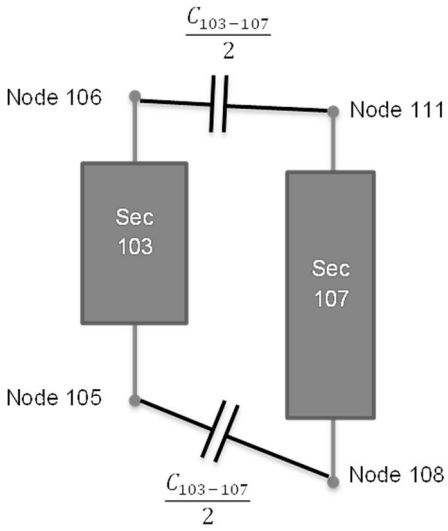

Figure 3-15: Redistribution of section capacitances

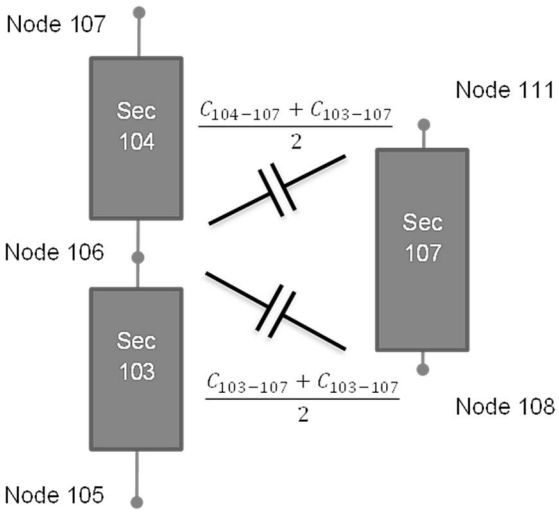

Figure 3-16: Redistribution of multiple nodal capacitances

The capacitance matrix is a *(n x n)* matrix, where n is the total number of nodes in the system. The diagonal matrix entries represent the sum of the capacitances connected to the respective node. The off-diagonal matrix values represent the capacitance connected between the two respective nodes and are negative values as seen in relation (3.23).

$$\boldsymbol{C_n} = \begin{bmatrix} C_{12} & -C_{12} & 0 & \cdots & 0 \\ -C_{12} & (C_{12}+C_{23}) & -C_{23} & \ddots & \vdots \\ 0 & -C_{23} & \ddots & \ddots & 0 \\ \vdots & \ddots & \ddots & \ddots & -C_{(n-1)n} \\ 0 & \cdots & 0 & -C_{(n-1)n} & C_{(n-1)n} \end{bmatrix} \quad (3.23)$$

3.4.4 Capacitance model validation

3.4.4.1 Considerations for validation methods

The two major contributors to the accuracy of the calculated capacitance values is the effect of fringing and the accuracy of the calculated equivalent permittivity of the complex insulation structures. The challenge is to differentiate which one is causing the discrepancy between calculated and measured values.

To ascertain the degree of influence the fringing has in the system, all insulation material can be omitted in a FEM simulation and compared to the calculated capacitance values. Any deviation can only be caused by fringing since all materials have a permittivity of 1. The analytically based capacitance model can then be altered until the deviation is acceptable. If the calculated and FEM-simulated capacitance values agree well without the presence of insulation, the effect of fringing can be ruled out.

The validation of the calculated equivalent permittivities of complex insulation structures would require actual capacitance measurements. However, the only capacitance that can effectively be measured is C_g. This would indicate if the calculated equivalent permittivies of the insulation structure to ground is correct or not. The remaining challenge is to validate C_s since this is more an abstract parameter. This can be addressed by comparing the measured initial voltage distribution to the calculated response. By means of relation (2.9) the accuracy of the series-capacitance can be evaluated which would indirectly reflect the accuracy of the calculated equivalent permittivies inside the winding.

Stray-capacitances are also a matter that needs to be considered when doing measurements. Abetti did extensive measurements on a test winding that has been a benchmark in various studies [100] [20] [19]. The coil was mainly used to investigate the

effect of a magnetic core on the inductance of the winding. The test winding had a very important feature regarding its capacitive behaviour. The winding was enclosed by an electrostatic shielding-cylinder. This confined the stray-capacitance from the outside of the winding to ground to a known region. The test-unit presented in section 5.1 does not have an outer shielding-cylinder and may therefore have a larger capacitive coupling to ground than the transformer model.

In light of the above mentioned considerations, the development of the capacitance model is more challenging than the inductance model since the inductance model does not need to take into account the presence of nearby magnetic material. This reduces the elements of uncertainties and deviation may enlarge be attributed to a geometrical nature. This is not the case with the capacitance model since the insulation material properties has a significant effect on the capacitances. There are thus more uncertainties with capacitance calculations. The development of the capacitance model is a fine balancing act which requires insight in the capacitive behaviour of the winding as presented in 2.4.3.

3.4.4.2 FEM simulation configuration

To evaluate the discrepancies caused by the omittance of the fringing-effect in the capacitance calculations, the permittivity of all the materials was set to one. Thus the suitability of equation (3.15) can be validated by means for FEM only in a uniform permittivity structure. The validation of the capacitance model was done in a similar manner as that used for the validation of the inductance model. The electrostatic solver of Ansoft Maxwell ® Version 15.0.0 was used to obtain partial capacitance matrices of the geometry of the test-unit as presented in Figure 3-5.

In order to determine the capacitive coupling between the sections, Ansoft Maxwell ® calculates the stored energy between each section by recursively applying a per unit voltage on each section while the other sections are kept at zero volts. The equivalent capacitances between two sections are calculated using the relation in (2.20).

The results were obtained after a boundary- and mesh sensitivity analysis was done similarly to that of the inductance simulation. The outer boundary was set to a balloon type boundary and the revolving axis was set to a symmetric boundary. The calculated and simulated capacitances in disk 40 are compared in Table 3-9 and Table 3-10. The methodology described in 3.4.1 ignores capacitive coupling between non-overlapping surfaces. These sections are assumed to have zero capacitive coupling as shown in Table 3-10. The presented Table 3-12 and Table 3-13 compare the capacitance of the sections in disk 40 to the sections in disk 41.

Table 3-9: Capacitance matrix of disk 40 using FEM (pF)

Section	318	319	320	321	322	323
318	232.1	169.7	0.1071	0.0017	2.68E-05	4.32E-07
319	169.7	384.16	174.5	0.10851	0.00172	2.76E-05
320	0.1071	174.5	395.09	179.4	0.11149	0.00179
321	0.0017	0.10851	179.4	406.03	184.3	0.11638
322	2.68E-05	0.00172	0.11149	184.3	416.96	189.31
323	4.32E-07	2.76E-05	0.00179	0.11638	189.31	368.49

Table 3-10: Calculated capacitance matrix of disk 40 (pF)

Section	318	319	320	321	322	323
318		145.9				
319	145.9		150.1			
320		150.1		154.3		
321			154.3		158.6	
322				158.6		162.8
323					162.8	

Table 3-11: Deviation between FEM and calculated capacitances in disk 40

Section	318	319	320	321	322	323
318		15.1%				
319	15.1%		15.0%			
320		15.0%		15.0%		
321			15.0%		15.0%	
322				15.0%		15.1%
323					15.1%	

Table 3-12: Capacitance matrix of disk 40 to 41 using FEMM (pF)

Section	324	325	326	327	328	329
318	23.797	3.3815	0.05358	0.00085	1.34E-05	2.16E-07
319	3.3808	13.056	3.427	0.05423	0.00086	1.38E-05
320	0.05352	3.427	13.428	3.5232	0.05578	0.0009
321	0.00085	0.05428	3.5232	13.799	3.6192	0.0582
322	1.34E-05	0.00086	0.05574	3.6193	14.169	3.7765
323	2.16E-07	1.38E-05	0.0009	0.05821	3.7767	79.294

Table 3-13: Calculated capacitance matrix of disk 40 to 41 (pF)

Section	324	325	326	327	328	329
318	16.8					
319		17.3				
320			17.8			
321				18.3		
322					18.8	
323						19.2

Table 3-14: Deviation between FEM and calculated capacitances between disk 40 and 41

Section	324	325	326	327	328	329
318	34.5%					
319		28.0%				
320			28.0%			
321				28.0%		
322					28.1%	
323						122.0%

From the results seen in Table 3-11 and Table 3-14 it is evident that fringing plays a significant role and causes a considerable error when not taken into account. This is especially evident at the edges of the disk. For the capacitances between section 318 and 324 and also that of section 323 to 329 suggests that the fringing at the edge of the disk causes a higher capacitive coupling than that calculated.

3.4.4.3 Ground-capacitance validation

As a final evaluation of the capacitance model, the test-unit in 5.1 was simulated using the capacitance model methodology presented in this chapter. The total ground-capacitance of the test-unit was measured at 1 kHz with an RLC bridge and compared to the calculated total ground-capacitance. The results are shown in Table 3-15.

Table 3-15: Total winding capacitance to ground

Method	***Capacitance value (pF)***
Calculated using equation (3.6), (3.7), (3.8) and (3.14)	636
Measured	766

As discussed in 3.4.4.1, this deviation in measured and calculated values is influenced by various matters. Table 3-11 and Table 3-14 already indicated that the omittance of fringing in the capacitance calculation caused a significant error. Thus, by including the fringing effect in the calculation method the difference in measured and calculated capacitance values should reduce. The difference could also be further reduced by placing and electrostatic shield around the test subject to reduce the stray capacitive coupling to a confined area.

3.5 Modelling of damping due to losses

3.5.1 Calculation of copper losses

The resistance R of a conductor having a length of l and a cross sectional area of A be calculated using the following relation [47]:

$$R = \rho l/A \tag{3.24}$$

where ρ is the resistivity of the conductor material as shown in Appendix B. Due to the skin-effect, the effective area of the conductor reduces due to the reducing penetration depth. The penetration depth ς in a highly conductive medium excited at a frequency ω can be expressed using the following relation [23] [47]:

$$\varsigma = \sqrt{2/\omega\mu\sigma} \tag{3.25}$$

where μ is the relative permeability of the conductor and σ is the conductivity of the conductor. The effective area for a square conductor is then

$$A = \pi \cdot (GMD - 2 \cdot \varsigma) \tag{3.26}$$

where GMD is defined as per equation (3.3). For the purpose of this project, the angular frequency ($\omega = 2\pi f$) at which the losses are calculated are the mean frequency of the range over which the model are required to be valid, hence $f = 225\,kHz$. This method is used to calculate the resistance of each inductive branch.

3.5.2 Dielectric loss calculations

The dissipation factor represents the ratio of resistive to displacement current in an insulation medium and is expressed in the following equation [37] :

$$tan(\delta) = I_r / I_s \tag{3.27}$$

where I_r is the resistive current and I_s is the displacement current in the dielectric material. Equation (3.27) can be rewritten in the following form in terms of the applied potential across the insulation medium resulting in the following expression:

$$tan(\delta) = \left(\frac{V}{R}\right) / (V \cdot j\omega C) \tag{3.28}$$

The conductance of the insulation material can then be calculated if the dissipation factor is and capacitance is known and is expressed as:

$$G = tan(\delta) \cdot \omega C \tag{3.29}$$

The dissipation of a new transformer at 50 Hz is approximately 0.5 $\%$ [101]. This dissipation factor was also used in the calculation of the dielectric losses. The calculated capacitance matrix was used in (3.29).

Chapter 4 Model formulations and solution algorithms

4.1 Introduction

Chapter 3 presented the discretization of the model and the calculations of the model parameters. This chapter presents the two model formulations and the solution methods used to evaluate them. First the nodal formulation will be presented followed by a state-space formulation. Each formulation is solved using a different solution method. The two modelling methodologies are used to model the electromagnetic behaviour of the test-unit described in section 5.1. The discretisation was done the same for both methodologies. The electric circuit equivalent model of the test-unit contains 495 nodes including the excitation node, and 492 inductive branches.

4.2 Implementation of difference equation method on nodal model

4.2.1 Nodal formulated model synthesis

The nodal model used for modelling the power transformer winding presented in section 5.1 is synthesised without any losses. The only losses in the system are due to the small resistive elements connecting the excitation source and ground to the LC network as presented in Figure 4-1.

Using the $[\boldsymbol{L_n}]$ and $[\boldsymbol{C_n}]$ matrix as presented in Chapter 3 and a $[\boldsymbol{G_n}]$ matrix representing only the resistive elements connecting the system to the excitation source and to ground, the voltage distribution can be calculated using the following relation:

$$\left[\frac{d}{dt}[\boldsymbol{C_n}] + \int[\boldsymbol{L_n}]\,dt + [\boldsymbol{G_n}]\right]\boldsymbol{v}(t) = \boldsymbol{i}(t)\,. \qquad (4.1)$$

In this thesis equation (4.1) will be solved using the difference equation method as presented in the following section.

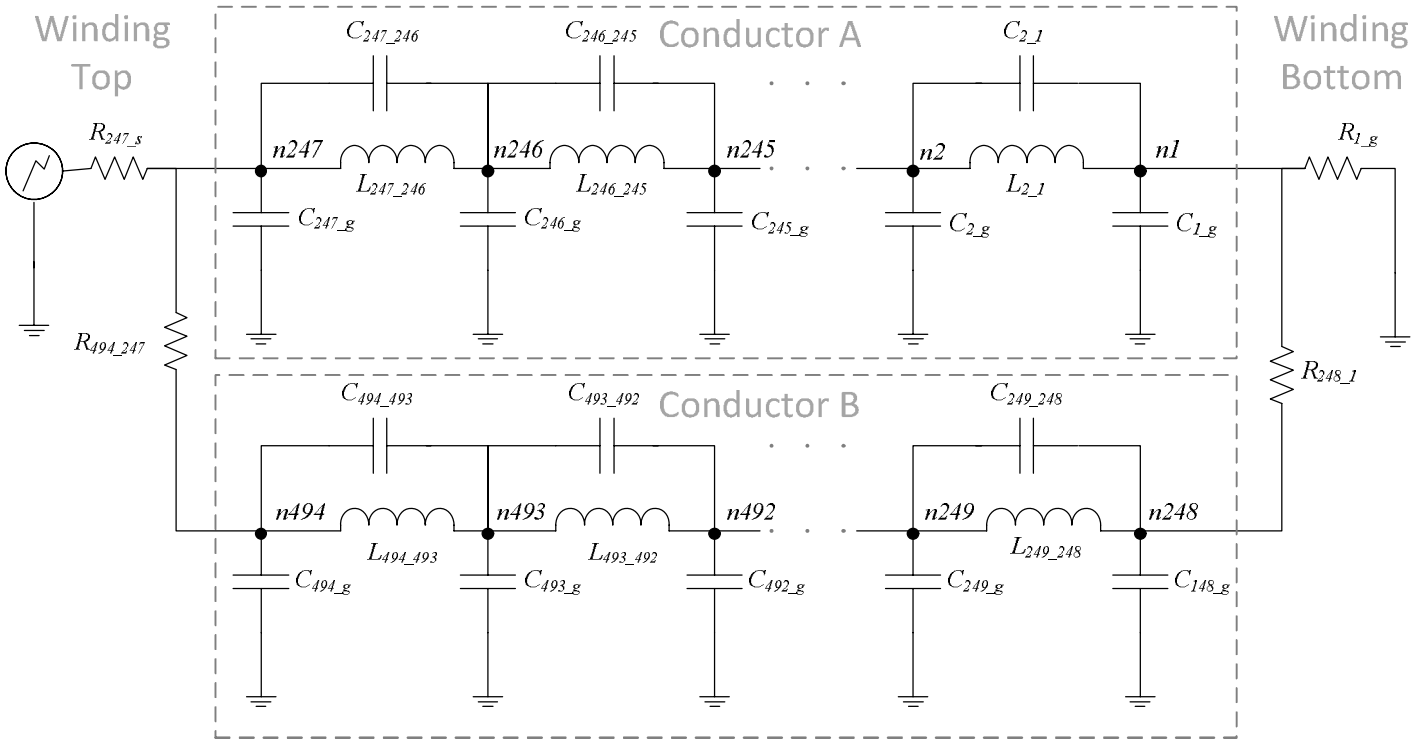

* Mutual inductive coupling and capacitive coupling between conductors not shown

Figure 4-1: Synthesis of nodal formulated electromagnetic model

4.2.1.1 *Difference equation method*

Dommel presented a paper whereby a large RLC network can be solved by transforming the inductive and capacitive elements to equivalent resistive elements by means of trapezoidal integration [102]. This solution method is known as the *difference equation method* (DEM). Using Figure 4-3 and Figure 4-4 as reference, the current through the inductor in Figure 4-2 – when using a resistive base element - can be expresses as [103] [102]:

$$i_{1-2}(t) = \frac{\Delta t}{2L}[V_1(t) - V_2(t)] + I_{1-2}(t - \Delta t)\,, \tag{4.2}$$

where

$$I_{1-2}(t - \Delta t) = i_{1-2}(t - \Delta t) + \frac{\Delta t}{2L}\,[V_1(t - \Delta t) - V_2(t - \Delta t)] \tag{4.3}$$

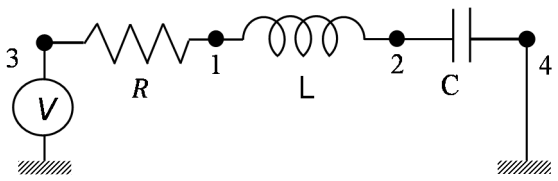

Figure 4-2: A Simple RLC circuit

The resistive network for the capacitive element can be expressed in a similar way using equation (4.4) and (4.5) with reference to Figure 4-5 and Figure 4-6.

$$i_{2-4}(t) = \frac{2C}{\Delta t}[V_2(t) - V_4(t)] + I_{2-4}(t - \Delta t) \tag{4.4}$$

where

$$I_{2-4}(t - \Delta t) = -i_{2-4}(t - \Delta t) - \frac{2C}{\Delta t}\,[V_2(t - \Delta t) - V_4(t - \Delta t)] \tag{4.5}$$

Unlike inductive and capacitive elements, a purely resistive element has no memory. Thus, with reference to Figure 4-7:

$$i_{3-1}(t) = \frac{1}{R}[V_3(t) - V_1(t)] \tag{4.6}$$

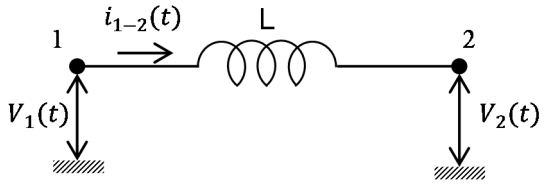

Figure 4-3: Inductive element

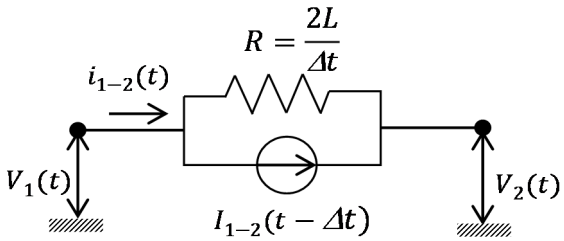

Figure 4-4: Equivalent resistive representation of inductive element

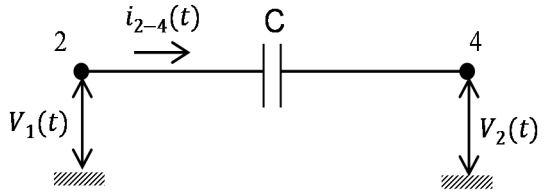

Figure 4-5: Capacitive element

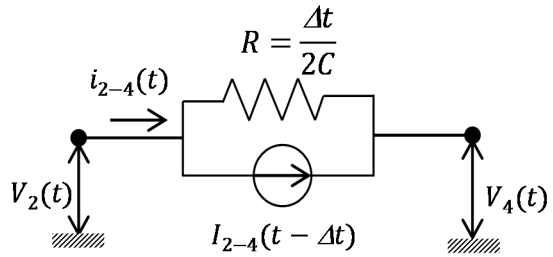

Figure 4-6: Equivalent resistive representation of capacitive element

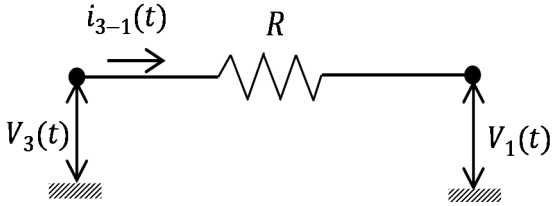

Figure 4-7: Purely resistive element

The network in Figure 4-2 can now be represented using Equations (4.2), (4.4) and (4.6) in matrix form:

$$[\boldsymbol{G}_n]\boldsymbol{V}(t) = \boldsymbol{i}(t) - \boldsymbol{I}(t - \Delta t) \tag{4.7}$$

where $[\boldsymbol{G}_n]$ is the nodal admittance matrix, $\boldsymbol{V}(t)$ is the nodal voltage column vector and $\boldsymbol{i}(t)$ and $\boldsymbol{I}(t - \Delta t)$ is the injected nodal current- and history current column vectors respectively.

The nodes can then be subdivided into group A and B for which the nodal voltages are unknown and known respectively. Rewriting equation (4.7) results in the following matrix equation [102] [103]:

$$\begin{bmatrix}[\boldsymbol{G_{AA}}] & [\boldsymbol{G_{AB}}] \\ [\boldsymbol{G_{BA}}] & [\boldsymbol{G_{BB}}]\end{bmatrix}\begin{bmatrix}\boldsymbol{V_A}(t) \\ \boldsymbol{V_B}(t)\end{bmatrix} = \begin{bmatrix}\boldsymbol{i_A}(t) \\ \boldsymbol{i_B}(t)\end{bmatrix} - \begin{bmatrix}\boldsymbol{I_A}(t - \Delta t) \\ \boldsymbol{I_B}(t - \Delta t)\end{bmatrix} . \tag{4.8}$$

The unknown voltages, $[\boldsymbol{V_A}(t)]$, can then obtained at each time step by solving the system of algebraic equations expressed in the following relation:

$$[\boldsymbol{G_{AA}}]\boldsymbol{V_A}(t) = \boldsymbol{I_{total}} - [\boldsymbol{G_{AB}}]\boldsymbol{V_B}(t) , \tag{4.9}$$

where

$$\boldsymbol{I_{total}} = \boldsymbol{i_A}(t) - \boldsymbol{I_A}(t - \Delta t) . \tag{4.10}$$

The base element does not need to be resistive, but could be capacitive or inductive as presented by Degeneff [103]. In this case equation (4.8) is expressed in terms of either magnetic flux if the base element is inductance or electric charge if the base element is capacitance. These have various advantageous depending of the context of application. In this thesis, a resistive base element has been chosen. For a nodal resistance matrix $\boldsymbol{R}_n$, nodal capacitance matrix $\boldsymbol{C}_n$ and an inverse nodal inductance $\boldsymbol{\Gamma}_n$, the admittance matrix used in the application of Dommel's method can be rewritten as:

$$[\boldsymbol{G}_n] = \left[\frac{\Delta t}{2}\boldsymbol{\Gamma}_n\right] + [\boldsymbol{R}_n] + \left[\frac{2}{\Delta t}\boldsymbol{C}_n\right] \tag{4.11}$$

4.2.1.2 Validation of solution routine

To implement equation (4.8) means that the nodes of the network must be arranged in such a way that the highest node numbers represent the excited and grounded nodes. To simplify the algorithm implementation, the highest node number represents the ground node and the preceding node is the point of excitation as depicted in Figure 4-2.

To test the solution routine, the step response of the small network in Figure 4-2 was solved and compared to the results obtained when the circuit response is calculated using Laplace transformation. The $[\boldsymbol{C}_n]$, $[\boldsymbol{\Gamma}_n]$, and $[\boldsymbol{R}_n]$ matrices were constructed manually and imported to the solution routine in MATLAB. The results are portrayed in Figure 4-8 and Figure 4-9 where a time step size Δt was chosen to be 1 μs and 0.075 μs respectively [104].

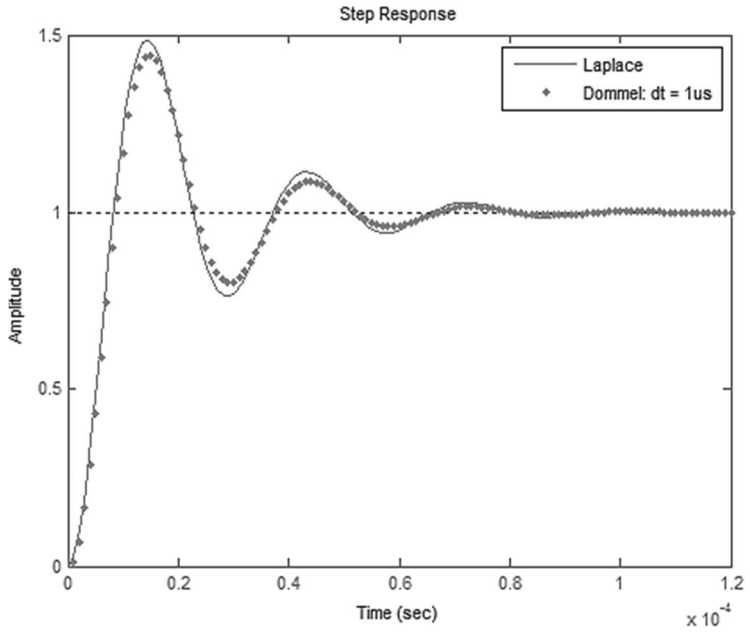

Figure 4-8: Step response of RLC circuit in using difference equation solving technique [104]

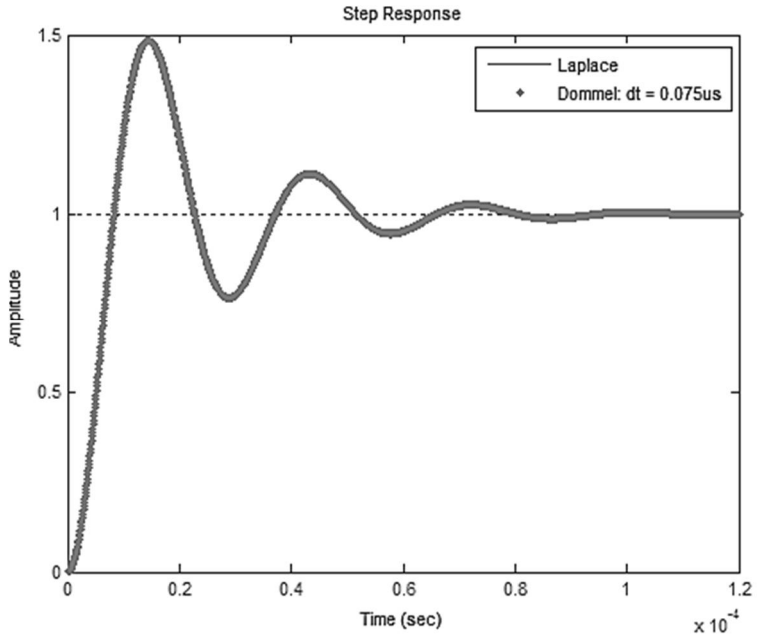

Figure 4-9: Step response of RLC circuit when compared to Laplace [104]

4.3 Application of 'lsim' function on a state-space formulation

4.3.1 State-space formulated model synthesis

Unlike the nodal formulated model in 4.2, another model was developed for the test-unit presented in section 5.1 which includes dielectric losses and losses in the inductive branches. This model is shown in Figure 4-10. The losses were calculated as presented in in section 3.5.

The formulation of the state-space equations representing the network presented in Figure 4-10 requires the $[\boldsymbol{L}_b]$ and $[\boldsymbol{C}_n]$ matrix as presented in Chapter 3. The $[\boldsymbol{G}_n]$ matrix in this formulation includes the conductive elements connecting the system to the excitation source and to ground as well as the dielectric losses associated with each capacitive element in the nodal capacitance matrix. $[\boldsymbol{R}_b]$ is a matrix having entries only on the diagonal which represents the copper loss of each branch.

Using a similar approach as that done by Fergistad, the column and row of $[\boldsymbol{C}_n]$, $[\boldsymbol{G}_n]$ of the excitation node is removed yielding $[\boldsymbol{C}_m]$, $[\boldsymbol{G}_m]$ respectively [14] [74]. The row relating to the excitation node is also removed from $[\boldsymbol{T}]$ yielding $[\boldsymbol{T}_m]$. $[\boldsymbol{L}_b]$ and $[\boldsymbol{R}_b]$ remains unchanged. $\boldsymbol{G}_m$ is the column removed from $[\boldsymbol{G}_n]$ without the row pertaining to the excitation node. The state-space formulation excited with a voltage $\boldsymbol{v_a}(t)$ is then realised as presented in the following relation:

$$\begin{bmatrix} \dot{\boldsymbol{v}_n}(t) \\ \boldsymbol{\imath}_b(t) \end{bmatrix} = \begin{bmatrix} -[\boldsymbol{C}_m{}^{-1}][\boldsymbol{G}_m] & -[\boldsymbol{C}_m{}^{-1}][\boldsymbol{T}_m] \\ [\boldsymbol{L}^{-1}][\boldsymbol{T}_m{}'] & -[\boldsymbol{L}^{-1}][\boldsymbol{R}_b] \end{bmatrix} \begin{bmatrix} \boldsymbol{v}_n(t) \\ \boldsymbol{i}_b(t) \end{bmatrix} + -[\boldsymbol{C}_m{}^{-1}]\, \boldsymbol{G}_m \cdot \boldsymbol{v_a}(t), \qquad (4.12)$$

where the unknown nodal voltages are then presented as:

$$\boldsymbol{v}_b(t) = [[\mathfrak{T}] \quad [\boldsymbol{0}]] \begin{bmatrix} \boldsymbol{v}_n(t) \\ \boldsymbol{i}_b(t) \end{bmatrix} \qquad (4.13)$$

$\mathfrak{T}$ is an identity matrix.

4.3.2 Matlab linear simulation tool

The state-space model presented above can be solved numerically using various numerical ODE solvers. Matlab contains various built-in ODE solvers and was therefore the preferred software platform to implement the solver routine. The *control system toolbox* of Matlab contains the *linear simulation tool* which can be used to solve a set of ODEs representing a linear system. The solver function pertaining to this simulation tool that was used in this thesis is called *lsim*.

The lsim function is capable of solving the system of ODEs for arbitrary inputs. The input to the function is the synthesised dynamic system model, time vector and the input signal corresponding to the time vector. In this context, the dynamic system model is represented by the state-space model.

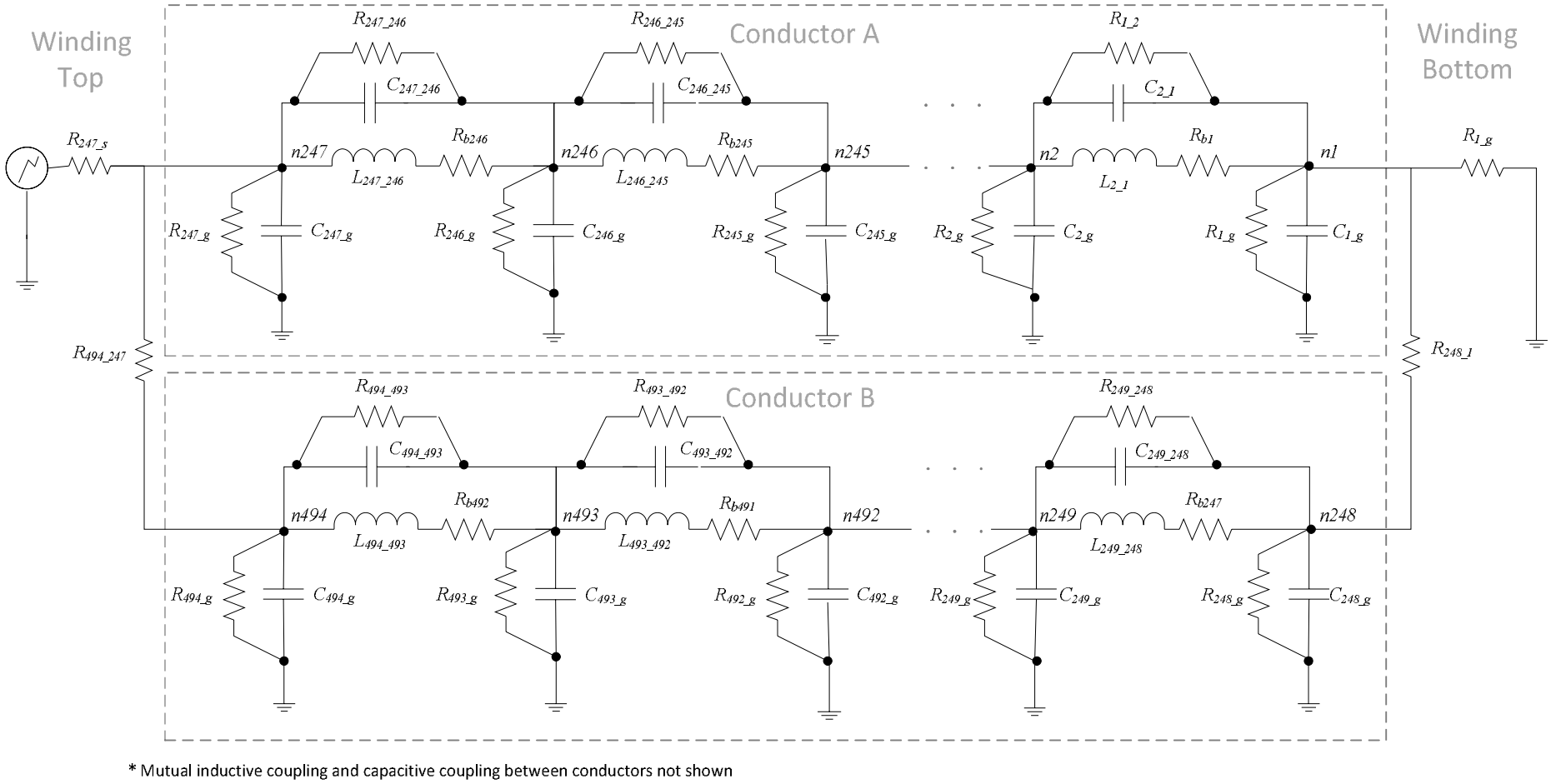

* Mutual inductive coupling and capacitive coupling between conductors not shown

Figure 4-10: Synthesis of state-space formulated electromagnetic model

Chapter 5 Model validation

5.1 Air-core reactor test-unit specifications

The complete model response was validated against measurements taken while applying a recurring low voltage LI on a disk winding air-core reactor. The reactor test-unit was constructed as a disk-type winding as referred to in section 2.2.4.2. There are 82 disks where each disk has three radial turns using two parallel conductors. The conductors are naturally transposed when the ordinary disk winding configuration is used similar to the illustration in Figure 2-7. Each conductor has two insulated strands which are transposed at the cross-over from disk 41 to disk 42.

Table 5-1: Winding construction detail

Number of disks	82	n/a
Number of turns per disk	3	n/a
Number of conductors per turn	2	n/a
Number of key spacers on circumference	12	n/a
Spacer thickness	3	mm
Spacer width	38	mm
Winding inner diameter	420	mm
Radial build of winding	37	mm

Table 5-2: Winding conductor detail

Number of strands radially	2	n/a
Number of strands axially	1	n/a
Strand height	9.95	mm
Strand width	2.5	mm
Strand edge radius	0.8	mm
Strand enamel covering thickness (double sided)	0.12	mm
Paper covering thickness of conductor (double sided)	0.8	mm

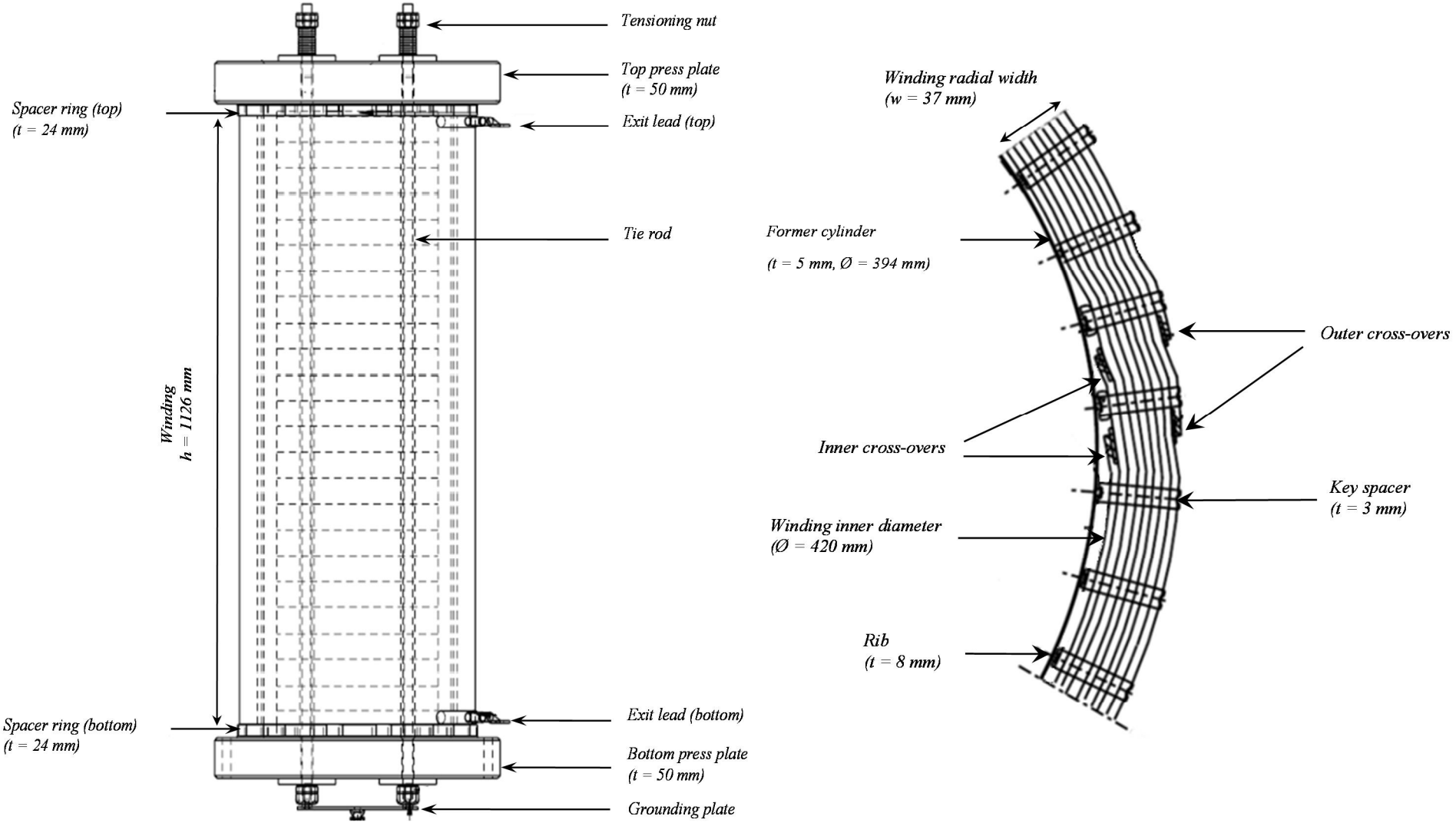

Figure 5-1: Geometrical detail of test-unit

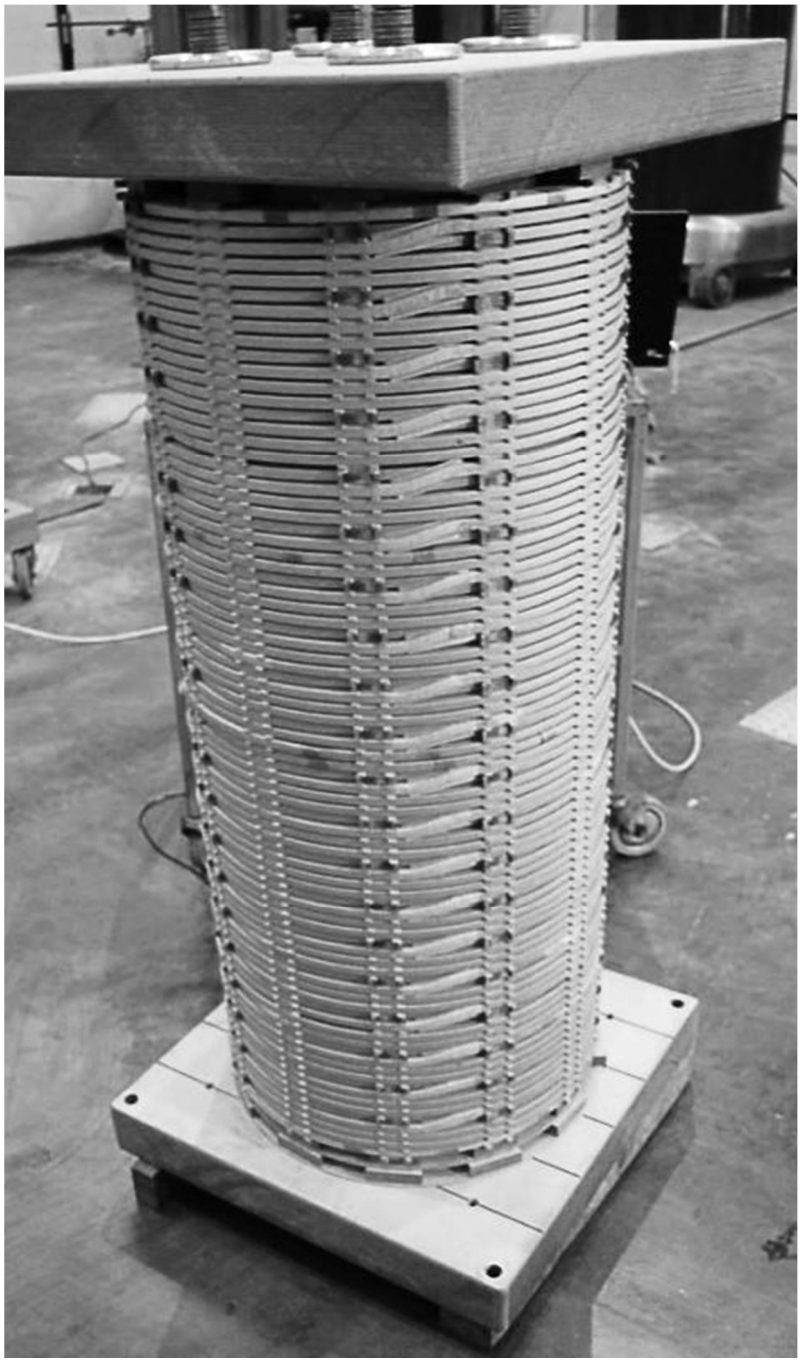

Figure 5-2: Actual test-unit

An electrostatic shield was fitted on the inside the former-cylinder of the disk winding to represent the surface of an iron-core. The shield was realised by cladding the inside of pressboard cylinder with aluminium foil. The diameter of the electrostatic shield is 376 mm. The shield may not form a closed cylinder otherwise it will behave like a shorted turn. To avoid this, a 5 mm wide strip was cut out of the foil from top to the bottom. The electrostatic shield was held at ground potential at one end only to avoid circulating currents.

5.2 Experimental arrangement

Two sets of tests was performed and analysed in the arrangement shown in Figure 5-3. The first set of tests were done by exciting the winding with a standard low voltage LI by means of a recurrent surge generator. The second set of tests was done by exciting the winding with a standard low voltage LIC. For each test the voltages $v_1(t)$, $v_2(t)$ and $v_3(t)$ was measured at the three places along the height of the winding as presented in Figure 5-4. The voltage $v_{term}(t)$ across the terminals of the winding represents the excitation wave. The measurements were done on the outer cross-over of the disks along the winding. The measurements and its respective place in the winding as well as its corresponding node in the electromagnetic model are presented in Table 5-3.

Table 5-3 : Location of measured voltages

Measurement	***Disk***	***Node***
$v_{term}(t)$	82	494
$v_1(t)$	62	434
$v_2(t)$	42	374
$v_3(t)$	20	308

The environmental parameters were measured at 1333 m above sea level using a T3004 Top Tronic temperature and humidity meter. The tests were conducted at an ambient temperature of 25 ^oC and a relative humidity of 46 % using the following equipment:

- Oscilloscope: Yokogawa DL850, Analogue voltage modules - 720210
- Recurrent Surge Generator: HAEFELY RSG 482
- Voltage probes: HAMEG HZ154 1:1/1:10

To ensure accurate measurements as discussed in section 2.7, the voltage probes were set to a ratio of 10:1. With reference to Figure 2-27, this increases R_p to 10 $M\Omega$ which is much higher that the winding resistance. The probe capacitance is 12 pF where the total C_g of the winding is 766 pF. In the arrangement of the ground lead was kept straight and as short as possible to lower L_g.

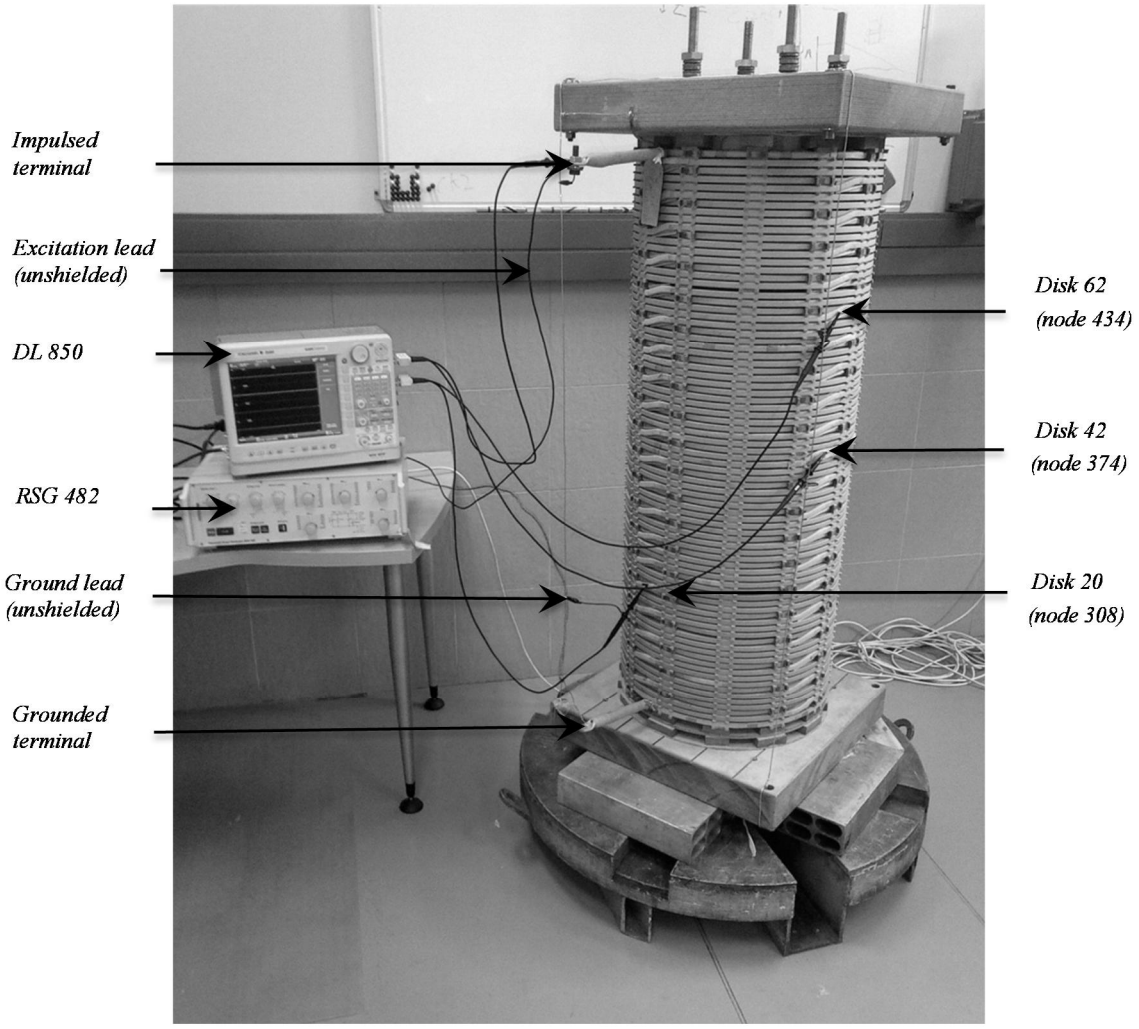

Figure 5-3: Experimental arrangement

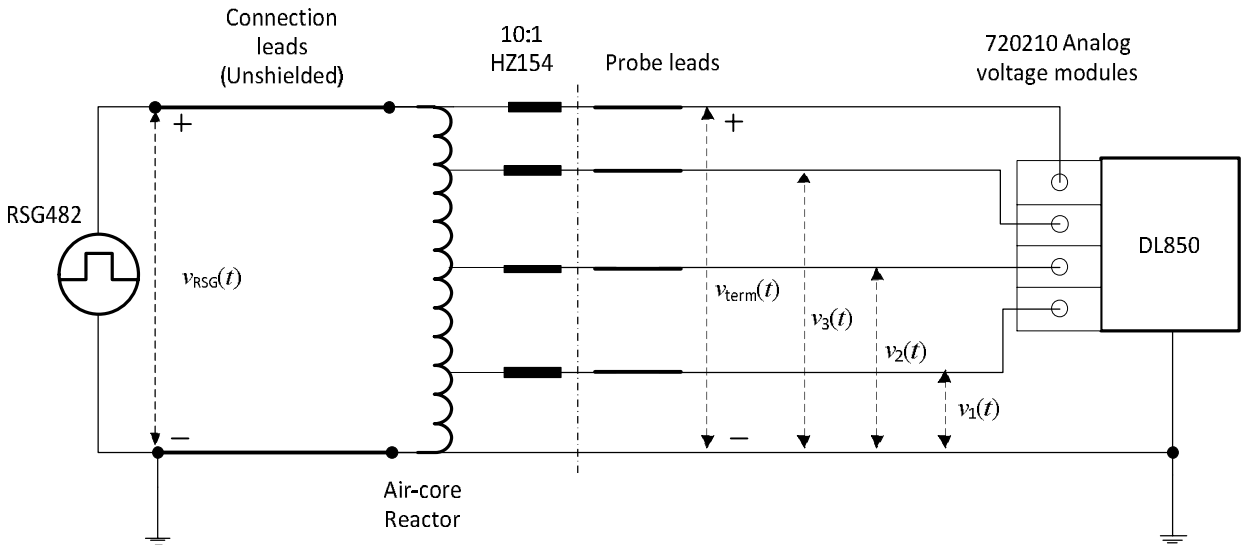

Figure 5-4: Diagram of experimental arrangement

Measurements were recorded at a sampling rate f_s of 100 MS/s at an 8 bit A/D resolution. In adherence with the principle presented by relation (2.27) the average acquired over 128 repetitive signals was used for each measurement. This was done to reduce the error caused by quantisation- and ambient noise. The parameter values of the recurrent surge generator with reference to the schematic in Figure 5-5 are given in Table 5-4. These parameters were used to obtain the low voltage standard 1.2/50 μs LI and LIC wave shapes.

Table 5-4: Recurrent Surge Generator Parameter Values

C_{serial} (μF)	R_{serial} (Ω)	C_{load} (nF)	$R_{parallel}$ (Ω)	L_{serial} (mH)
1	22	10	150	0

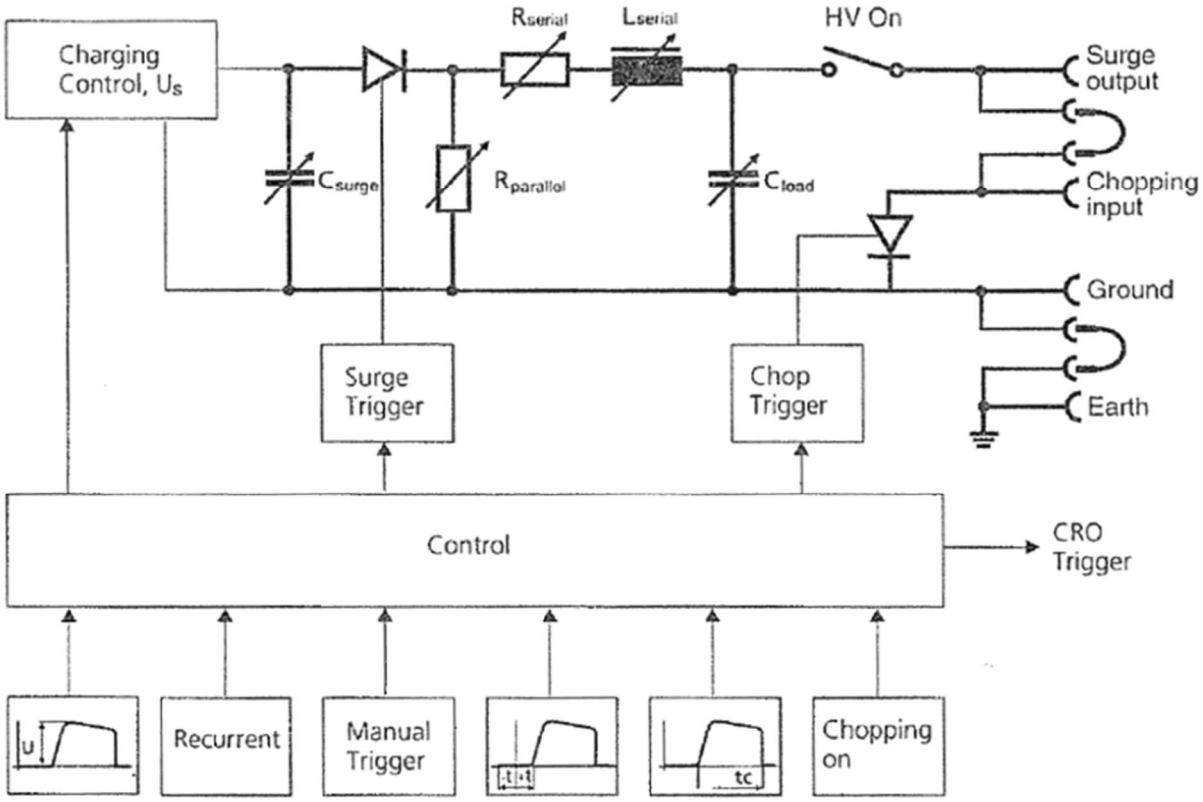

Figure 5-5: Schematic of HAEFELY RSG 482

5.3 Simulation results

5.3.1 Introduction

To validate the complete model in terms of the requirements set out in section 1.3.1, the LI and LIC standardised excitation waves were used. The measured voltages along the winding are compared to the calculated voltages. Initial validation is done using the measured excitation wave as the input to the model. Final validation is done by first generating the excitation waves using the mathematical expressions presented in 2.3.2. The measured signals were obtained using the experimental setup presented in section 5.2.

The two formulations presented in Chapter 4 with their respective solution methods were used to determine the model response. Having calculated results using two different solvers and formulations presents an opportunity to validate both model accuracy and solver fidelity. If any discrepancies occur during the comparison of measured- and calculated values, the source of error can be isolated.

The difference equation solution method is applied to a formulation that does not represent damping. Therefore a considerable deviation is expected in the time-domain representation of the calculated- and measured voltage signals. However, as mentioned in 2.4.4, the frequency content of the model response should not be affected by damping. If the calculated response of the model corresponds well in the frequency-domain using the two different solvers – regardless of accuracy – it would be a good indication the solvers are reliable. The state-space formulation does contain damping. If the developed model presented in Chapter 3 is correct, the time- and frequency representation of both the measured- and calculated voltage signals should correspond well if the state-space formulation is used.

5.3.2 LI excitation response

5.3.2.1 Measured LI system response

Using the arrangement presented in section 5.2, voltages along the winding were measured and are presented in Figure 5-6. The measured voltages at each location in the winding are individually compared to the calculated response at its respective node as presented in Table 3-1. The comparison is made in both the time- and frequency-domain.

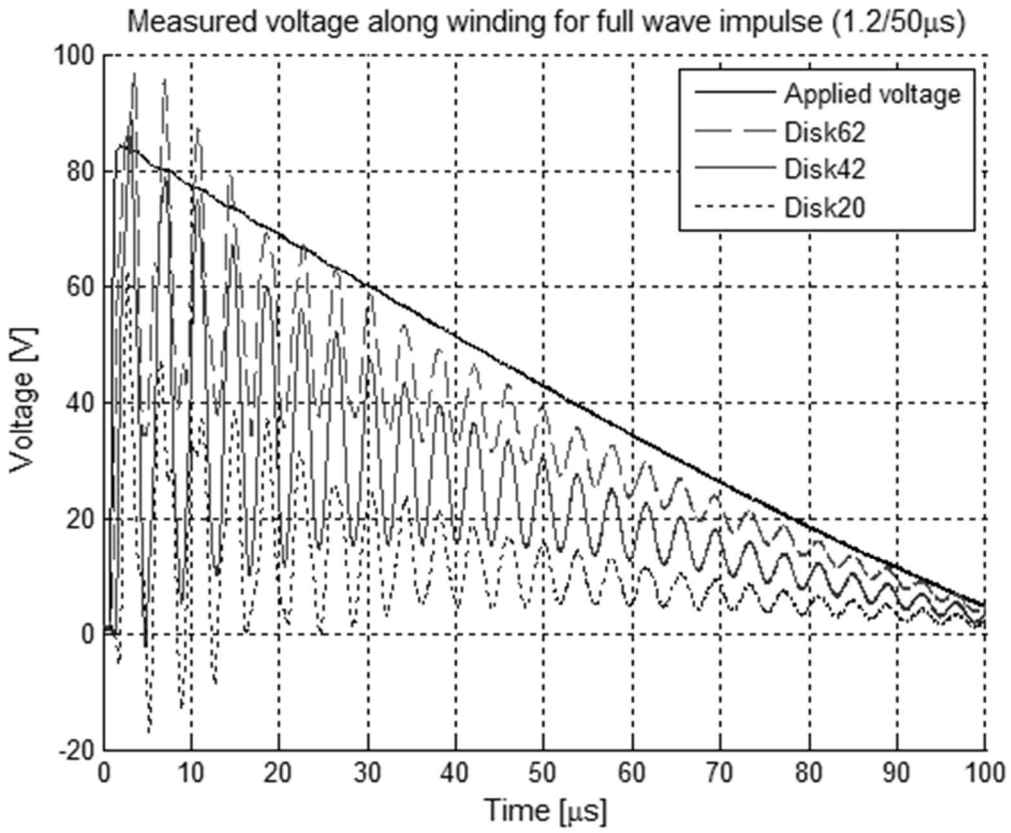

Figure 5-6: Measured voltage along air-core reactor for actual LI

5.3.2.2 LI response of nodal formulation solved with DEM

The application of DEM to the nodal formulation of the transformer model was evaluated and compared to the measured voltage waves. The measured voltage applied to the terminals of the test-unit was used as the input signal to the model.

The calculated and their respective measured voltage waves are presented in Figure 5-7 to Figure 5-12. In general the calculated time-domain response has a significant deviation from what is measured. This was expected since no damping is included in the equivalent electrical circuit model shown in Figure 4-1 used for the nodal formulation. The absence of damping elements causes the calculated voltage waves to maintain an oscillation of considerable amplitude while the measured voltage eventually reaches steady state. This is observed in Figure 5-7, Figure 5-9 and Figure 5-11.

In the frequency-domain the results look very promising. In Figure 5-8, Figure 5-10 and Figure 5-12 it can be seen that the first resonance point of the calculated and measured voltage waves is at nearly at the same frequency. The third and second resonance points for all three measured and calculated voltage waves also does seem to have a matching trend. These resonance frequencies f_{r1}, f_{r2} and f_{r3} are presented in Table 5-5. Another

matter that is evident from the frequency analysis is that the amplitudes of the resonance frequencies of the measured values are lower than that of the measured voltage waves. This is due to the absence of damping in the system.

Table 5-5: Resonance frequencies of model

	Measured kHz	*Calculated kHz*
f_{r1}	259.9	249.8
f_{r2}	569.8	529.8
f_{r3}	939.0	789.7

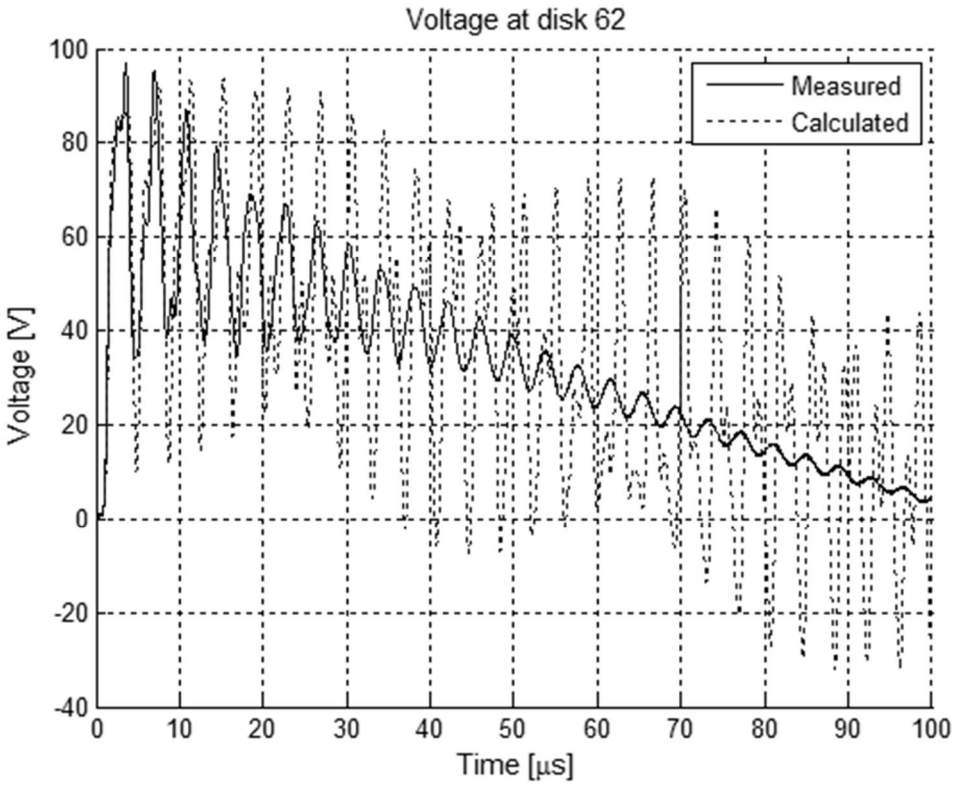

Figure 5-7: Measured and calculated voltages at disk 62 using DEM

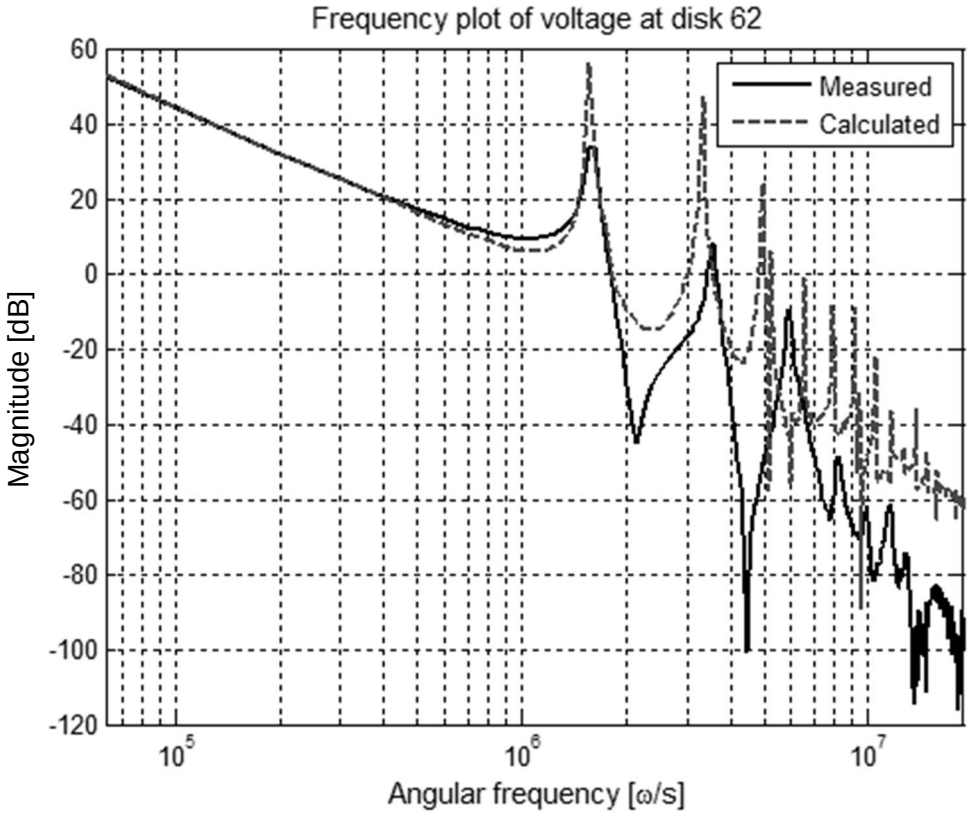

Figure 5-8: Frequency content of voltages at disk 62 using DEM

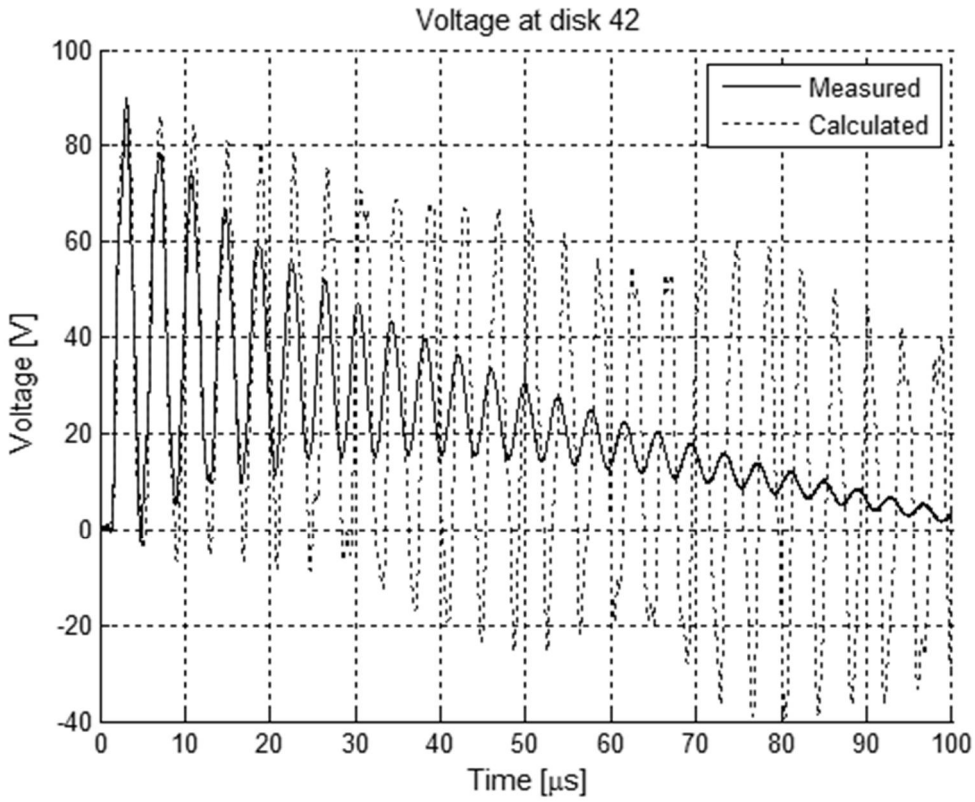

Figure 5-9: Measured and calculated voltages at disk 42 using DEM

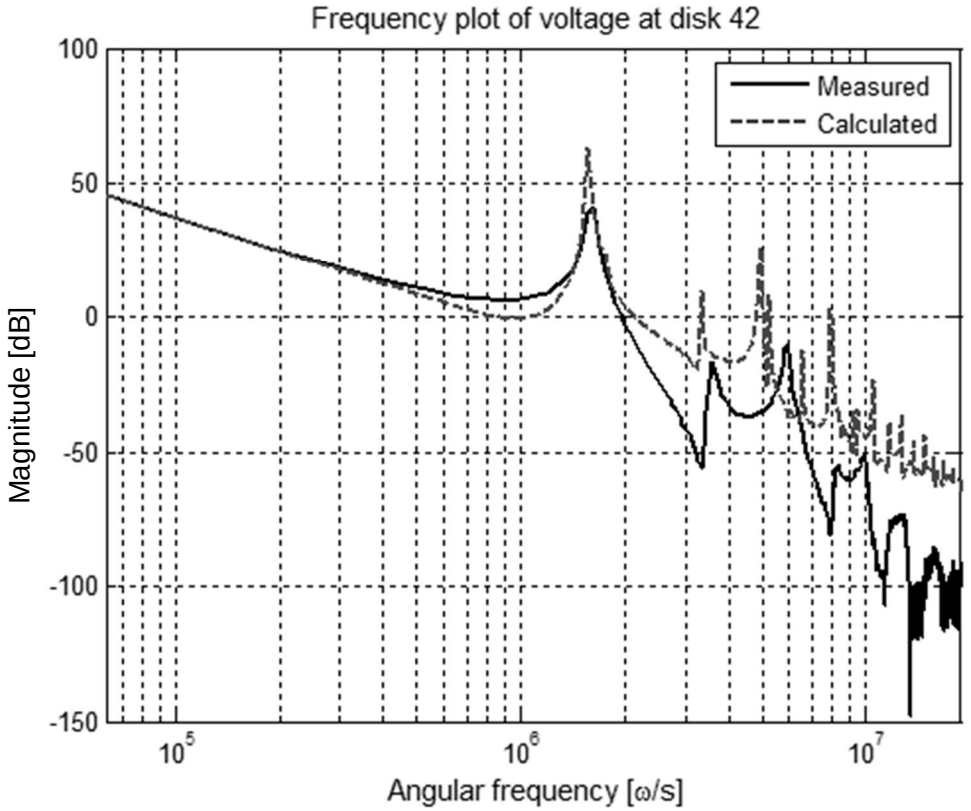

Figure 5-10: Frequency content of voltages at disk 62 using DEM

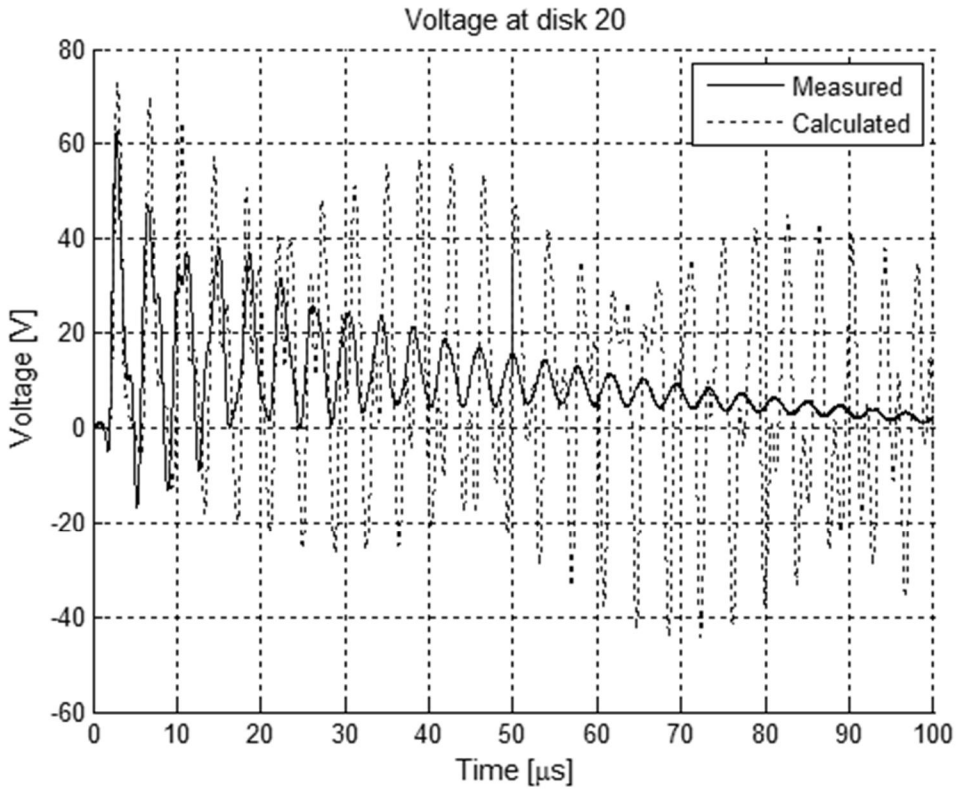

Figure 5-11: Measured and calculated voltages at disk 20 using DEM

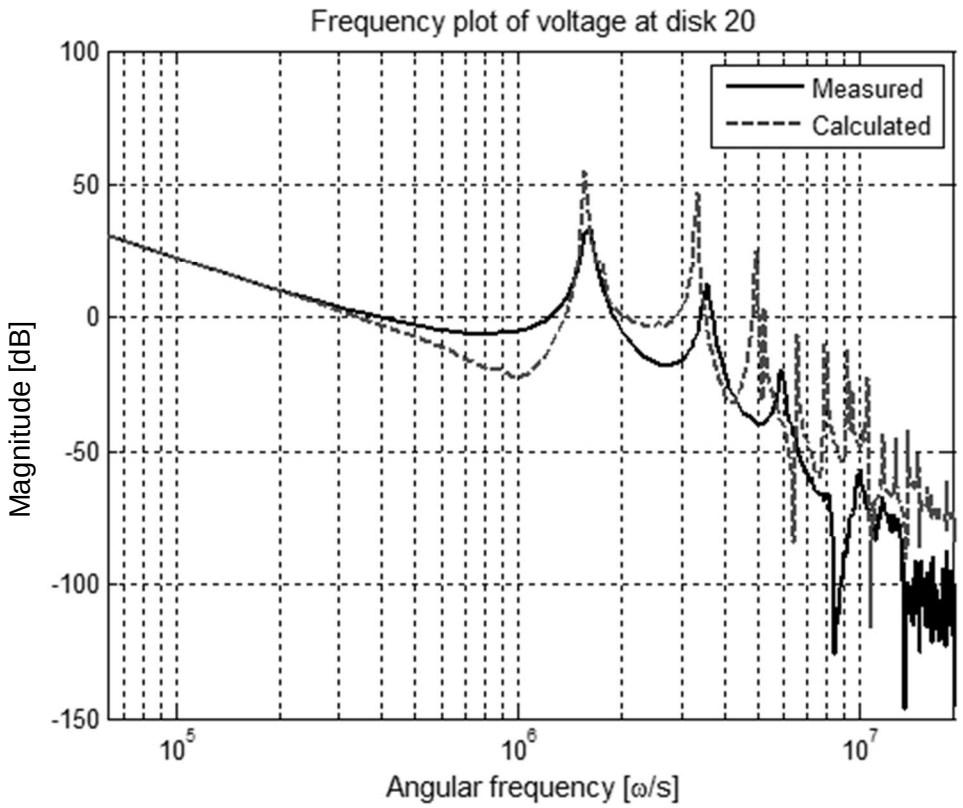

Figure 5-12: Frequency content of voltages at disk 20 using DEM

5.3.2.3 LI response of state-space formulation solved with LSim

The state-space formulation of the model was defined in Matlab® using the 'ss' function. The state-space model was solved using a linear differential solver function called 'lsim'. The measured voltage applied to the terminals of the test-unit was used as the input signal to the model.

The time-domain representations of the calculated and respective measured voltage waves are presented in Figure 5-13, Figure 5-15 and Figure 5-17. The time-domain voltage wave shapes correspond very well to the measured voltage waves. This is due to the fact that the state-space formulated model includes damping. This allows the calculated voltage wave to attenuate in an appropriate manner.

Since damping does not affect the frequency response noticeably, the frequency plot of the voltages calculated using the state-space formulation should not differ significantly from that of the nodal formulation. This can be seen in Figure 5-14, Figure 5-16 and Figure 5-18. The state-space formulation with damping yields the exact same resonance points as that of the nodal formulation without damping as presented in Table 5-5. It is also noticeable that the amplitude difference of the frequency components of the measured and calculated voltage wave forms is much less than that observed from the nodal formulated model. This is also due to the presence of the damping parameters in the state-space formulated model.

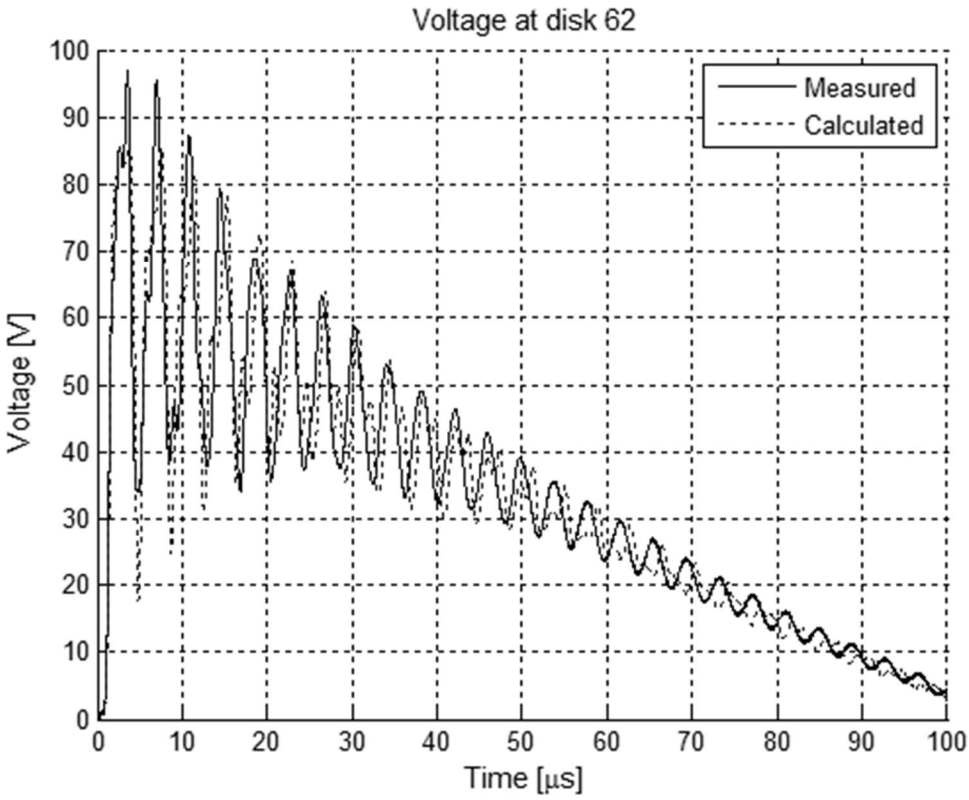

Figure 5-13: Measured and calculated voltages at disk 64 using state-space formulation

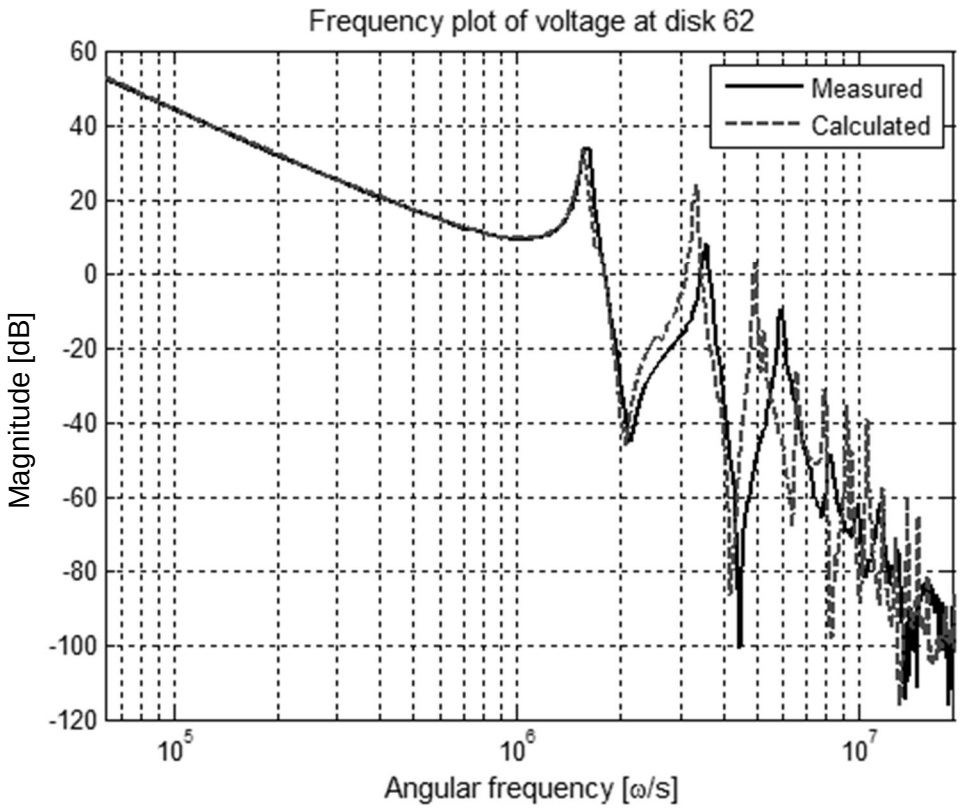

Figure 5-14: Frequency content of voltages at disk 64 using state-space formulation

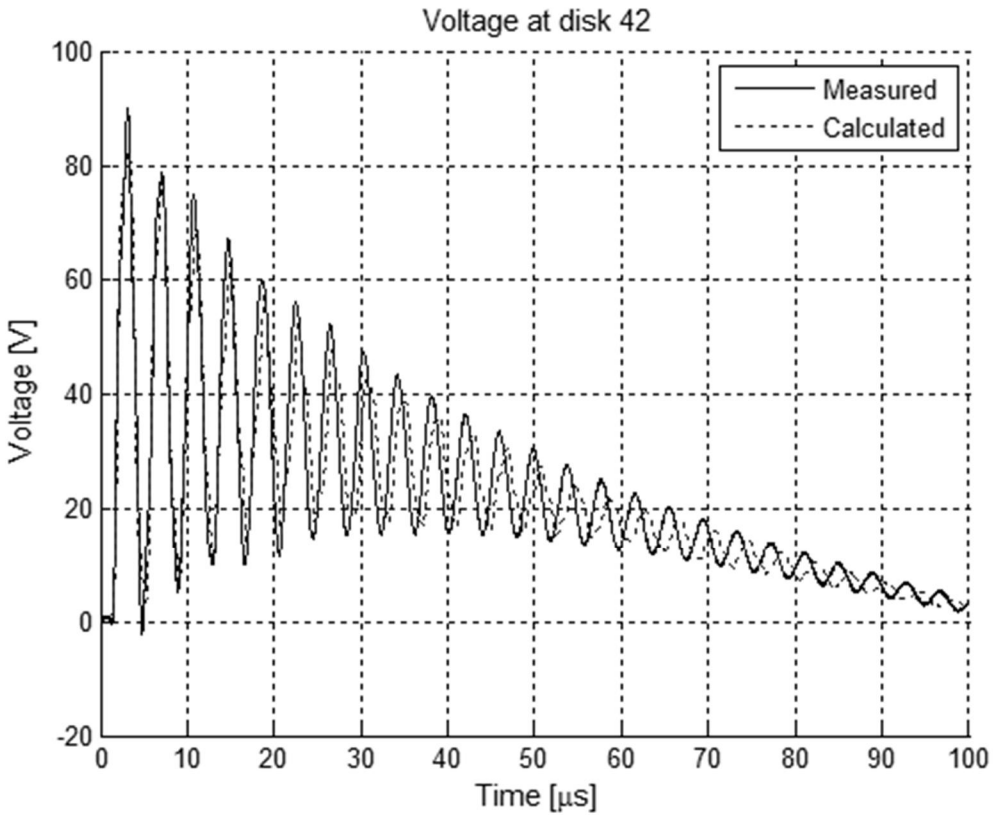

Figure 5-15: Measured and calculated voltages at disk 42 using state-space formulation

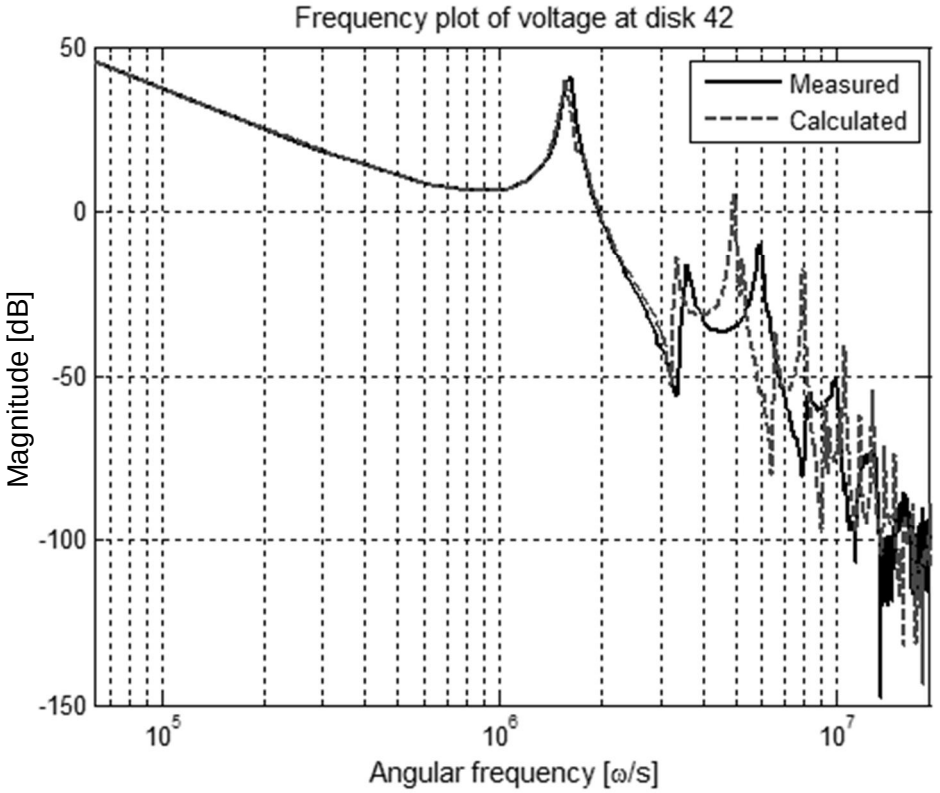

Figure 5-16: Frequency content of voltages at disk 64 using state-space formulation

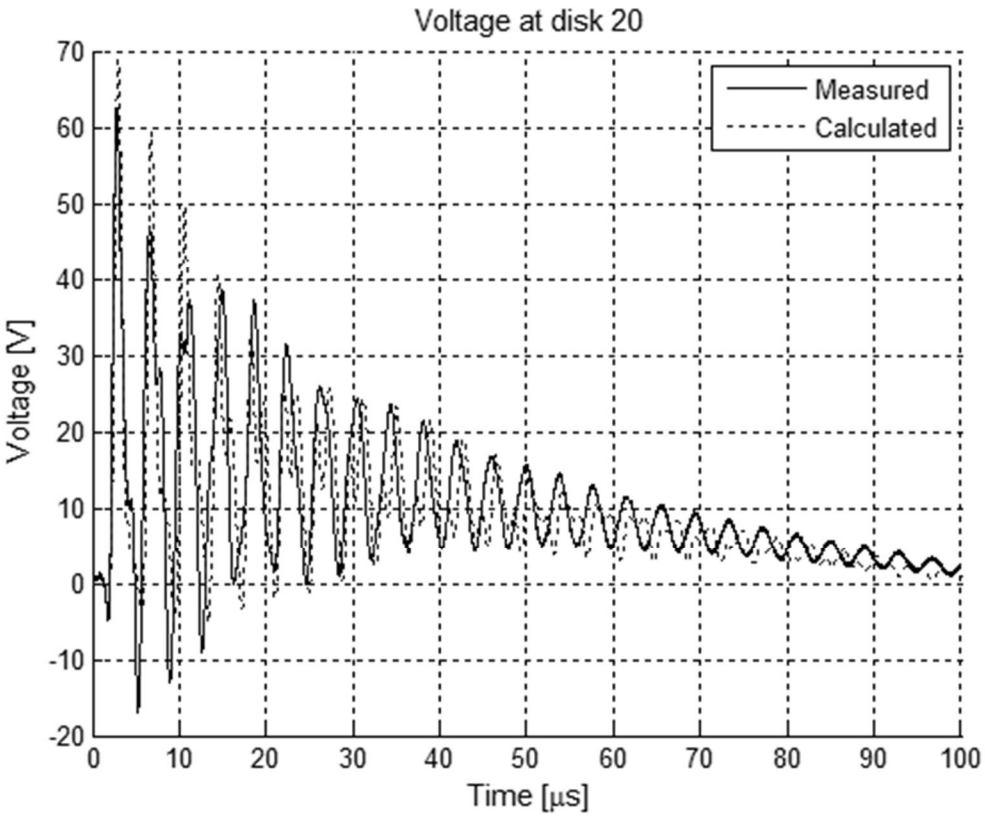

Figure 5-17: Measured- and calculated voltages at disk 20 using state-space formulation

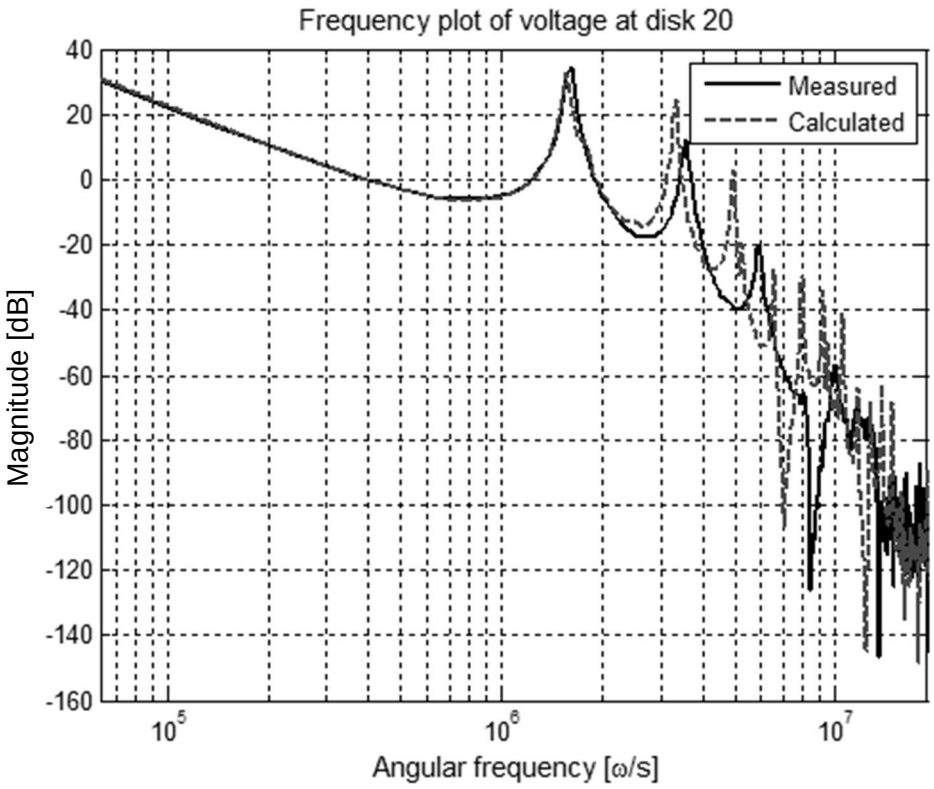

Figure 5-18: Frequency content of voltages at disk 64 using state-space formulation

5.3.3 LIC excitation response

5.3.3.1 Measured LIC system response

The LIC response of the test-unit was measured using the same arrangement as presented in 5.2. To obtain the desired wave shape, the standard LI was chopped on its tail at 6 µs. The measured voltages at disk 62, 42 and 20 is shown in Figure 5-19.

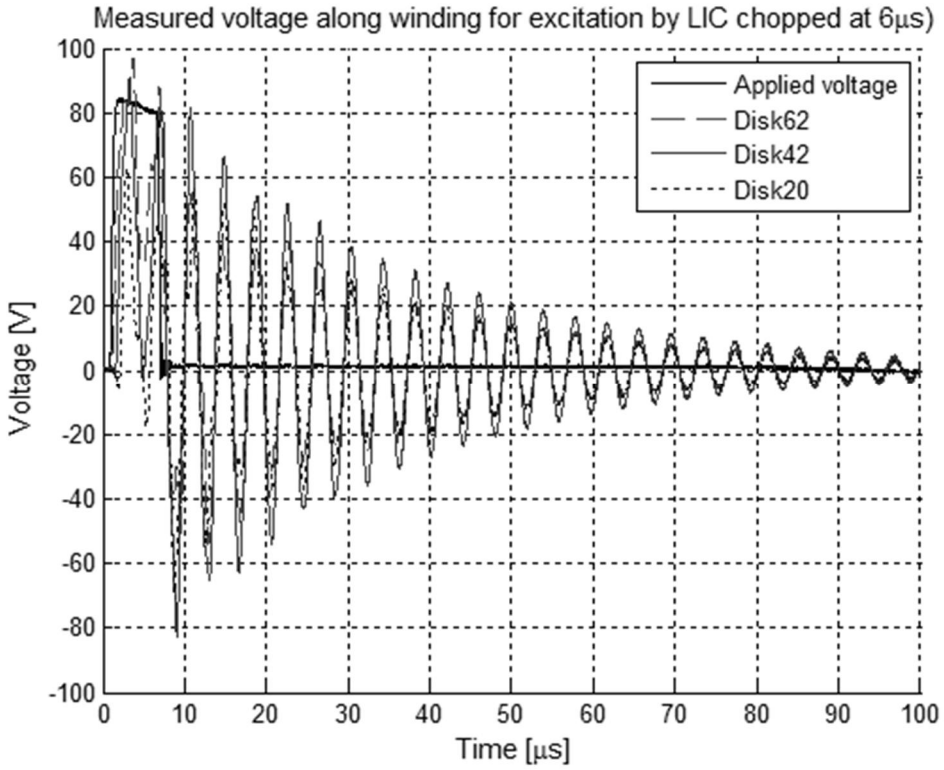

Figure 5-19: Measured voltage along air-core reactor for LIC

5.3.3.2 LIC response of nodal formulation solved with DEM

The nodal formulation of the model was solved using DEM. The measured LIC voltage across the terminals of the test-unit was used as the input signal to the model. The time-domain representation is presented in Figure 5-20, Figure 5-22 and Figure 5-24. As seen previously with the LI response of the model, the time-domain representation of the measured and calculated values agrees poorly due to the absence of damping parameters in the nodal formulated model developed in this study.

Apart from the difference in amplitude, the frequency-domain representation of the calculated values matches that of the measured voltage waves to a reasonable extent as seen in Figure 5-21, Figure 5-23 and Figure 5-25. The resonance frequencies of the measured- and calculated voltage wave forms coincide at the values shown in Table 5-5.

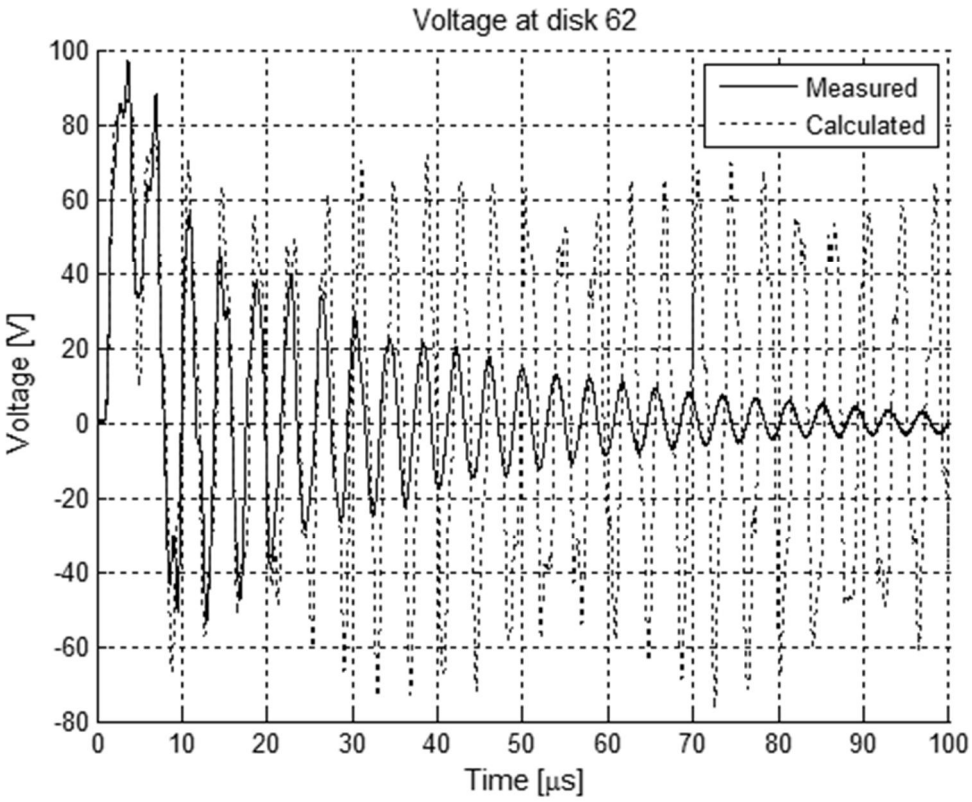

Figure 5-20: Measured and calculated voltages at disk 62 for LIC excitation using DEM

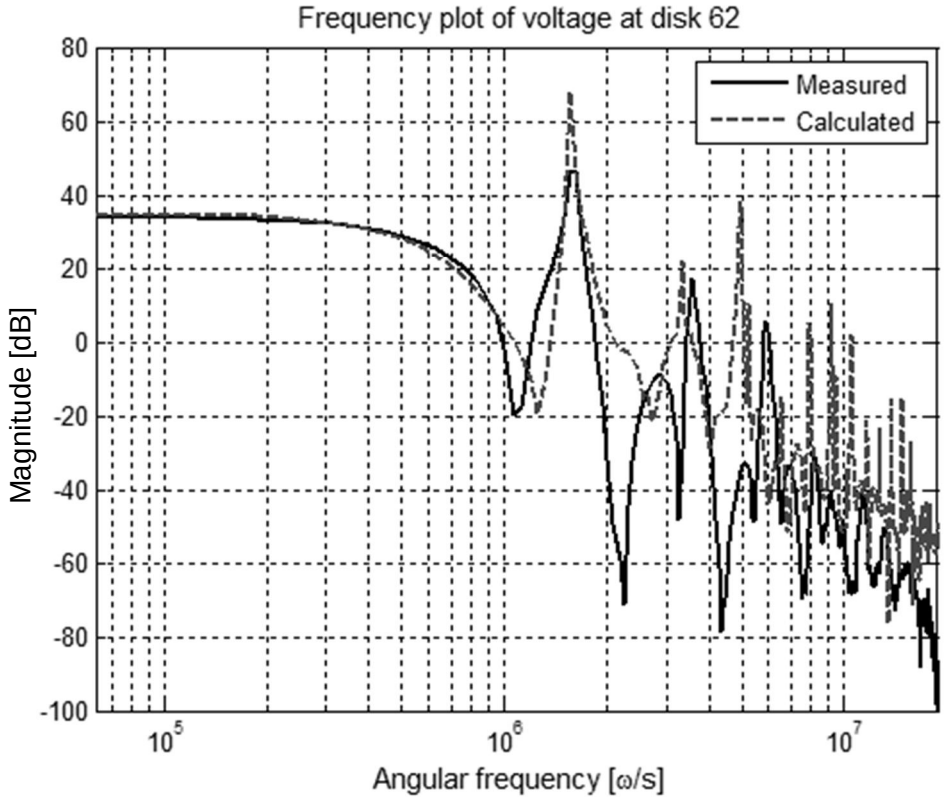

Figure 5-21: Frequency content of voltages at disk 62 using DEM for LIC excitation

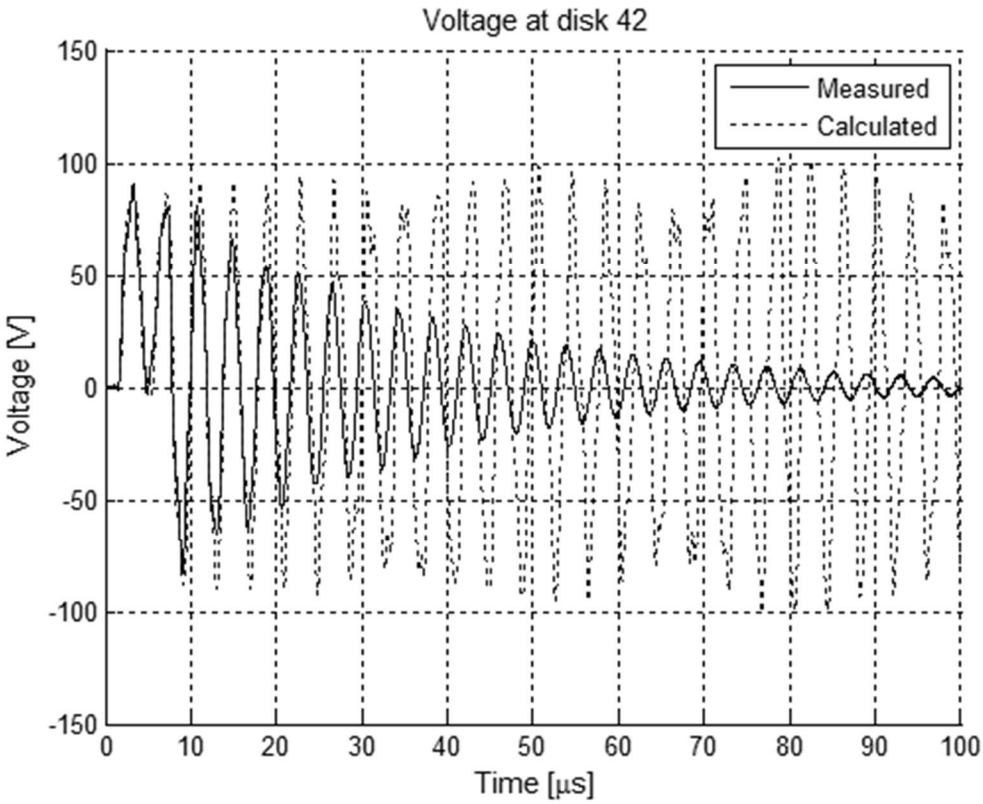

Figure 5-22: Measured and calculated voltages at disk 42 for LIC excitation using DEM

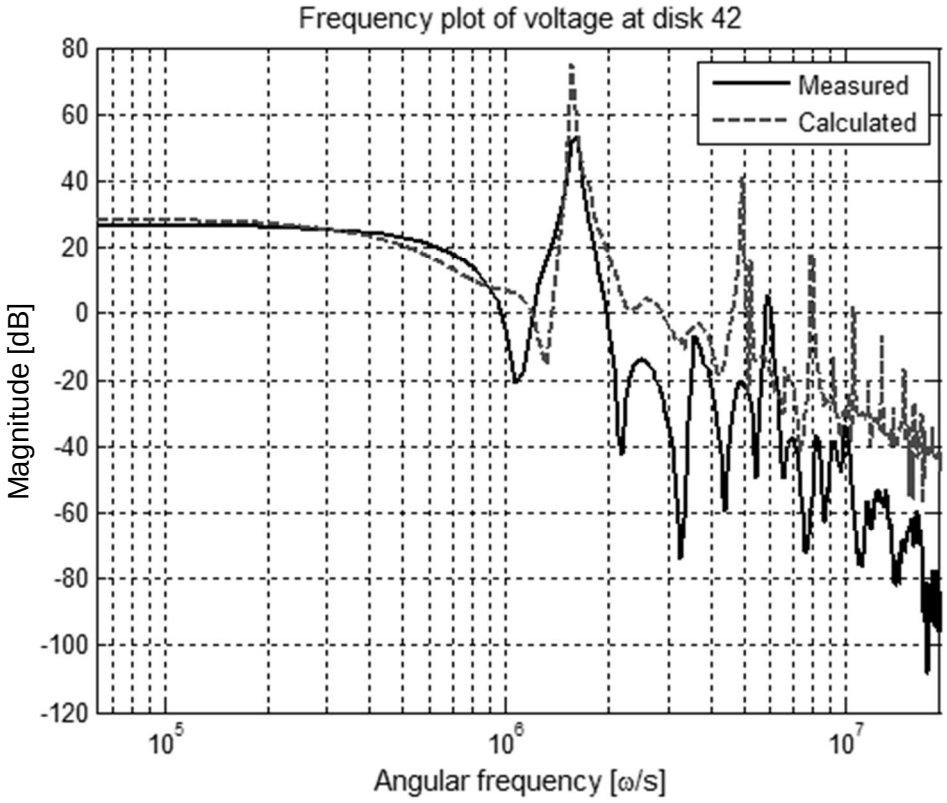

Figure 5-23: Frequency content voltages at disk 42 using DEM for LIC excitation

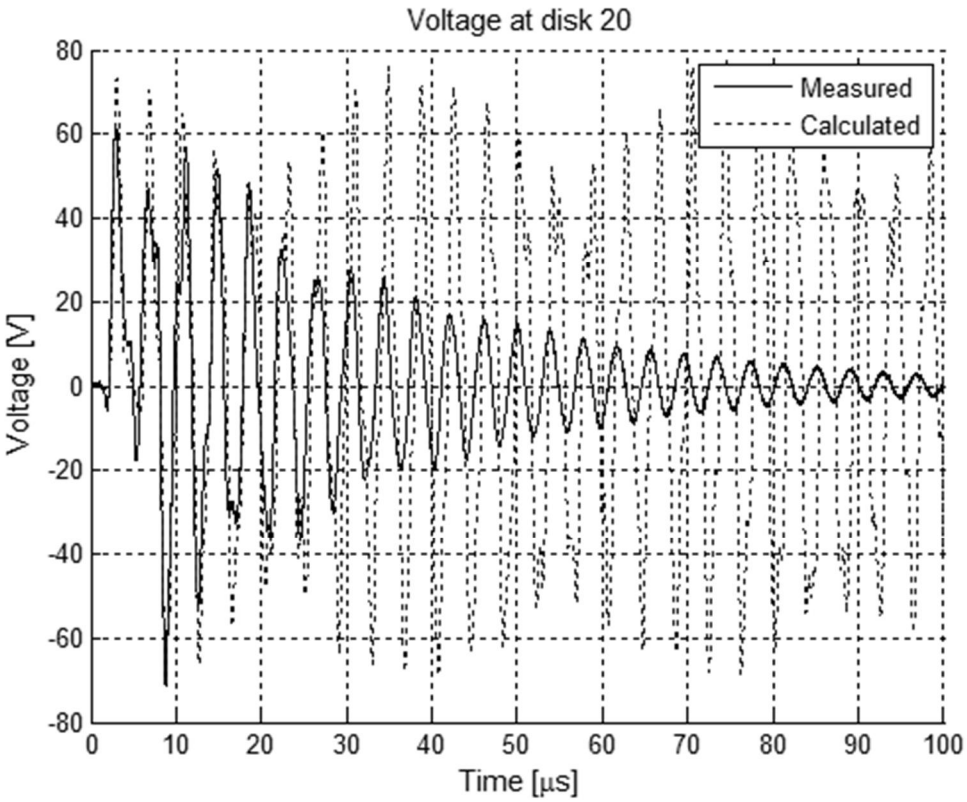

Figure 5-24: Measured and calculated voltages at disk 20 for LIC excitation using DEM

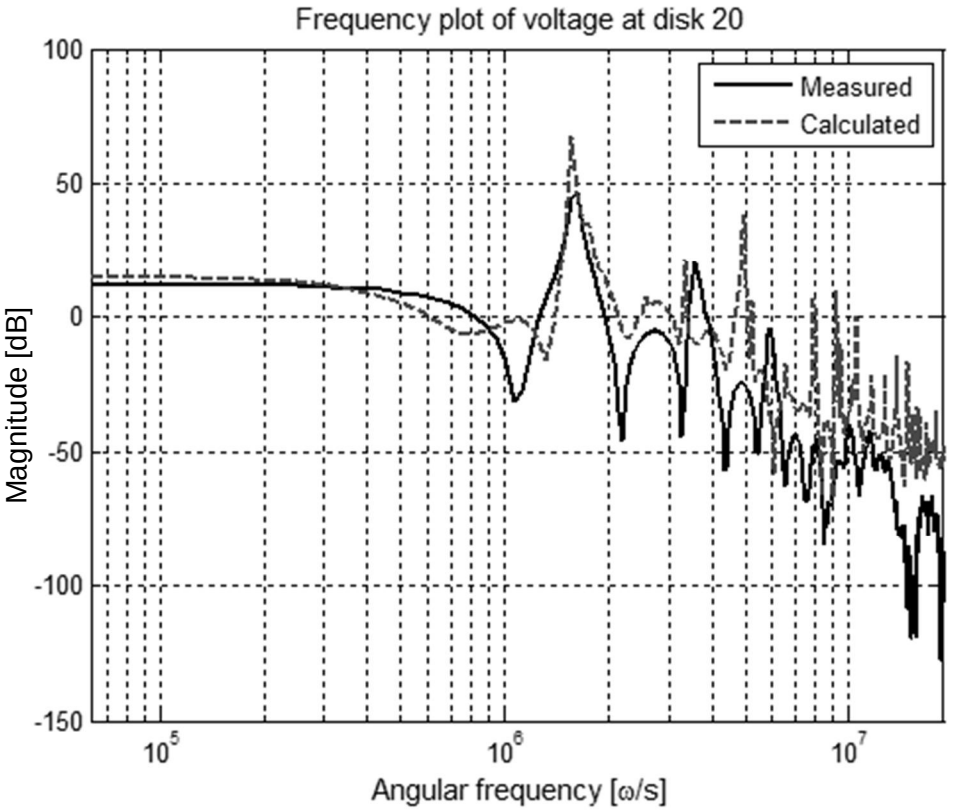

Figure 5-25: Frequency content of voltages at disk 20 using DEM for LIC excitation

5.3.3.3 LIC response of SS formulation solved with LSim

Using the state-space formulation, the model was solved for a LIC excitation wave using Matlab's 'lsim' function. The measured LIC voltage across the terminals of the test-unit was used as the input signal to the model. The time-domain representation is presented in Figure 5-26, Figure 5-28 and Figure 5-30. It is evident that the time-domain representation matches very well due to the damping elements in the state-space formulated model.

The frequency-domain representation of the measured and calculated voltage waves are shown in Figure 5-27, Figure 5-29 and Figure 5-31. Both amplitude and location of the resonance frequencies of the calculated response matches that of the measured values. These resonance frequencies are the same as those shown in Table 5-5.

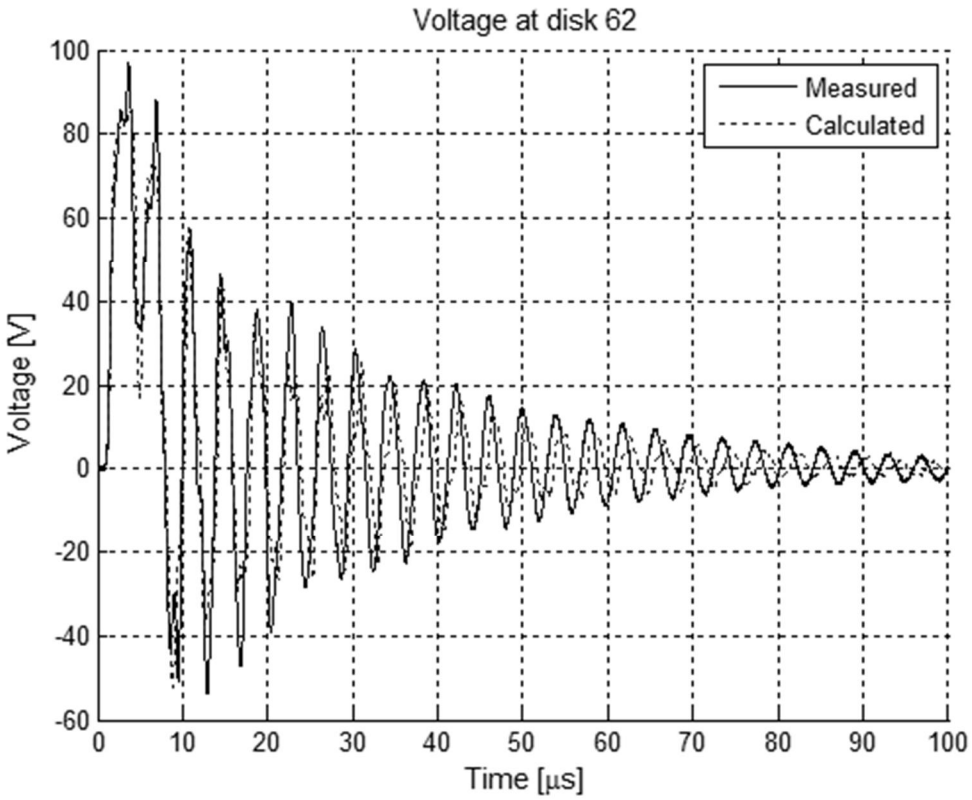

Figure 5-26: Voltages at disk 62 using state-space formulation (LIC)

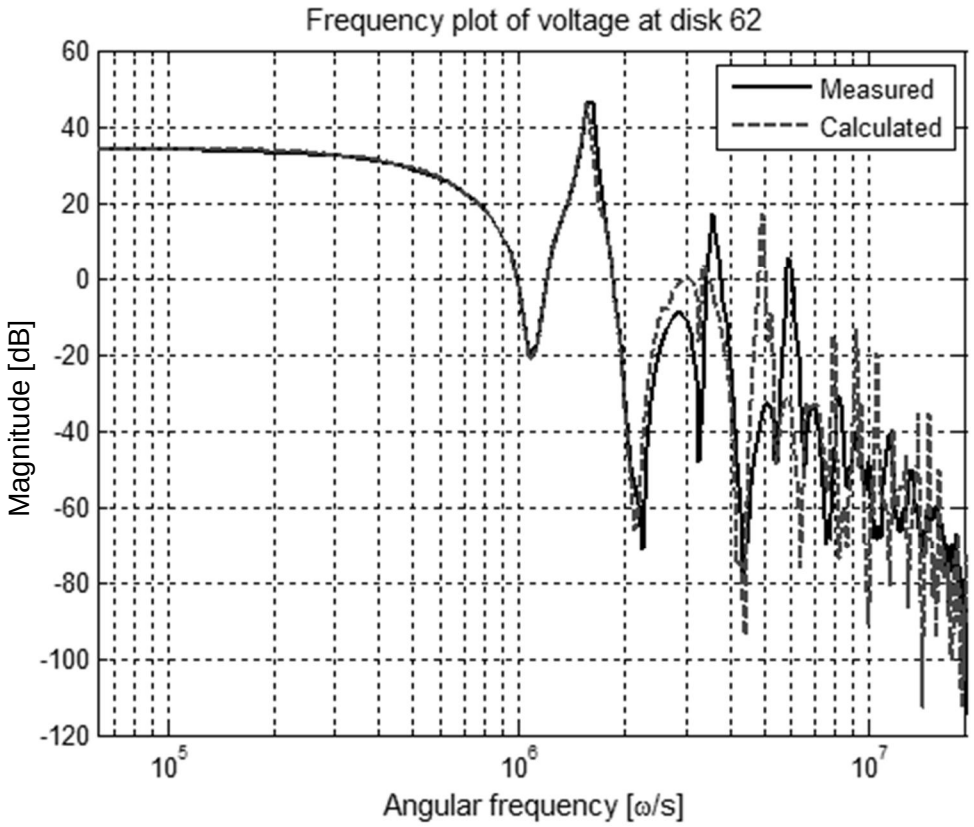

Figure 5-27: Frequency content voltages at disk 62 using state-space formulation (LIC)

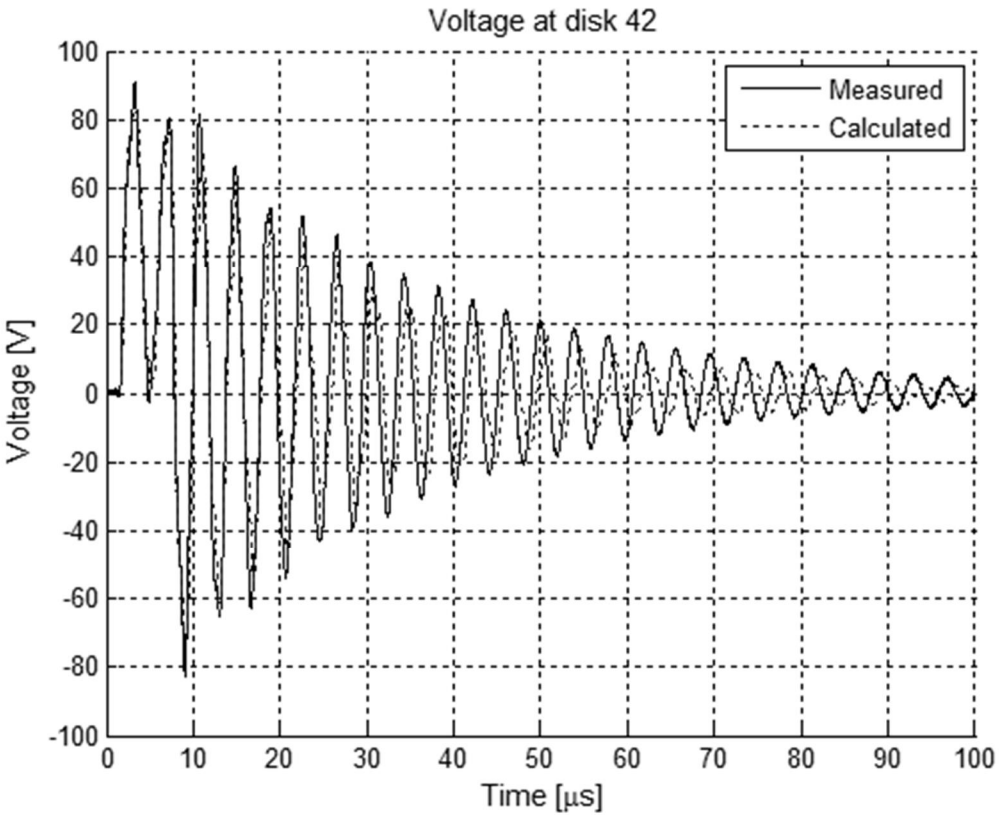

Figure 5-28: Voltages at disk 42 using state-space formulation (LIC)

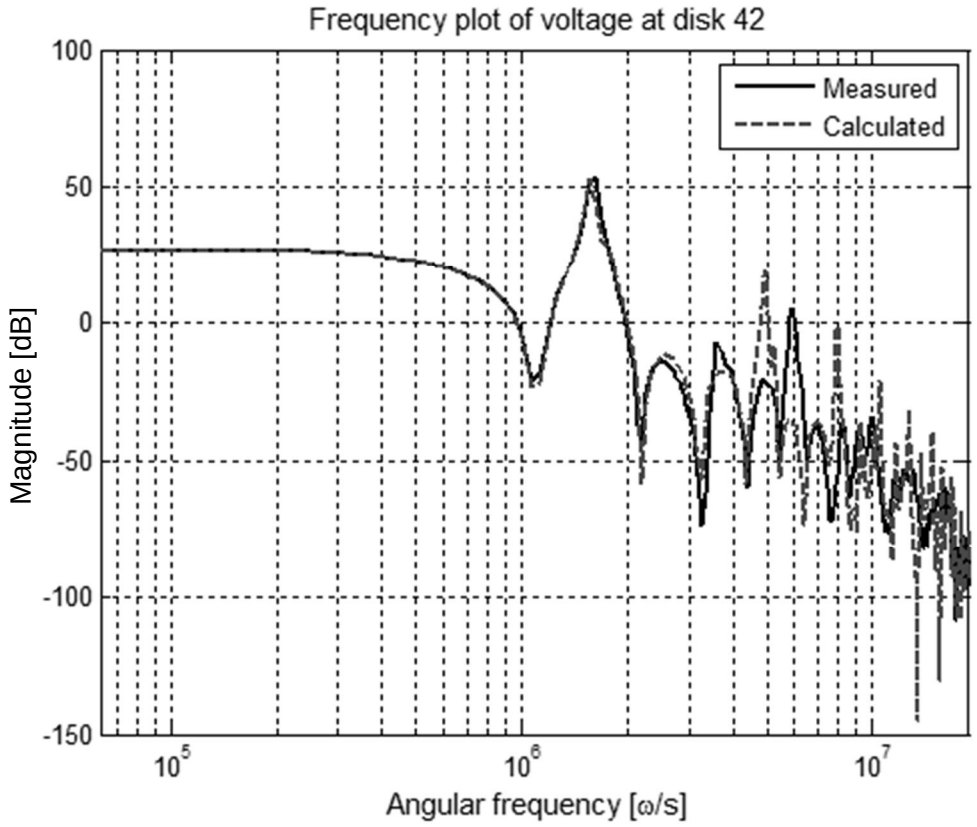

Figure 5-29: Frequency content voltages at disk 42 using state-space formulation (LIC)

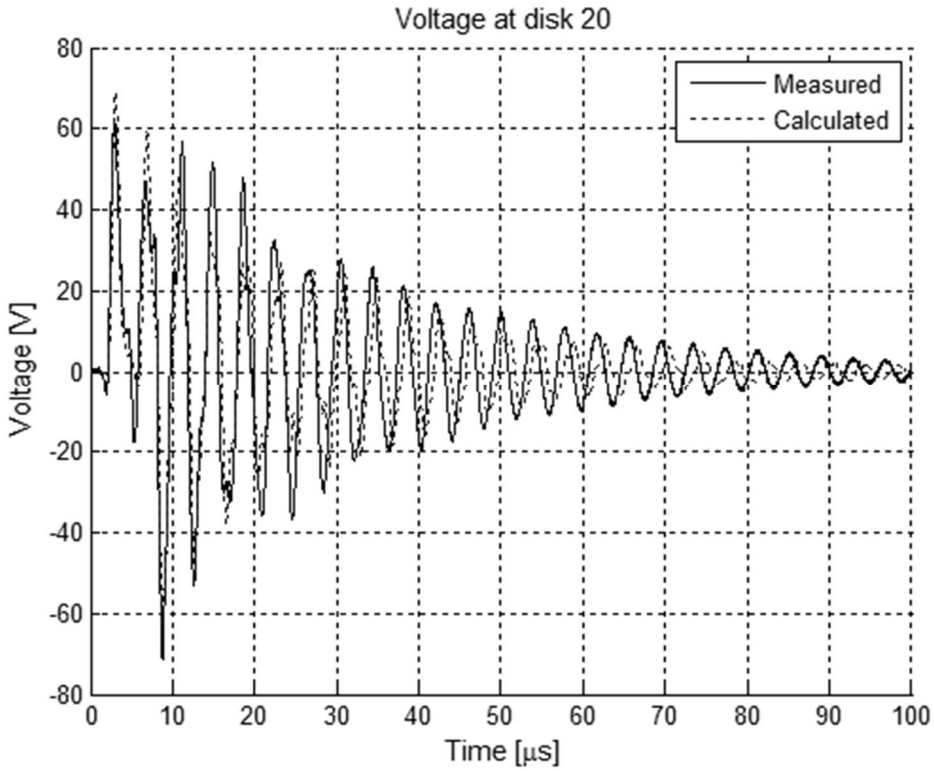

Figure 5-30: Voltages at disk 20 using state-space formulation (LIC)

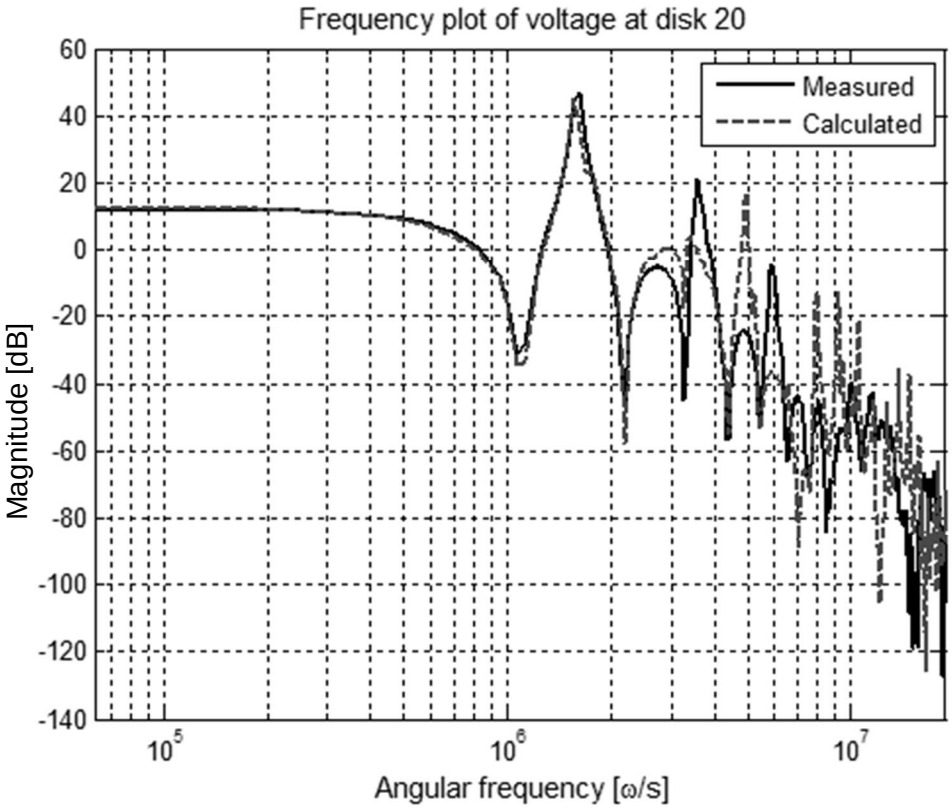

Figure 5-31: Frequency content of voltages at disk 20 using state-space formulation (LIC)

5.3.4 Function generated wave excitation

The response of the state-space formulated model was used to validate if the artificially created wave form which was generated using equation (2.3) is suitable for replicating the actual excitation wave. The time-domain representations are shown in Figure 5-32, Figure 5-35 and Figure 5-37. The result is very similar to that of an actual LI excitation wave input.

The frequency-domain representation shown in Figure 5-33, Figure 5-35 and Figure 5-37 also yields similar results as that shown in 5.3.2.3. In this study, the calculated excitation wave seems to be an appropriate substitute for the actual excitation wave.

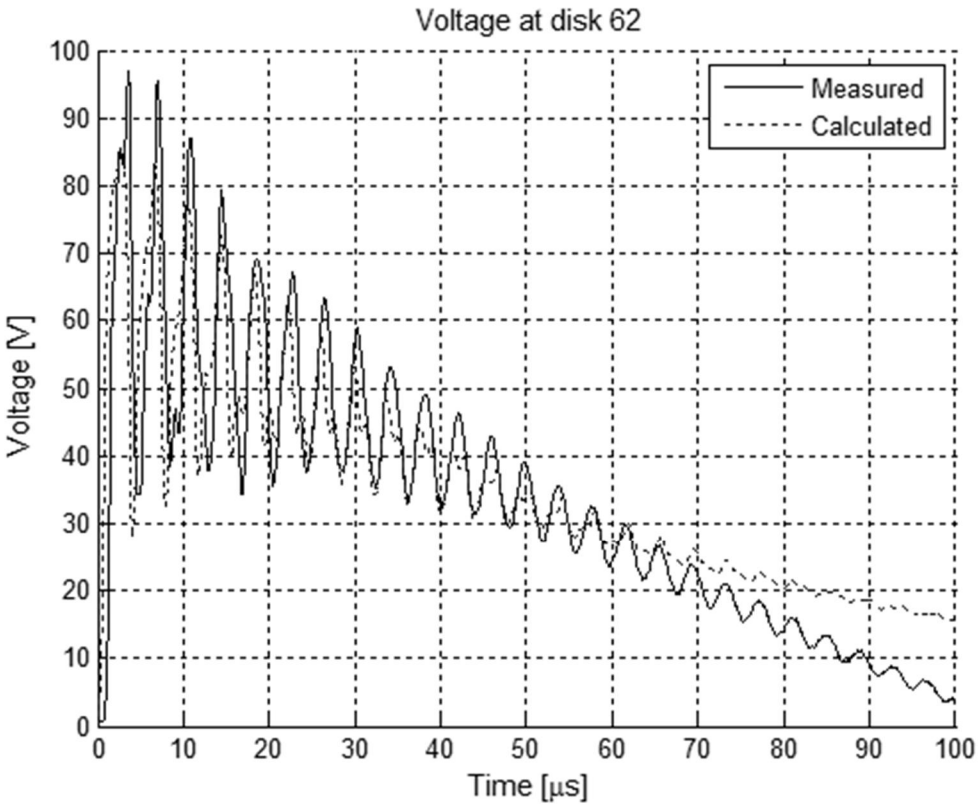

Figure 5-32: Voltages at disk 62 using state-space formulation (Generated LI)

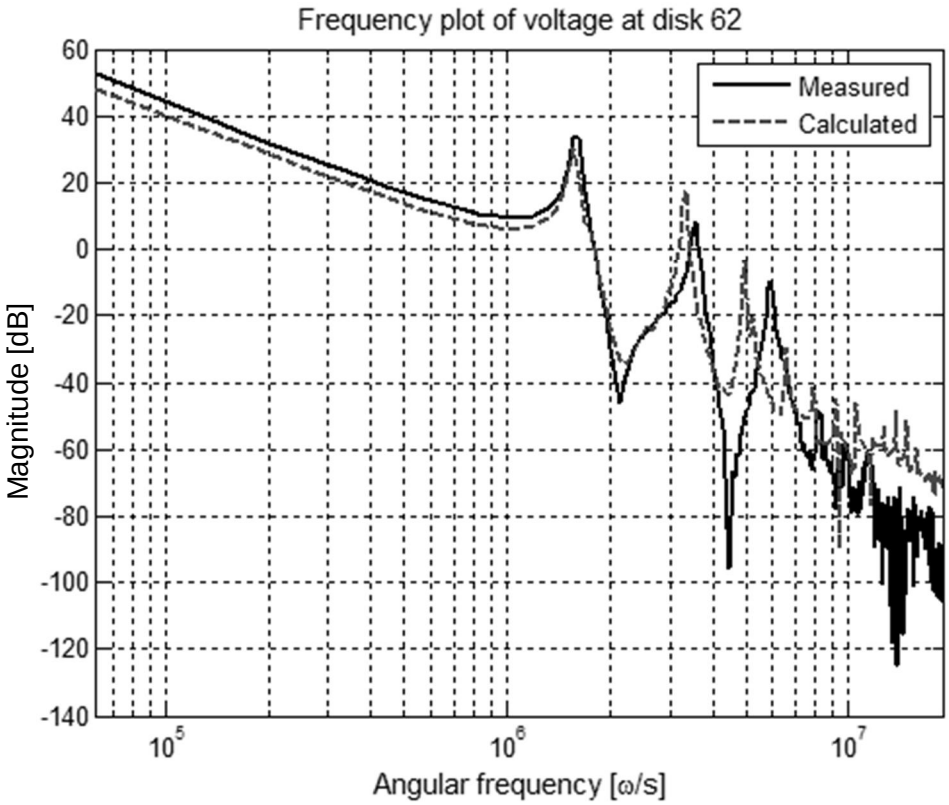

Figure 5-33: Frequency content of voltages at disk 62 (state-space formulation with generated LI)

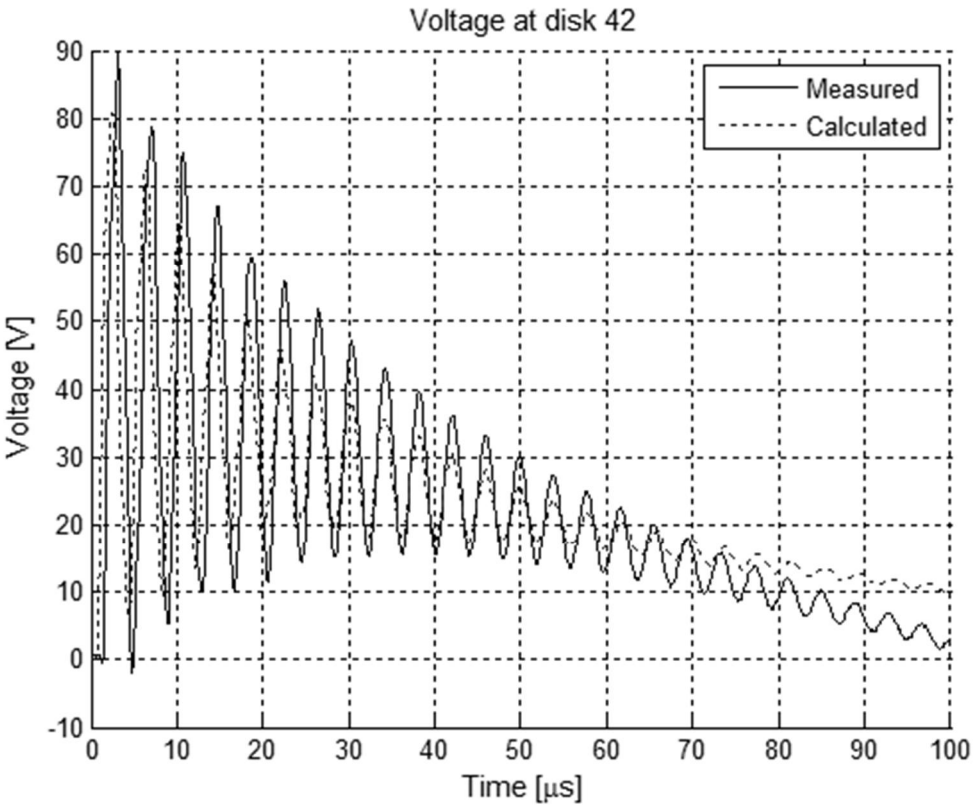

Figure 5-34: Voltages at disk 42 using state-space formulation (Generated LI)

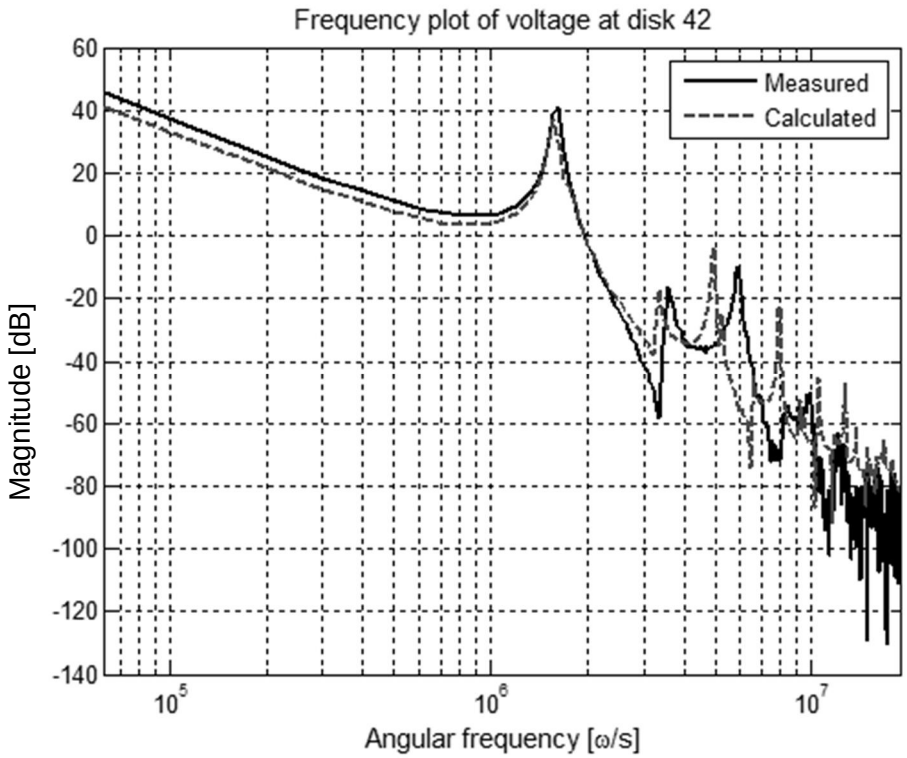

Figure 5-35: Frequency content of voltages at disk 42 (state-space formulation with generated LI)

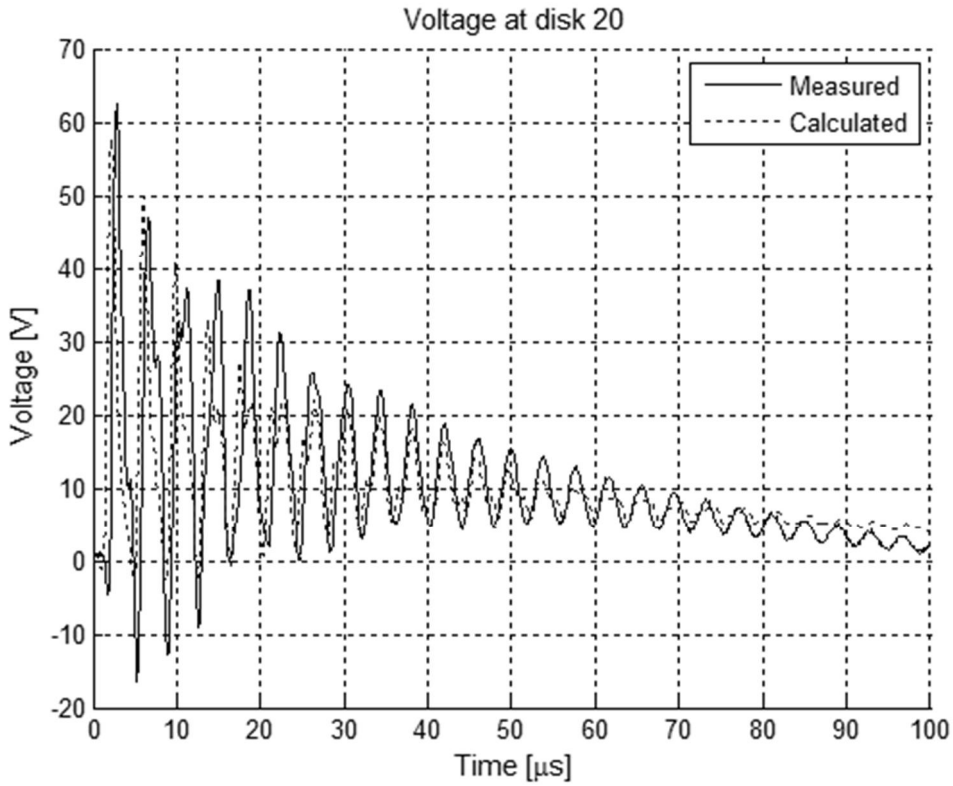

Figure 5-36: Voltages at disk 20 (state-space formulation with generated LI)

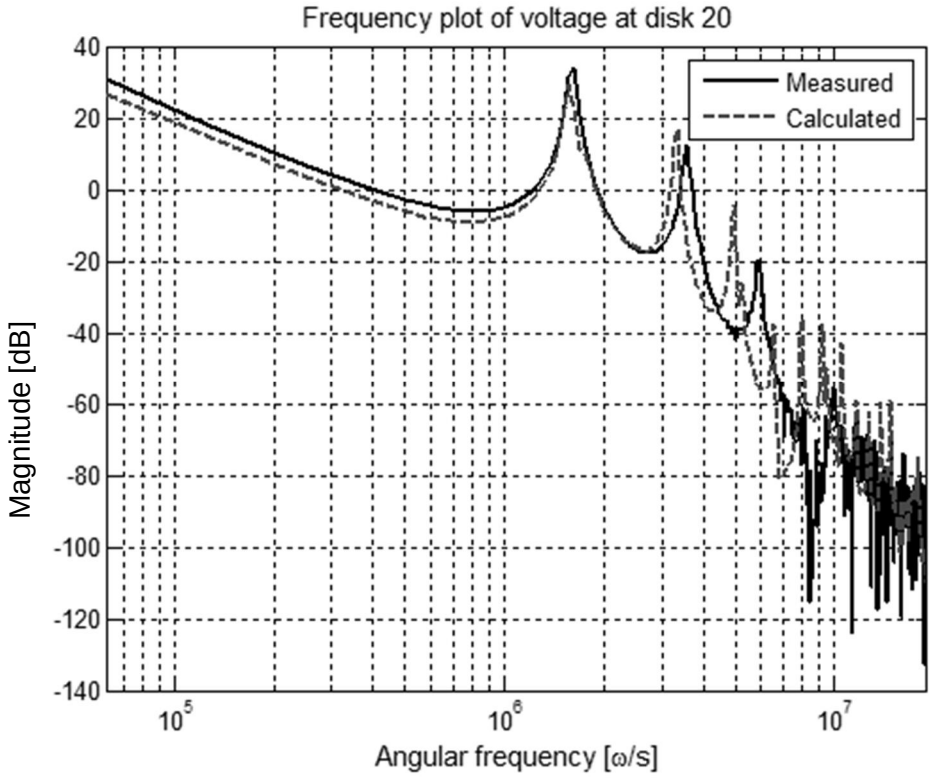

Figure 5-37: Frequency content of voltages at disk 20 (state-space formulation with generated LI)

Chapter 6 Conclusions and recommendations

6.1 Introduction

This chapter discusses the conclusions that can be drawn from the results presented in the preceding chapters. These conclusions are derived with reference to the project and research objectives stated in 1.3.1. Each objective is reviewed along with the relevant outcome on completion of this project. Recommendations are made based upon the conclusions presented in the following sections. This includes a discussion of possible improvements that can be made, as well as some matters that may require further research to improve model accuracy.

6.2 Conclusions

6.2.1 Overview

From the point of view of the power transformer manufacturer, the insulation structure of the power transformer is designed to withstand the maximum overvoltage expected during standard factory acceptance tests. In light of this, the only matter that the design engineer is interested in is the voltage profile along the winding for the duration of the applied excitation wave. Of particular interest to the design engineer is the maximum voltage value and the trend in terms of the wave attenuation.

Chapter 5 presents a case study where the modelling methods presented in this thesis were applied to a test-unit. The test-unit is a single disk-type winding which is commonly found in large power transformers. No magnetic core is present due to the facts presented in section 2.4.2.2. The test-unit was modelled by using both a lossless model in differential equation form and a model in state-space form that includes the iron and copper losses. A comparison between the models was done for two measured input signals namely LI and LIC. The results of the two models were compared to the measured voltages of the actual test-unit for the same input excitation wave. A third comparison was done using a signal that was mathematically created to represent a LI wave.

A comparison in the frequency-domain of the output of both models indicated a good correlation with the measured signals for the first two resonance points which extend up to 300 kHz. The magnitudes of the resonance frequencies calculated using the lossless model are not as accurate as that of the model containing losses but the locations of the frequencies matche well. From the comparisons done for LIC excitation, it would seem that

the lossless model does not perform well for frequencies above 300 kHz. However, the model that accounts for the losses accurately represents the resonance frequencies up to 650 kHz with respect to both amplitude and location.

The result that is of particular interest to the power transformer design engineer is the accuracy of the representation of the time-domain response. When comparing the measured and calculated results presented in this thesis, it is evident that the lossless model does not fulfil this need. The model that includes the losses in the transformer succeeds in this.

The results from the case study given in Chapter 5 indicate that the project objective has successfully been achieved. The research objectives that led to the successful outcome of the project are those presented in section 1.3.2. These objectives and their respective outcomes are discussed in the following section.

6.2.2 Development of a modelling methodology

The literature survey presented in Chapter 2 revealed a wide variety of modelling methods which can be used to achieve the objective of this project. The choice of an appropriate modelling method was not a trivial one, since various approaches seemed suitable for the application.

The chosen method was to represent the winding with an equivalent electrical circuit to form a lumped parameter model as discussed in 2.5.2.1. This method provided an intuitive way to represent the capacitive, inductive and dissipative behaviour of the transformer winding. The application of this methodology was also easy to implement in a digital environment.

The frequency-domain response shows a decrease in accuracy as the frequency content of the excitation wave increases. This could be caused by the inherent error of a discretised model as mentioned in 2.5.2.2. However, the deviation between measured and calculated results does not seem to be significant at the frequencies of interest. It can therefore be assumed that the order of the model is appropriate for this application.

6.2.3 Calculation methods for the model parameters

The calculation of winding inductances and capacitances could be approached in multiple ways. The use of FEM simulations as the primary method is not practical due to the time required for generating the geometry and setting up of boundary and material properties. The calculation time is also excessive especially for large geometries. FEM simulations does however provide very accurate results and these were used as a benchmark in the

evaluation of alternative calculation methods. To maintain short computation time, closed-form equations were used for the calculation of the model parameters. The validation of the inductance and capacitance calculation by means of closed-form equations was done by comparing the results with actual measured values.

The inductance of the winding was calculated assuming an air-core in light of the matters discussed in section 3.3.1. The calculated self- and mutual-inductances were compared to results obtained from FEM. The deviation between the results obtained using closed-form equations versus those found using FEM was very small. The calculated self-inductance of the winding was compared to the measured inductance of the actual test-unit. The deviation was negligible.

The capacitances in and around the winding was also calculated using closed-form equations. The calculated values were also compared with FEM results and the values measured during laboratory testing. Values calculated using closed-form equations varied in accuracy when compared to those found using FEM. The deviations observed were much higher than that found in the inductance calculations. The measured ground capacitance of the winding was also a bit higher than the values calculated. The severity of these deviations does not seem to be of concern when analysing the time-domain response of the model.

6.2.4 Modelling of non-linear frequency dependant damping

Copper and dielectric losses were considered in this project. The copper losses caused by the reduction of the effective conductor area due to the skin-effect was calculated and included in series with the inductive element of each branch in the model. The dielectric losses due to the leakage currents in the dielectric material were also included in the model. Since the model application will be limited to the frequency range of 10 - 500 kHz, an average frequency of 225 kHz was used to calculate all losses in the system.

6.2.5 Identification, implementation and validation of solver algorithms

In Chapter 4 two mathematical formulations of the equivalent electrical circuit model were explored. The initial approach was to implement a nodal formulated model. The advantage of this formulation is that its structure simplifies model expansion and the addition of non-linear time dependant elements and sub-networks. The model was solved by means of the difference equation method. The challenge faced when using this formulation is that the addition of loss components in the inductive branches increases the complexity of the history terms. In light of this, the model did not include system losses.

An alternative approach was to use a State-space formulation. The structure of this formulation can easily include losses in the inductive branches. The copper and dielectric dissipation was included in the model and an ODE solver was used to solve the system of differential equations.

The solver algorithms were implemented in a MATLAB® environment. Appendix C presents the code of the difference equation solver used to solve the nodal formulated model. The state-space formulated model was solved using a built-in solver of MATLAB® namely *lsim*. In terms of execution time, lsim performed much better than the difference equation solver. A model representing the test-unit was solved using both solvers. The lsim solver took approximately 30 s to execute while the execution of the difference equation solver required a runtime of two orders higher than that of the lsim solver.

The investigation identified the state-space formulation in conjunction with the built-in lsim function of MATLAB® as the preferable solution methodology. This is due to the ease with which dissipative elements are included in the inductance branches and the fast runtime.

6.3 Recommendations

Though the project objective has been successfully accomplished, various matters have been identified that requires further research. Various opportunities exist that can be used to improve the accuracy of calculations. The application of the work done in this project can also be broadened with some augmentations. The following sections presents the major aspects that can to be addressed in future work.

6.3.1 Modelling effect of iron-core

In this study the effects of the iron-core were not taken into account. The reasoning behind this methodology is presented in 2.4.2.2. However, since the test-unit did not contain an iron-core, the validity of this assumption still remains unaddressed and requires additional research. The non-linear frequency dependency of the core's magnetic properties and the isotropic nature of the material's permeability are all constituents of the complex behaviour of the core.

To determine the severity of the effects when considering the context defined in section 1.2, the test-unit must be fitted with a laminated iron-core. A comparison should then be made between the calculated and measured inductance and voltage values. An investigation of this nature will confirm or dismiss the assumption made in the inductance calculation methods which currently omits the effect of the presence of the iron-core. It would also be

valuable to consider the effect of the iron-core on other model parameters such as the losses in the system. Alternative inductance calculation methodologies such as those briefly discussed in section 2.4.2.3 could also be implemented to improve the model accuracy when an iron-core is present.

6.3.2 Improved modelling of non-linear frequency dependant losses

Only copper- and dielectric losses were considered in the modelling methods presented in this thesis. Reasonable results were obtained in this way. It can, however, be reasoned from the concluding remarks in section 6.2.3 that losses do contribute to the model accuracy especially when analysing the model response to high frequency excitation – a fact also supported by various authors as presented in 2.4.4. It may be possible to achieve a higher level of accuracy in the high frequency range by merely improving the calculation of the damping in the system.

Another matter to consider is the fact that the losses in the system were calculated for a fixed frequency of 225 kHz. In actual fact, the frequency content of the voltage wave varies over time and position, and thus is not a constant for the duration of the transient. Thus, for greater accuracy, the losses should be updated for each element after each time step.

Since no core was present in the test-unit, omitting core losses is only logical. However, if an iron-core is present in the test-unit, losses due to eddy currents on the core surface should also be considered during the model development.

6.3.3 Extending model to multi-winding configurations

The project objective in this study was limited to the modelling of a single power transformer disk-type winding. This was the very first step in the development of a complete electromagnetic modelling methodology for power transformer with complex winding configurations and winding types.

After the above mentioned recommendations have been addressed, another case study should be done on a complete power transformer assembly that includes primary and secondary windings as well as a laminated iron-core. The effect of the magnetic coupling to other phases in a three phase transformer can also be investigated and implemented.

REFERENCES

[1] A. Hadfield, "Energy for people," *Power Engineering Journal*, vol. 7, no. 1, pp. 7 - 16, February 1993.

[2] J. C. Ekeh, "Issues and challenges of power sector reforms in a depressed economy," *5th International Conference on European Electricity Market*, pp. 1 - 7, 2008.

[3] L. Musaba and P. Naidoo, "Power supply challenges in Southern Africa," in *IEEE Power & Energy Society General Meeting*, 2009, pp. 1 - 6.

[4] J. Zhong, C. Wang, and Y. Wang, "Chinese growing pains," *IEEE Power and Energy Magazine*, vol. 5, no. 4, pp. 33 - 40, 2007.

[5] J. P. Bickford and A. G. Heaton, "Transient overvoltages on power systems," *IEE Proceedings Conference on Generation, Transmission and Distribution*, vol. 133, no. 4, pp. 201 - 225, May 1986.

[6] IEC 60060-1, "High-Voltage test techniques - Part 1: General definitions and test requirements," International Electrotechnical Commission, International Standard IEC 60060-1, 1989.

[7] IEC 60076-3, "Power Transformers - Part 3: Insulation levels, dielectric tests and external clearances in air," International Electrotechnical Commission, International Standard IEC 60060-1, 2000.

[8] J. A. Martinez-Velasco, Ed., *Power system transients : Parameter determination*. New York, United States of America: CRC Press, 2010.

[9] R. Malewski, J. Douville, and L. Lavallee, "Measurement of switching transients in 735 kV substations and assessment of their severity for transformer insulation," *IEEE Transactions on Power Delivery*, vol. 3, no. 4, pp. 1380 - 1390, Octover 1988.

[10] M. Hori et al., "Internal winding failure due to resonance overvoltage in distribution transformer caused by winter lightning," *IEEE Transactions on Power Delivery*, vol. 21, no. 3, pp. 1600-1606, July 2006.

[11] P. A. Abetti, "Survey and classification of publisled data on the surge performance of transformers and rotating machines," *Transactions of the American Institute of*

Electrical Engineers on Power Apparatus and Systems, vol. 77, no. 3, pp. 1403 - 1413, April 1958.

[12] L. V. Bewley, "Transient oscillations in distributed circuits with special reference to transformer windings," *Transactions of the American Institute of Electrical Engineers*, vol. 50, no. 4, pp. 1215 - 1233, 1931.

[13] B. M Dent, E. R. Hartill, and J. G. Miles, "A method of analysis of transformer impulse voltage distribution using a digital computer," *Proceedings of the IEE Power Engineering*, vol. 105, no. 23, pp. 445 - 459, October 1958.

[14] P. I. Fergestad and T. Henriksen, "Transient oscillations in multiwinding transformers," *IEEE Transactions on Power Apparatus and Systems*, vol. 93, no. 2, pp. 500 -509, March 1974.

[15] A. Greenwood, *Electrical transients in power systems*, 2nd ed. USA: Wiley interscience, 1991.

[16] J. M. Weed, "Abnormal voltages in transformers," *Transactions of the American Institute of Electrical Engineers*, vol. 34, no. 2, pp. 2197 - 2236, 1915.

[17] L. F. Blume and A. Boyajian, "Abnormal voltages within transformers," *Transactions of the American Institute of Electrical Engineers*, vol. 38, no. 1, pp. 577 - 620, January 1919.

[18] B. Heller and A. Veverka, *Surge phenomena in electrical machines*, J. S. Vosper, Ed. London: Iliffe Books LTD., 1968.

[19] R.C. Degeneff, "A general method for determining resonances in transformer windings," *IEEE Transactions on Power Apparatus and Systems*, vol. 96, no. 2, pp. 423 - 430, March 1977.

[20] P. A. Abetti and F. J. Maginniss, "Natural frequencies of coils and windings determined by equivalent circuit," *Transactions of the American Institute of Electrical Engineers on Power Apparatus and Systems*, vol. 72, no. 2, pp. 495 - 504, January 1953.

[21] H. Sun, G. Liang, X. Zhang, and X. Cui, "Analysis of resonance in transformer windings under very fast transient overvoltages," in *17th International Zurich*

Symposium on Electromagnetic Compatibility, Zurich, 2006, pp. 432 - 435.

[22] U. R. Massaro, "Electrical transient interaction between transformers and power system - Brazilian experience," in *presented at the International Conference Power System Transients*, Delft, 2011.

[23] R. M. Del Vecchio, B. Poulin, P. T. Feghali, D. M. Shah, and R. Ahuja, *Transformer design principles: With applications to core-form power transformers*, 2nd ed.: CRC Press, 2010.

[24] K. Karsai, D. Kerenyi, and L. Kiss, *Large power transformers*.: Elsevier, 1987.

[25] S. V. Kulkarni and S. A. Khaparde, *Transformer engineering - Design and practice*. United States of America: Marcel Dekker, Inc., 2004.

[26] X. M. Lopez-Fernandez, C. Alvarez-Marino, D. Couto, R. Lopes, and A. Jacomo-Ramos, "Modeling and insulation design methodology in power transformer under fast transients," in *XIX International Conference on Electrical Machines*, 2010, pp. 1-6.

[27] A. Pederson, "On the response of interleaved transformer windings to surge voltages," *IEEE Transactions on Power Apparatus and Systems*, vol. 82, no. 66, pp. 349 - 356, June 1963.

[28] R. M. Del Vecchio, B. Poulin, and R. Ahuja, "Calculation and measurement of winding disc capacitances with wound-in-shields," *IEEE Transactions on Power Delivery*, vol. 13, no. 2, pp. 503 - 509, April 1998.

[29] H. B. Margolis, J. Phelps, A. A. Carlomagno, and A. J. McElroy, "Experience with part-winding resonance in EHV auto-transformers: Diagnosis and corrective measures," *IEEE Transactions on Power Apparatus and Systems*, vol. 94, no. 4, pp. 1294 - 1300, August 1975.

[30] H. M. Pflanz and G. N. Lester, "Control of overvoltages on energizing capacitor banks," *IEEE Transactions onPower Apparatus and Systems*, vol. 92, no. 3, pp. 907-915, 1973.

[31] A. C. O. Rocha, "Impact of transformer modeling in assessing dielectric failure analysis," in *presented at the International Conference Power System Transients*,

Delft, 2011.

[32] ABB, *Transformer Handbook*, 3rd ed., 2007.

[33] H. W. Kerr and S. Palmer, "Developments in the design of large power transformers," *Proceedings of the Institution of Electrical Engineers*, vol. 111, no. 4, pp. 823 - 832, April 1964.

[34] A. C. Franklin and J. S. C. Franklin, *J&P Transformer handbook*, 11th ed.: Butterworth Heinemann, 1995.

[35] H. P. Moser, *Transformerboard*. Rapperswil: Weidmann AG, 1979.

[36] H. P. Moser, *Transformerboard 2*, 2nd ed., 1991.

[37] E. Kuffel, W. W. Zaengl, and J. Kuffel, *High Voltage Engineering: Fundamentals*, 2nd ed.: Elsevier, 2000.

[38] L. V. Bewley, *Traveling waves on transmission systems*, 2nd ed. New York: Dover Publications Inc., 1963.

[39] G. M. Stein, "A Study of the initial surge distribution in concentric transformer windings," *IEEE Transactions on Power Apparatus and Systems*, vol. 83, no. 9, pp. 877 - 893, September 1964.

[40] 60071-4, IEC TR, "Insulation co-ordination: Computational guide to Insulation co-ordination and modeling of electrical networks," International Electrotechnical Commission, Technical Report 2004.

[41] R. C. Degeneff et al., "Transformer response to system switching voltages," *IEEE Transactions on Power Apparatus and Systems*, vol. 101, no. 6, pp. 1457 - 1470, June 1982.

[42] R. Sobocki, "Function representation of lightning impulse wave," *IEE Proceedings on Physical Science, Measurement and Instrumentation, Management and Education*, vol. 134, no. 9, pp. 721 - 726, November 1987.

[43] R. Sobocki, "Function representation of lightning impulses produced by a testing circuit with continuity of voltages and currents at a tested object," *IEE Proceedings on*

Science, Measurement and Technology, vol. 138, no. 1, pp. 78 - 82, January 1991.

[44] R. C. Degeneff, "Transient-voltage response," in *Electric power transformer engineering*, J. H. Harlow, Ed.: CRC Press, ch. 20.

[45] R. C. Degeneff and W. N. Kennedy, "Calculation of initial, pseudo-final and final voltage distributions in coils using matrix techniques," in *Summer Power Meeting*, San Francisco, 1975.

[46] P. A. Abetti and H. F. Davis, "Surge Transfer in 3-Winding Transformers," *Transactions of the American Institute of Electrical Engineers on Power Apparatus and Systems*, vol. 73, no. 2, pp. 1395 -1407, December 1954.

[47] L. C. Shen and J. A. Kong, *Applied electromagnetism*, 3rd ed.: PWS Publishing Company, 1995.

[48] D. K. Gehmlich and S. B. Hammond, *Electromechanical systems*. USA: McGraw-Hill, 1967.

[49] Massachusetts Institute of Technology, *Magnetic circuits and transformers*. Massachusetts, USA: MIT Press, 1943.

[50] D. Vitkovitch, *Field analysis: Experimental and computational methods*. London, Britain: The Camelot Press, 1966.

[51] K. K. Palueff, "Effect of transient voltages on power transformer design," in *Transactions of the American Institute of Electrical Engineers*, New York, 1929, pp. 681-701.

[52] R. Rudenburg, "Performance of traveling waves in coils and windings," *Transactions of the American Institute of Electrical Engineers*, vol. 59, no. 12, pp. 1031-1040, 1940.

[53] Y. Shibuja, S. Fujita, and N. Hosokawa, "Analysis of very fast transient overvoltages in transformer winding," *IEE Proceedings on Generation, Transmission and Distribution*, vol. 144, no. 5, pp. 461 - 468, September 1997.

[54] T. R. Lyle, "On the self-inductance of circular coils of rectangular section," *Philosophical Transactions of the Royal Society of London*, vol. 213, pp. 421 - 435,

1914.

[55] E. B. Rosa, *The self and mutual inductances of linear conductors*, Bulletin of the Bureau of Standards, Ed.: U.S. Dept. of Commerce and Labor, Bureau of Standards, September 1907, vol. 4.

[56] W. Grover, *Inductance calculations*. New York, United States of Amarica: D. Van Nostrand Co., 1946.

[57] F. W. Grover, "Formulas and tables for the calculation and design of single-layer coils," *Proceedings of the Institute of Radio Engineers*, vol. 12, no. 2, pp. 193 - 208, 1924.

[58] F. W. Grover, "The calculation of the inductance of single-layer coils and spirals wound with wire of large cross section," *Proceedings of the Institute of Radio Engineers*, vol. 17, no. 11, pp. 2053 - 2063, 1929.

[59] M. D. Loose, "Lumped parameter based transformer analysis: Modeling, reduction, time and frequency domain solutions," Rensselaer Polytechnic Institute, New York, Thesis 2003.

[60] A. Miki, T. Hosoya, and K. Okuyama, "A Calculation method for impulse voltage distribution and transferred voltage in transformer windings," *IEEE Transactions on Power Apparatus and Systems*, vol. 97, no. 3, pp. 930 - 939, June 1978.

[61] S. D. Mitchell and J. S. Welsh, "Permeability and its influence on the broadband frequency response of a power transformer," *Power and Energy Engineering Conference, APPEEC 2009. Asia-Pacific*, 2009.

[62] P. A. Abetti, "Transformer models for the determination of transient voltages," *Transactions of the American Institute of Electrical Engineers on Power Apparatus and Systems*, vol. 72, no. 2, pp. 468 - 480, January 1953.

[63] P. A. Abetti and F. J. Maginniss, "Fundamental oscillations of coils and windings," *Power Apparatus and Systems, Part III. Transactions of the American Institute of Electrical Engineers*, vol. 73, no. 1, pp. 1 - 10, 1954.

[64] L. Rabins, "Transformer reactance calculations with digital computers," *AIEE Transactions*, vol. 75, pp. 261 - 267, July 1956.

[65] J. A. Quintana, "Modeling frequency dependent losses in transformers," Rensselaer Polytechnic Institute, New York, Ph.D Thesis 1999.

[66] Y. Li, J. Du, X. Li, and D. Li, "Calculation of capacitance and inductance parameters based on FEM in high-voltage transformer winding," *International Conference on Electrical Machines and Systems*, pp. 1 - 4, 2011.

[67] M. Popov, L. van der Sluis, R. P. Smeets, and J. Lopez-Roldan, "Analysis of very fast transients in layer-type transformer windings," *IEEE Transactions on Power Delivery*, vol. 22, pp. 238-247, January 2007.

[68] M. Bagheri, A. Hekmati, R. Heidarzadeh, and M. Naderi, "Impulse voltage distribution in intershield disk winding VS interleaved and continuous disk winding in power transformer," in *IEEE 2nd International Power and Energy Conference*, 2008, pp. 387 - 392.

[69] H. Nishiyama and M. Nakamura, "Capacitance of disk capacitors," *IEEE Transactions on Components, Hybrids, and Manufacturing Technology*, vol. 16, no. 3, pp. 360 - 366, May 1993.

[70] M. N. Sadiku, S. M. Musa, and S. R. Nelatury, *Comparison of approximate formulas for the capacitance of microstrip line*., 2007.

[71] M. Florkowski, B. Florkowska, J. Furgal, and P. Pajak, "Impact of oil and temperature on initial voltage distributions in transformer windings at ultra fast stresses," in *Annual Report Conference on Electrical Insulation and Dielectric Phenomena*, 2010, pp. 1 - 4.

[72] F. M. Clark, *Engineering guide book for electrical insulation*. New York, United States of America: General Electric Company, 1958, vol. I.

[73] A. Semlyen and F. De Leon, "Eddy current add-on for frequency dependent representation of winding losses in transformer models used in computing electromagnetic transients," *IEE Proceedings on Generation, Transmission and Distribution*, vol. 141, no. 3, pp. 209 - 214, May 1994.

[74] P. I. Fergestad, "Transient oscillations in transformer windings," Universitetsforlaget, 1972.

[75] E. Mombello and K. Moller, "New power transformer model for the calculation of electromagnetic resonant transient phenomena including frequency-dependent losses," *IEEE Transactions on Power Delivery*, vol. 15, no. 1, pp. 167 - 174, January 2000.

[76] T. J. Lewis, "The transient behaviour of ladder networks of the type representing transformer and machine windings," *Proceedings of the IEE on Power Engineering*, vol. 101, no. 83, pp. 541-553, April 1954.

[77] H. Poritsky, P. A. Abetti, and R. P. Jerrard, "Field theory of wave propagation along coils," pp. 930 - 939, October 1953.

[78] S. Song, H. Kim, T. Chung, and S. Hahn, "Modal analysis for the transient internal voltage of a transformer," *IEEE Transactions on Magnetics*, vol. 40, no. 2, pp. 581 - 584, March 2004.

[79] M. Popov, L. van der Sluis, G. C. Paap, and H. de Herdt, "Computation of very fast transient overvoltages in transformer windings," *IEEE Transactions on Power Delivery*, vol. 18, no. 4, pp. 1268 - 1274, October 2003.

[80] S. M. Hosseini, M. Vakilian, and G. B. Gharehpetian, "Comparison of transformer detailed models for fast and very fast transient studies," *IEEE Transactions on Power Delivery*, vol. 23, no. 2, pp. 733 - 741, April 2008.

[81] S. M. H. Hosseini, M. Vakilian, and G. B. Gharehpetian, "An improved MTL modeling of transformer winding," *presented at the International Conference Power System Transients, Lyon*, 2007.

[82] G. Hoogendorp, M. Popov, and L. van der Sluis, "Computation of inter-turn voltages in transformer windings with interconnected distribution cable," in *presented at the International Conference Power System Transients*, Delft, 2011.

[83] A. R. Djordjevic, T. K. Sarkar, and R. F. Harrington, "Time-domain response of multiconductor transmission lines," *Proceedings of the IEEE*, vol. 75, pp. 743 - 764, June 1987.

[84] T. Dhaene and D. De Zutter, "Selection of lumped element models for coupled lossy transmission lines," *IEEE Transactions on Computer-Aided Design of Integrated*

Circuits and Systems , vol. 11, no. 7, pp. 805 - 815, July 1992.

[85] J. Du, G. Liang, H. Sun, Xin Liu, and Xixiao Liu, "Lumped parameter modeling of transformer windings under VFTO," *IEEE 4th International Symposium on Microwave, Antenna, Propagation, and EMC Technologies for Wireless Communications*, pp. 258 - 261, 2011.

[86] E. Rahimpour and M. Bigdeli, "Simplified transient model of transformer based on geometrical dimensions used in power network analysis and fault detection studies," in *Conference proceedings on POWERENG Power Engineering, Energy and Electrical Drives*, 2009, pp. 375 - 380.

[87] N. Watson and J. Arrillaga, *Power systems electromagnetic transients simulation*. London, United Kingdom: IET, 2007.

[88] G. Liang, H. Sun, X. Zhang, and X. Cui, "Modeling of transformer windings under very fast transient overvoltages," *IEEE Transactions on Electromagnetic Compatibility*, vol. 48, no. 4, pp. 621 - 627, November 2006.

[89] M. Popov, L. van der Sluis, R. P. Smeets, J. Lopez-Roland, and V. V. Terzija, "Modelling, simulation and measurement of fast transients in transformer windings with consideration of frequency-dependent losses," *IET Proceedings on Electric Power Applications*, vol. 1, no. 1, pp. 29 - 35, January 2007.

[90] Tektronix, "ABC's of probes," Tektronix, Primer 2009.

[91] R. Blake, *Electronic communication systems*, 2nd ed. USA: Delmar, 2002.

[92] S. K. Mitra, *Digital Signal Processing - A computer-based approach*. Singapore: McGraw-Hill, 2006.

[93] R. H. Walden, "Analog-to-Digital converter survey and analysis," *IEEE Journal on Selected Areas in Communications*, vol. 17, no. 4, pp. 539 - 556, April 1999.

[94] R. Skartlien and L. Oyehaug, "Quantization error and resolution in ensemble averaged data with noise," *IEEE Transactions on Instrumentation and Measurement*, vol. 54, no. 3, pp. 1303 - 1312, June 2005.

[95] C. Phillips, J. M. Parr, and E. A. Riskin, *Signals, systems and transforms*, 3rd ed.: Pearson Education, 2003.

[96] J. L. Guardado and K. J. Cornick, "A computer model for calculating steep-fronted surge distribution in machine windings," *IEEE Transactions on Energy Conversion*, vol. 4, no. 1, pp. 95 - 101, March 1989.

[97] C. Snow, *Formulas for computing capacitance and inductance*, 544th ed. Washington, United States of America: National Bureau of Standards , 1954.

[98] G. Kron, *Tensor analysis of networks*. London: MacDonald, 1965.

[99] F. de Leon and A. Semlyen, "Reduced order model for transformer transients," *IEEE Transactions on Power delivery*, vol. 7, no. 1, pp. 361 - 369, January 1992.

[100] W. J. McNutt, T. J. Blalock, and R. A Hinton, "Response of transformer windings to system transient voltages," pp. 457 - 467, 1973.

[101] M. Perkins, A. Fazlagic, and G. Frimpong, "Dielectric frequency response measurment as a tool for troubleshooting insulation power factor problems," *Conference record of the IEEE International Symposium on Electrical Insulation*, pp. 162 - 165, April 2002.

[102] H. W. Dommel, "Digital computer solution of electromagnetic transients in single and multi phase networks," *IEEE Transactions on Power Apparatus and Systems*, vol. 88, no. 4, pp. 388 - 399, April 1969.

[103] R. C. Degeneff, "Reducing storage and saving computational time with a generalization of the Dommel solution method," in *IEEE PICA*, 1977, pp. 307-313.

[104] B. J. Van Jaarsveld and H. J. Vermeulen, "Implementation and evaluation in MATLAB of Dommel's method for a lumped parameter model of a power transformer," in *presented at the South African Universities Power Engineering Conference*, Cape Town, 2011.

[105] Matlab. Matlab.

[106] S. Kurz and M. Loppacher, "RSG 482 Operating instructions," HAEFELY - High Voltage Test, Operating instructions 2008.

[107] M. Abid, K. ben Abdallah, and R. Mraihi, "Causality relationship between energy industrial consumption and economic growth: Application on Tunisian country," in *First International Conference on Renewable Energies and Vehicular Technology*, 2012, pp. 396 - 404.

[108] J. B. Allen and L. R. Rabiner, "A Unified approach to short-time Fourier analysis and synthesis," *Proceedings of the IEEE*, vol. 65, no. 11, pp. 1558 - 1564, November 1977.

[109] M. Bigdeli and E. Rahimpour, "Estimation of simplified transient model parameters using genetic algorithm," in *18th Iranian Conference on Electrical Engineering*, 2010, pp. 722 -726.

[110] F. F. Brand and K. K. Palueff, "Lightning studies of transformers by the cathode ray oscillograph," *Transactions of the American Institute of Electrical Engineers*, vol. 48, no. 3, pp. 998 - 1008, July 1929.

[111] C. C. Brozio and H. J. Vermeulen, "Wideband equivalent circuit modelling and parameter estimation methodology for two-winding transformers," *IEE Proceedings on Generation, Transmission and Distribution*, vol. 150, no. 4, pp. 487 - 492, 2003.

[112] S. Chimklai and J. R. Marti, "Simplified three-phase transformer model for electromagnetic transient studies," *IEEE Transactions on Power Delivery*, vol. 10, no. 3, pp. 1316 - 1325, July 1995.

[113] Guishu Liang and Haifeng Sun and Xile Zhang and Xiang Cui, "Modeling of transformer windings under very fast transient overvoltages," *IEEE Transactions on Electromagnetic Compatibility*, vol. 48, pp. 621 -627, November 2006.

[114] A.A. Dahab, P.E. Burke, and T.H. Fawzi, "A complete model of a single layer air-cored reactor for impulse voltage distribution," *IEEE Transactions on Power Delivery*, vol. 3, pp. 1745 -1753, October 1988.

[115] S. Darlington, "A history of network synthesis and filter theory for circuits composed of resistors, inductors, and capacitors," *IEEE Transactions on Circuits and Systems*, vol. 31, no. 1, pp. 3 - 13, 1984.

[116] P. I. Fergestad and T. Henriksen, "Inductances for the calculation of transient oscillations in transformers," *IEEE Transactions on Power Apparatus and Systems*,

vol. 93, no. 2, pp. 510 - 517, 1974.

[117] J. S. Forrest, "The performance of the British grid systems in thunderstorms," *Proceedings of the IEE: Power Engineering*, vol. 97, no. 57, pp. 345 - 356, 1950.

[118] S. Gracia, A. Medina, and C. Perez, "A state space single-phase transformer model incorporating nonlinear phenomena of magnetic saturation and hysteresis for transient and periodic steady-state analysis," in *IEEE Power Engineering Society Summer Meeting*, vol. 4, 2000, pp. 2417 - 2421.

[119] J. R. Griffith and M. S. Nakhla, "Time-domain analysis of lossy coupled transmission lines," *IEEE Transactions on microwave theory and techniques*, vol. 38, no. 10, pp. 1480 - 1487, October 1990.

[120] P. G. McLaren and H. Oraee, "Multiconductor transmission-line model for the line-end coil of large AC machines," *IEE Proceedings on Electric Power Applications*, vol. 132, no. 3, pp. 149 - 156, May 1985.

[121] G. W. Milne, "Ground voltage and current cancellation by co-axial cable," in *Proceedings of the 11th IEEE Symposium on Computers and Communications*, 2006, pp. 327 - 332.

[122] A. Opal, "The transition matrix forlinear circuits," *IEEE Transactions on Computer-Aided Design of Integrated Circuits and Systems*, vol. 16, no. 5, pp. 427 - 436, May 1997.

[123] C. Zhao, J. Ruan, Z. Du, and L. Chen, "Solution for voltage distribution in transformer winding model," in *Power and Energy Engineering Conference*, Asia-Pacific, 2009, pp. 1 - 5.

[124] X. Zhu, H. Dong, G. Lian, and C. Ji, "A new hybrid model of transformer windings under very fast transient overvoltages," in *International Conference on Electrical Machines and Systems* , 2008, pp. 4296 - 4301.

Appendix A Calculation of impulse function constants

With reference to Figure 2-9, the constants in equation (2.3) can be determined in the following manner. The derivative of equation (2.3) results in the following equation:

$$\frac{dv}{dt} = k_k\left(-\alpha_k e^{-\alpha_k t} + \beta_k e^{-\beta_k t}\right). \tag{A.1}$$

The gradient at the peak value at time t_p is zero, such that (A.1) can be written as:

$$0 = k_k(-\alpha_k e^{-\alpha_k t_p} + \beta_k e^{-\beta_k t_p}). \tag{A.2}$$

From equation (A.2) t_p can be calculated as:

$$t_p = \frac{ln(\beta_k/\alpha_k)}{(\beta_k - \alpha_k)}. \tag{A.3}$$

For a per-unit voltage wave the equation (2.3) can be written as:

$$1.0 = k_k(e^{-\alpha_k t_p} - e^{-\beta_k t_p}) \tag{A.4}$$

When the voltage drop to 50 % of its peak value (2.3) can be written as:

$$0.5 = k_k(e^{-\alpha_k t_{50}} - e^{-\beta_k t_{50}}) \tag{A.5}$$

Using the Newtwon-Rapshon numerical differential solver, the constants can be calculated by first defining the Jacobian matrix for the following functions:

$$f_1 = \frac{ln(\beta_k/\alpha_k)}{(\beta_k - \alpha_k)} - t_p \tag{A.6}$$

$$f_2 = 1.0 - k_k(e^{-\alpha_k t_p} - e^{-\beta_k t_p}) \tag{A.7}$$

$$f_3 = 0.5 - k_k(e^{-\alpha_k t_{50}} - e^{-\beta_k t_{50}}) \tag{A.8}$$

The entries of the Jacobian matrix are then expressed in the following relations:

$$\frac{\delta f_1}{\delta \alpha_k} = \frac{(\beta_k - \alpha_k)/\alpha_k - ln(\beta_k/\alpha_k)}{(\beta_k - \alpha_k)^2} \tag{A.9}$$

$$\frac{\delta f_1}{\delta \beta_k} = \frac{1}{\beta_k(\beta_k - \alpha_k)} - \frac{ln(\beta_k/\alpha_k)}{(\beta_k - \alpha_k)^2} \tag{A.10}$$

$$\frac{\delta f_1}{\delta k_k} = 0 \tag{A.11}$$

$$\frac{\delta f_2}{\delta \alpha_k} = k_k t_p e^{-\alpha_k t_p} \tag{A.12}$$

$$\frac{\delta f_2}{\delta \beta_k} = -k_k t_p e^{-\beta_k t_p} \tag{A.13}$$

$$\frac{\delta f_2}{\delta k_k} = e^{-\beta_k t_p} - e^{-\alpha_k t_p} \tag{A.14}$$

$$\frac{\delta f_3}{\delta \alpha_k} = k_k t_{50} e^{-\alpha_k t_{50}} \tag{A.15}$$

$$\frac{\delta f_3}{\delta \beta_k} = -k_k t_{50} e^{-\beta_k t_{50}} \tag{A.16}$$

$$\frac{\delta f_3}{\delta k_k} = e^{-\beta_k t_{50}} - e^{-\alpha_k t_{50}} \tag{A.17}$$

The system of differential equations can then be written as:

$$\begin{bmatrix} \delta\alpha_k \\ \delta\beta_k \\ \delta k_k \end{bmatrix} = \begin{bmatrix} \frac{\delta f_1}{\delta \alpha_k} & \frac{\delta f_2}{\delta \alpha_k} & \frac{\delta f_3}{\delta \alpha_k} \\ \frac{\delta f_1}{\delta \beta_k} & \frac{\delta f_2}{\delta \beta_k} & \frac{\delta f_3}{\delta \beta_k} \\ \frac{\delta f_1}{\delta k_k} & \frac{\delta f_2}{\delta k_k} & \frac{\delta f_3}{\delta k_k} \end{bmatrix} \begin{bmatrix} -f_1 \\ -f_2 \\ -f_3 \end{bmatrix} \tag{A.18}$$

From Figure 2-9 it is seen by inspection that the front time can be expressed as:

$$t_f = \frac{5}{3}(t_{90} - t_{30}) . \tag{A.19}$$

There also exists a relationship between t_p and t_f such that:

$$t_p/t_f = 0.6\, log(t_{50}/t_f) . \tag{A.20}$$

Appendix B Resistivity of materials

Material	ρ_r(Ω-m)	σ(mho/m)
Aluminum	2.83×10^{-8}	3.53×10^{7}
Copper	1.69×10^{-8}	5.92×10^{7}
Gold	2.44×10^{-8}	4.10×10^{7}
Nickel	7.24×10^{-8}	1.38×10^{7}
Silver	1.62×10^{-8}	6.17×10^{7}
Germanium	0.45	2.20
Silicon	640:00	1.56×10^{-3}
Seawater (average)	0.25	4.00
Amber	5.00×10^{14}	2.00×10^{-15}
Glass	10^{10}–10^{14}	10^{-10}–10^{-14}
Petroleum oil	10^{14}	10^{-14}
Quartz	7.50×10^{17}	1.30×10^{-18}

* Data from American Institute of Physics Handbook (New York: McGraw-Hill, 1957).

Appendix C Dommel's solution method in Matlab

```
function [vn,t] = solveDommel(G,Qn,Cn,E,t)
%SOLVELDOMMEL Time-domain solver for system

%     Vn = solveDommel(G,Qn,Cn,E,t)solves the voltages for a nodal
      formulation model representation of a RLC network. The solver
      algorithm does not take into account dielectric and copper losses.

%   INPUTS
%   G:    Admittance matrix.
%   Qn:   Inverse nodal inductance matrix.
%   Cn:   Nodal capacitance matrix.
%   E:    Voltage excitation row vector.
%   t:    Time row vector.

%% Prelim data
% First add ground nodes to nodal matrices
cGnds = sum(Cn);
qGnds = zeros(size(cGnds));
gGnds = sum(G);

Cn(end+1,end+1) = sum(cGnds);
Qn(end+1,end+1) = sum(qGnds);
G (end+1,end+1) = sum(gGnds);
Cn(1:end-1,end) = -cGnds';
Cn(end,1:end-1) = -cGnds;
Qn(1:end-1,end) = -qGnds';
Qn(end,1:end-1) = -qGnds;
G(1:end-1,end) = -gGnds';
G(end,1:end-1) = -gGnds;

dt = max(t)/length(t);
points = length(E);
nodes = length(Cn);

% Find inductive and capacitive elements
[Ci,Cj,CVal]= find(Cn);
[Qi,Qj,QVal]= find(Qn);
[Gi,Gj,GVal]= find(G);
GL  = (dt/2)*QVal;     % G's of L
GC  = (2/dt)*CVal;     % G's of C

cInd = sub2ind(size(Cn),Ci,Cj);
qInd = sub2ind(size(Qn),Qi,Qj);
gInd = sub2ind(size(G),Gi,Gj);

% Build G
Gtmp = zeros(size(Cn));
Gtmp(cInd)  = Gtmp(cInd) + GC;
Gtmp(qInd)  = Gtmp(qInd) + GL;
Gtmp(gInd)  = Gtmp(gInd) + GVal;

% Split G into sub groups respective of known and unknown voltages;
Gaa = Gtmp(1:end-2,1:end-2);
Gbb = Gtmp(end-1:end,end-1:end);
Gab = Gtmp(1:end-2,end-1:end);
```

```
% Current and voltage vectors at t = 0;
vb      = E(1);                     % All known voltages
va      = zeros(length(Gaa),1);     % All unknown nodal voltages
IHistCv  = zeros(numel(cInd),1);    % History currents through C's - Vector
IHistLv  = zeros(numel(qInd),1);    % History currents through L's - Vector
IHistCm  = zeros(size(CnMod));      % History currents through C's - Matrix
IHistLm  = zeros(size(QnMod));      % History currents through L's - Matrix
IHa     = zeros(length(Gaa),1);     % History currents in nodes where
voltages are known
ia      = zeros(length(Gaa),1);     % Injected currents at nodes where
voltages are unknown

%% Solving nodal voltages
[GaaL,GaaU]=lu(Gaa);
for k = 1:points
    % Solving [Gaa][Va(t)] = [ia(t)]-[Iha(t-dt)]-[Gab][Vb(t)];
    vb = [E(k);0];            % Known nodal voltages.
    Itota = ia - IHa - Gab*vb;
    va = GaaU\(GaaL\Itota);
    vTemp = [va;vb];
    vn(:,k)=vTemp;
    % History current through each element:
    IHistCv = -2*(vTemp(Ci)-vTemp(Cj)).*GC - IHistCv; % History current
source values for C's from i to j
    IHistLv =  2*(vTemp(Qi)-vTemp(Qj)).*GL + IHistLv; % History current
source values for L's from m to n
    % Rebuild history current matrixes
    IHistCm(cInd)=IHistCv;
    IHistLm(qInd)=IHistLv;
    IH = (sum(IHistCm) + sum(IHistLm))';
    IHa = IH(1:end-2,1);
end
end
```